UC Berkeley
UC Berkeley Electronic Theses and Dissertations

Title

Ultrafast Dynamics in Condensed Matter Studied with Attosecond Extreme Ultraviolet Transient Reflectivity

Permalink

https://escholarship.org/uc/item/3xh309qx

Author

Kaplan, Christopher James

Publication Date

2019

Peer reviewed|Thesis/dissertation

Ultrafast Dynamics in Condensed Matter Studied with Attosecond Extreme Ultraviolet
Transient Reflectivity

By

Christopher J Kaplan

A dissertation submitted in partial satisfaction of the

requirements for the degree of

Doctor of Philosophy

in Chemistry

in the

Graduate Division

of the

University of California, Berkeley

Committee in charge:

Professor Stephen R. Leone, co-Chair

Professor Daniel M. Neumark, Co-Chair

Professor William H. Miller

Professor David Attwood

Spring 2019

Ultrafast Dynamics in Condensed Matter Studied with Attosecond Extreme Ultraviolet
Transient Reflectivity

Abstract

Ultrafast Dynamics in Condensed Matter Studied with Attosecond Extreme Ultraviolet

Transient Reflectivity

by

Christopher J Kaplan

Doctor of Philosophy in Chemistry

University of California, Berkeley

Professor Stephen R. Leone, Co-Chair

Professor Daniel M. Neumark, Co-Chair

The advent of attosecond pulse duration light sources has enabled the study of fundamental light-matter interactions. Condensed matter systems are of particular interest, as they are often significantly impacted by many body interactions, and thus provide a natural environment for the observation and study of such interactions in the time domain. In this dissertation, an apparatus for extreme ultraviolet (XUV) transient reflectivity is described, and several studies on ultrafast dynamics in solids are performed. In the first chapter, background on ultrafast spectroscopy, light matter interaction, and reflection from surfaces is provided, giving the necessary underpinnings for the subsequent discussion. In the second chapter, the development and capabilities of the constructed XUV transient reflection apparatus are reviewed. Additionally, the static refractive index of germanium (a commonly employed semiconductor), is recovered from multi angle reflection measurements. In the third chapter, femtosecond dynamics in germanium are studied by XUV transient reflection. The results are analyzed and interpreted in the context of the existing optical literature. In the fourth chapter, preliminary attosecond resolved measurements in germanium are presented, and the results are tentatively interpreted in the context of light dressed states. In the fifth chapter, attosecond dynamics of core excitons in magnesium oxide (MgO) are studied. The results are analyzed and interpreted as a light induced modification of excitonic coherence. This body of work is intended to establish XUV transient reflectivity as a technique for study of solid-state systems and to provide example studies in two representative systems, a semiconductor and an insulator.

"For me, it is far better to grasp the Universe as it really is than to persist in delusion, however satisfying and reassuring." – **Carl Sagan**

Table of Contents

List of Figures

List of Tables

List of Acronyms

NIR	Near infrared
XUV	Extreme ultraviolet
HHG	High harmonic generation
FWHM	Full width at half maximum
MgO	Magnesium oxide
CEP	Carrier envelope phase
CCD	Charge coupled device
ADP	Ammonium dihydrogen phosphate
BBO	Beta barium borate
ALS	Advanced light source
HH	Heavy hole
VB	Valence band
CB	Conduction band
LO	Longitudinal optical
Ti:Sapp	Titanium Sapphire

Acknowledgements

I would like to acknowledge my PhD advisors Steve Leone and Dan Neumark. Without your tireless support and encouragement I would not have been able to study at Berkley, let alone accomplish even a fraction of what I've done over the last 5 years. During my PhD, I made a difficult transition from an inorganic chemist to a hardcore electronic spectroscopist. Words fail to express my gratitude for the unfathomable patience and kindness Steve and Dan provided me while I made that transition.

During my time at Berkeley, I have been fortunate enough to work with many amazing colleagues. I'm very grateful to Marieke Jager and Christian Ott, my first mentors in the group. In particular Marieke was incredibly encouraging and helped me greatly in acclimating to a new field. My early experience of the group was defined by graduate students Lauren Borja, Andrew Attar, Natalie Gibson, Lucas Carneiro, Marieke Jager, Erika Warrick, and Marina Yang. I'm very grateful for the fun and supportive atmosphere they provided. I'm indebted to the postdocs whom I've worked with. Peter Kraus with whom I worked closely and who was there from the very beginning of the reflectivity experiment. Scott Cushing, who somehow exists as a quantum superposition: simultaneously intimidatingly knowledgably about solid state physics and yet also undeniably approachable and encouraging. Michael Zuerch, who's exacting standards and unflinching honesty were an essential help to me. I'm also grateful to Romain Geneaux, Maurizio Reduzzi, Brett Marsh, Aditi Bhattacherjee, Alexander Guggenmos, Wei Cao, Denisia Popolan, Kristen Schnorr, Mazyar Sabbar, Mihai Vaida, Krupa Ramasesha, and Andrey Gandman for help, encouragement and support.

I'm incredibly impressed with the students and postdocs who have come after me: Yuki Kobayashi, Hung-Tzu Chang, Andrew Ross, Ashley Fielder, Chris Tian Xue, Bethany Lamoreaux, Ilana Porter, Kristina Chang, Leah Harrison, and Yen-Chen Lin. I'm happy to know that the group is in good hands, and I'm excited to hear about the groundbreaking science that you all are currently working on.

I'd like to acknowledge my mentors in undergrad research. John Sheats: for conversing with me on the bus and thereby introducing me to the fascinating world of organometallic

x

Chapter 1: Introduction

1.1 Ultrafast spectroscopy

Understanding how matter behaves on an ultrashort timescale is of critical importance to chemistry and physics [1]. In condensed matter, as well as gas phase systems, equilibrium properties such as electrical and thermal conductivity, optical properties, and magnetic behavior are in large part determined by a delicate balance between a staggering number of competing ultrafast processes [2].

From a more fundamental perspective, the ability to study processes on an ultrafast timescale allows interrogation of chemistry on its natural timescale. The most fundamental processes of chemistry, electronic and nuclear motion, occur on the ultrafast timescale. The period of an electron in the first Bohr orbit around a hydrogen atom has a period of 152 as, [3] (1 as = 10^{-18} s), while the vibrational period of an H_2 molecule is 8 fs (1 fs = 10^{-15} s) [4]. Consequently, a proper understanding of the basic processes in chemistry and condensed matter physics requires investigation of processes on their native, ultrafast timescales.

The ability to probe femtosecond processes was heralded by the 1999 Nobel Prize to Ahmed Zewail, for "studies of the transition states of chemical reactions using femtosecond spectroscopy" [5]. Zewail's work – much of which used optical and infrared pulses to probe ultrafast dynamics – granted access to femtosecond processes, including vibrational dynamics and snapshots of reactions in real time [6,7].

Subsequently, the ability to probe attosecond dynamics was ushered in by the creation of attosecond duration extreme ultraviolet (XUV) pulses by high harmonic generation (HHG) [8,9]. The proliferation of HHG into the fields of the physical sciences has ushered in an attosecond revolution that has allowed researchers for the first time to probe electronic interactions on their natural timescale, which shows great promise for future investigations [10].

1.1.1 Pump-probe spectroscopy

One of the most powerful methods of investigating ultrafast dynamics in the time domain is the pump-probe technique. In a pump-probe experiment, two ultrashort events, typically laser pulses from a mode locked laser, are used to first excite, and then interrogate dynamics of an ultrashort process of interest.

An example experiment is shown below Figure 1. In Figure 1, a stronger pump (red) is used to induce some non-equilibrium dynamics in a sample. Changes in reflectivity of a time delayed probe pulse (blue) are then measured as a function of time delay (Δt). Because the reflectivity of the probe is ultimately linked to the optical response of the material, (see section 1.2.3 for details), the interaction of the probe with the sample reports on the ultrafast response of the sample.

In pump-probe experiments, the time delay Δt is typically created using an optical interferometer to produce an optical path difference between pump and probe, taking advantage of the known speed of light. Consequently, instability of the interferometer can lead to loss of
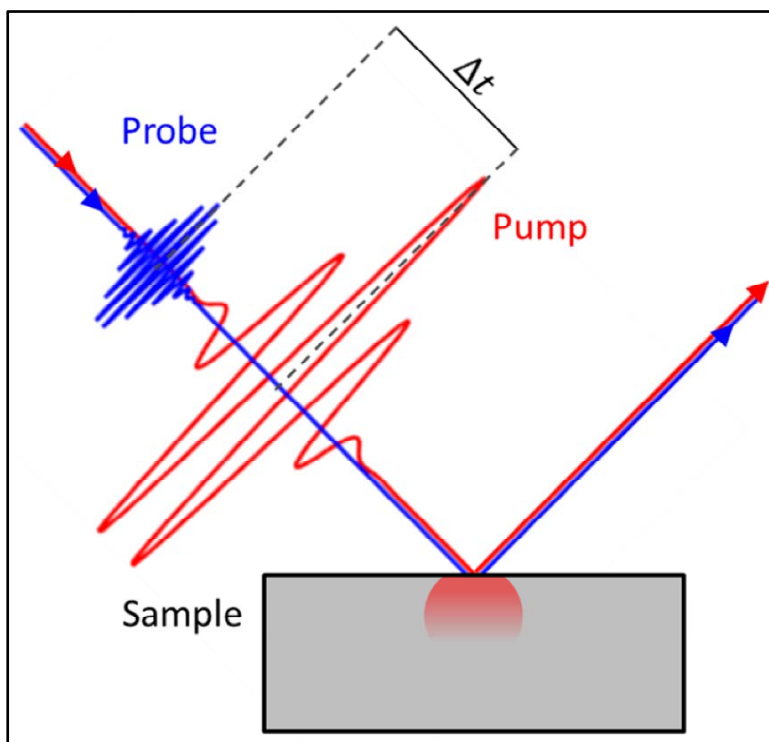
Figure 1: Example pump-probe experiment. A pump (red), incudes dynamics in a sample, which are subsequently probed by measuring the reflection of a time delayed probe (blue).

temporal resolution. Generally speaking, the time resolution of a pump-probe experiment is determined by a number of factors including experimental geometry, detection method, and importantly, the temporal duration of the pump and probe pulses.

The specific example in Figure 1 relies on detection of the reflectivity of the pump, termed transient reflectivity. However detection can be based on a number of methods including transmission (transient absorption) [11], photoelectrons (transient photoemission) [12], or even nonlinear mixing between pump and probe (transient wave mixing) [13]. Each specific variant of pump-probe spectroscopy comes with strengths and weaknesses, for example, transient absorption requires measuring transmitted light though a sample, which can be challenging or impossible for optically thick samples. Nevertheless, pump-probe methods are ubiquitous and have shown incredible promise for interrogating ultrafast processes [14].

1.1.2 Ultrafast process in solids

In solids, ultrafast excitation and subsequent relaxation of the excited material occur on a number of different timescales. The initial excitation occurs on a sub-femtosecond timescale [15] and is characterized by extremely rapid changes of electronic populations mediated by a wide variety of mechanisms [16–19] depending on the intensity of the exciting pulse and the electronic structure of the system. Directly following excitation, electronic screening of the excited carrier distribution occurs on a few femtosecond timescale [20]. On this timescale, ultrafast photodoping can result in renormalization of the electronic structure of the sample [21]. Subsequently, on the 10-100 fs timescale, excited carriers exchange energy and momentum via carrier-carrier scattering, beginning the formation of a thermal distribution [22]. Thermalization is then accelerated on the >50 fs timescale by carrier-phonon scattering, as carriers exchange energy and momentum with the lattice via a number processes involving carrier-phonon coupling, resulting in intervalley scattering [23,24] and a nonequilibrium population of phonons. Subsequently, on the ps timescale, the phonons generated by intervalley scattering may decay, and the excited carriers begin to experience diffusion [25,26]. Finally, carriers can recombine radiatively (via fluorescence on the ns timescale [27]), or non-radiatively (via Auger recombination on the ps-ns timescale [28]). Of the processes described above, relaxation and thermalization can be reasonably accessed by femtosecond resolution

measurements and have been studied extensively. In contrast, dynamics that occur during initial excitation requires attosecond resolution to be studied. Consequently, this regime has been investigated substantially less.

1.1.3 High Harmonic Generation

Attosecond duration XUV or soft X-rays are readily generated by up-conversion of optical or near infrared (NIR) light through a highly nonlinear process known as high harmonic generation (HHG). HHG is based on the interaction of a strong laser field with a nonlinear medium (typically a noble gas) and can described by the semi-classical 3-step model [29,30], illustrated in Figure 2.

In the first the step, the laser field modifies the atomic coulomb potential (grey, dashed), yielding a new potential (black), through which the electron can tunnel. In the second step, the electron is accelerated by the electric field, and it propagates freely picking up kinetic energy. In the third step, when the field reverses sign, the electron can recombine with the parent ion, releasing its kinetic energy in the form of a high energy XUV photon.

Under the 3-step model, the cutoff energy of the emitted harmonics E_c33 is given by:

$$E_c = 3.17 U_p + I_p \tag{1.1}$$

where I_p is the ionization potential of the medium, and U_p is the ponderomotive energy. Since $U_p \propto I\lambda^2$, where I and λ are the intensity and wavelength of the driving field, respectively, equation 1.1 provides a guideline for tuning the emission energy of HHG radiation. Many
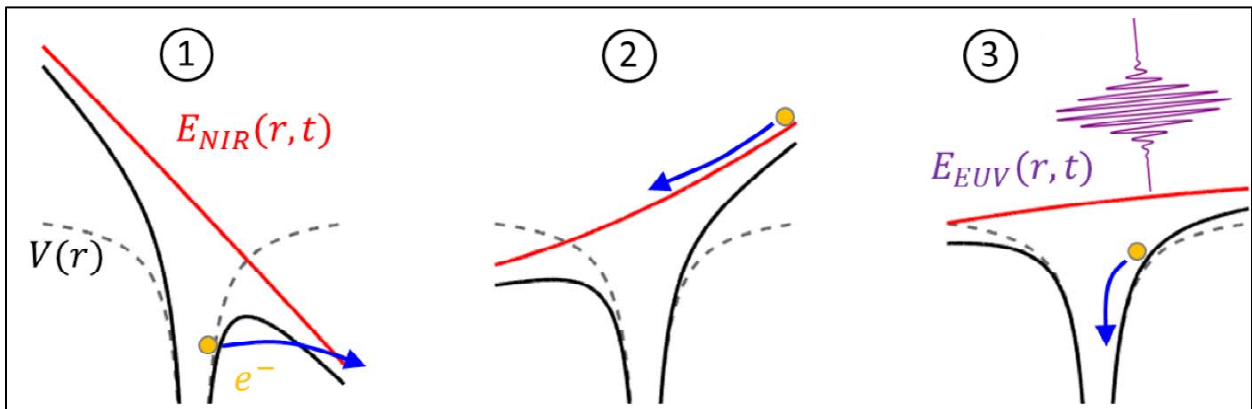
Figure 2: 3 step-model of high harmonic generation. 1: IR field (red) modifies the atomic coulomb potential, allowing an electron to tunnel ionize. 2: Electron freely propagates under electric field. 3: Electron recombines with parent ion, emitting a high-energy XUV photon.

groups have demonstrated the production of HHG radiation from the UV into the soft X-ray regimes [31,32].

Because only certain emission times will successfully lead to recombination, the resulting XUV radiation is emitted as attosecond bursts [33] every half cycle of the driving field. If XUV emission is somehow restricted to a single optical cycle, the resulting XUV light provides an isolated attosecond pulse, which can be used for attosecond resolution experiments. A large body of work is devoted to gating techniques, which restrict XUV emission events and allow the production of isolated attosecond pulses in the XUV and soft X-ray regimes [34–36].

1.2   Core-level spectroscopy

The XUV radiation created by HHG is energetic enough to liberate core level electrons, and as a consequence, XUV spectroscopy offers a number of benefits over traditional, optical spectroscopies. Because atomic core orbitals are separated in energy by 10 s or 100 s or eV, XUV and other core level spectroscopies provide element-specific information and can also be sensitive to spin state, orbital character, and oxidation state [37–39]. Because of the nature of the HHG process, tabletop generation of XUV by HHG allows access to this wealth of information with attosecond temporal resolution.

1.2.1 Electronic structure of solids

Because a solid is composed of ~10^{23} interacting atoms per cm^3, the electronic structure of a solid differs substantially from that of an isolated atom or small molecule. The electronic structure of an extended solid can be described by the solutions of the time independent Schrödinger equation (1.2)

$$\left[-\frac{\hbar^2}{2m}\nabla^2 + U(\vec{r})\right]\varphi = \epsilon\varphi \tag{1.2}$$

If the system possesses translational symmetry, i.e. if $U(\vec{r} + \vec{R}) = U(\vec{R})$ with spatial period $\vec{R}$, then the electronic wave functions (solutions to the eigenvalue problem in 1.2), can be represented as a so called Bloch wave [40]

$$\varphi_{\vec{k}}(\vec{r}) = e^{i\vec{k}\cdot\vec{r}}u_{\vec{k}}(\vec{r}) \qquad\qquad (1.3)$$

Here, the factor $u_{\vec{k}}(\vec{r})$ has the same periodicity as the crystal, and $\vec{k}$ parametrizes the wave vector (spatial frequency) of the wave function. The admissible $\vec{k}$ values span the Brillouin zone, $\vec{k} \in [0, \frac{2\pi}{R}]$, with a spacing of $2\pi/L$, where L is the length of the crystal. Because L is taken to be very large in a macroscopic solid, the corresponding energy eigenvalues $\epsilon(\vec{k})$ form a quasi-continuous distribution, called a band. Since electrons are fermions, under equilibrium the filling of bands can be described by a Fermi-Dirac distribution [2], with the distribution centered at the so called Fermi-Energy.

The precise form and occupation of these bands determines the electronic properties of the solid. At certain energies there may be no allowed $\vec{k}$ values, leading to a band gap between the occupied valence band and the unoccupied conduction band. Solids can be classified as metals – which have no band gap and are electrically conductive (resistivity $\approx 1\text{x}10^{-8}\ \Omega \cdot m$), insulators – which have a band gap $\gg k_b T$ and are electrically insulating (resistivity $\approx 1\text{x}10^{13}\ \Omega \cdot m$), or semiconductors – which have a moderate band gap and are moderately electrically conductive (resistivity $\approx 1\ \Omega \cdot m$) [41].

The Schrödinger equation (1.2) can be approximately solved under different regimes, corresponding to different physical situations. In systems with substantial delocalization, such as metals or semiconductors, a delocalized basis is used. This choice implicitly assumes that the system can be represented as a nearly free electron gas experiencing perturbations due to the periodic potential of the lattice. In more localized systems, such as ionic insulators, the solutions to equation 1.2 are represented as a linear combination of local functions similar to atomic orbitals [42], implicitly treating the extended solid as an extended chemical bond. The specific $\vec{k}$ dependence of $\epsilon(\vec{k})$, called a dispersion relation, is then determined by the overlap of the local basis functions on adjacent atoms. In valence states, which can have substantial overlap between adjacent lattice sites, $\epsilon(\vec{k})$ can show strong $\vec{k}$ dependence. Core states, by contrast, which have negligible overlap between adjacent lattice sites, have energies that have almost no $\vec{k}$ dependence.

1.2.2 XUV absorption

When a high energy photon interacts with matter, it can induce an electronic transition, resulting in an electric polarization of the material. Using time dependent perturbation theory, to first order the probability that a photon with energy $\hbar\omega$ will induce a transition from some initial state Φ_i (at energy E_i) to a final state Φ_f (at energy E_f), can be approximated by Fermi's Golden Rule [43]

$$\Gamma_{fi} = \frac{2\pi}{\hbar} \left| \langle \Phi_f | V' | \Phi_i \rangle \right|^2 \rho(E_f - E_i - \hbar\omega) \tag{1.4}$$

In equation 1.4, V' is the interaction Hamiltonian, and ρ is the density of final states. In the case of small $\hbar\omega$, the electric dipole approximation allows replacement of V' with the electric dipole operator $\hat{E} \cdot \vec{r}$ [44]. Assuming single particle transitions, Φ_f, Φ_i, and ρ can be taken to be a core-hole state, a ground state, and the initial density of states and equation 1.4 can be replaced with

$$\Gamma_{fi} \propto M^2 \rho(E_f - E_i - \hbar\omega) \tag{1.5}$$

for some constant M so long as $\langle \Phi_f | V' | \Phi_i \rangle$ is slowly varying as a function of energy. Because of the extremely flat dispersion of core orbitals, the density of core states reduces to a delta function, and Eq. 1.5 simply becomes the symmetry projected density of states. Because the absorption cross section $\sigma \propto \omega \Gamma_{fi}$, equation 1.5 indicates that XUV absorption, loosely speaking, probes the symmetry projected density of states.

1.2.3 The XUV dielectric function and observables

The electric polarization induced when an electric field interacts with matter, described in the previous section, can also be described by the electric susceptibility [45] (equation 1.6)

$$\vec{P}(\omega) = \varepsilon_0 \chi(\omega) \vec{E}(\omega) \tag{1.6}$$

where $\vec{P}$ is the polarization density, ε_0 is the permittivity of free space, and $\vec{E}(\omega)$ is the incident electric field. In condensed matter, which can support both free and bound charges, the more relevant quantity is electric displacement $\vec{D}(\omega)$

$$\vec{D}(\omega) = \varepsilon_0 \vec{E}(\omega) + \vec{P}(\omega) = \varepsilon_0 (1 + \chi(\omega)) \vec{E}(\omega) = \varepsilon_0 \varepsilon_r(\omega) \vec{E}(\omega) \tag{1.7}$$

where the proportionality constant $\varepsilon_r(\omega)$ is the dielectric function, which describes the electric displacement for a given electric field. Because $\vec{D}(\omega)$ may be out of phase with $\vec{E}(\omega)$, $\varepsilon_r(\omega)$ is complex, where the real part ε_1 describes the in phase response of the electric displacement, and the imaginary part ε_2 describes the out of phase response.

The dielectric function describes the polarization response of a material to an electric field. Consequently, it is intimately related to processes such as absorption, reflection, and refraction, which all depend on the polarization of a material in response to an electric field. For a nonmagnetic material, the complex valued refractive index $\tilde{N}$ is related to the dielectric function

$$\varepsilon_r = \varepsilon_1 + i\varepsilon_2 = \tilde{N}^2 = \left(\tilde{n} + i\tilde{k}\right)^2 \tag{1.8}$$

where $\tilde{n}$ and $\tilde{k}$ are the real and imaginary parts of the refractive index.

When an electric field $E(\omega)$ travels from vacuum to a material with refractive index interface $\tilde{n} + i\tilde{k}$ it experiences a phase shift due to polarization of the material, and consequently part of the field may be absorbed, part reflected, and part transmitted (Figure 3). If $\tilde{k}$ is non zero, the phase shift will be complex, and the intensity of the field will decay within
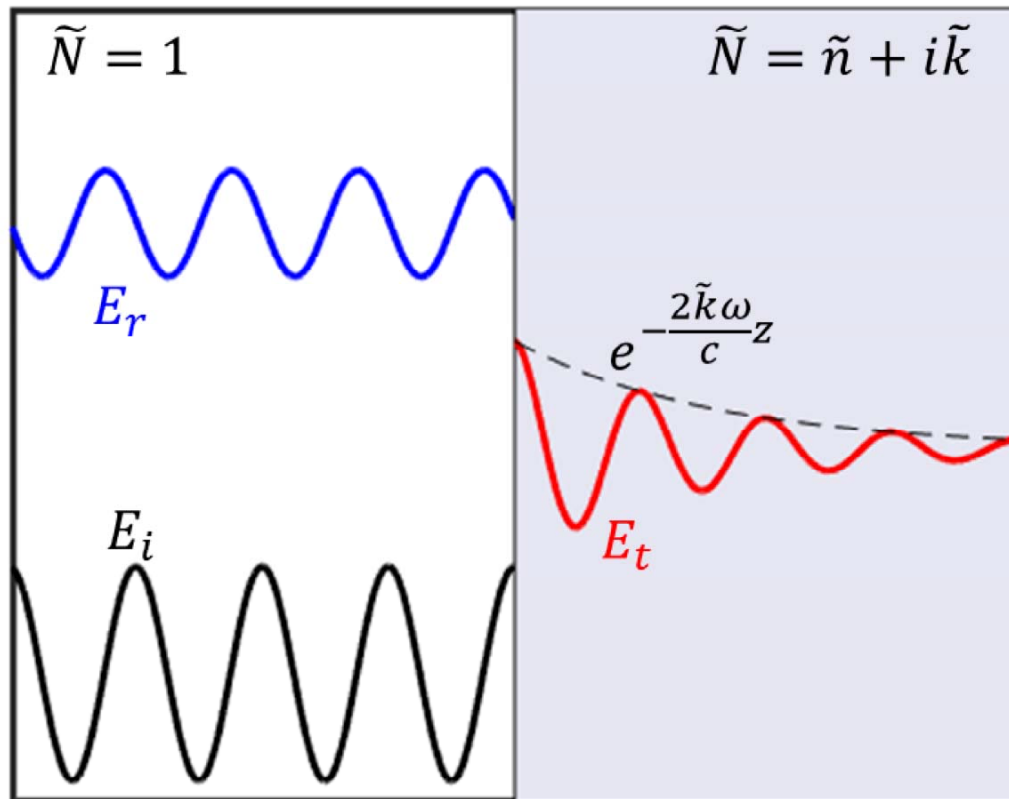
Figure 3: An incident electric field (black), with the reflected field (blue), and transmitted field (red). The transmitted field is attenuated due to absorption in the material.

the material by a factor of $e^{-\alpha z}$, where z is the distance into the material, α is the absorption coefficient,

$$\alpha = \frac{2\tilde{k}\omega}{c} \tag{1.9}$$

and c is the speed of light. Because the imaginary part of the refractive index determines the attenuation of light in a solid, $\tilde{k}$ is known as the extinction coefficient.

The polarization of the material can also result in a reflected field, the intensity of which is given by the Fresnel equations. At normal incidence, the Fresnel equation for the reflected intensity of a field incident from vacuum onto a material with refractive index $\tilde{N}$ is

$$R = \frac{I_r}{I_0} = \left|\frac{1-\tilde{N}}{1+\tilde{N}}\right|^2 \tag{1.10}$$

where I_r is the reflected intensity and I_0 is the incident intensity. The quantity in Equation 1.10, is known as the reflectivity and it may in practice differ from the true observed reflected intensity (reflectance) due to surface scattering, imperfections in the interface, or other phenomena. Accordingly, 1.10 is only strictly valid for an optically thick, infinitely smooth, infinitely sharp interface. In the case of a rough interface, the Debye-Waller correction has been shown to provide accurate results [46], while for multilayer structures, a matrix formalism has been developed to account for multiple reflections [47].

1.2.4 Advantages of XUV reflection

From Equation 1.10, it is apparent that reflectivity is sensitive to the complex dielectric function of a material, and thus in principle it provides all the same information as an absorption experiment. Additionally, previous work has shown that reflectivity can be sensitive to surface morphology, and it can provide selective surface or bulk sensitivity depending on the angle of incidence [48,49].

XUV reflectivity provides several key advantages over an absorption measurement. Because XUV absorption requires measuring transmitted light, its scope is limited to very thin films (often ~50 nm). These samples can be challenging to fabricate and suffer from high defect densities, low thermal conductivity, and may be difficult to characterize. As a consequence, results from XUV absorption in solids can be difficult to generalize into physical insights about the system of interest, and the results may often be more representative of the specific defect

structure of the material than the true underlying physical process [21]. XUV reflectivity overcomes these limitations by allowing investigation of optically thick, single crystal materials [50,51].

1.2.5 Lorentz-Drude model

In some cases [52], the electric polarization of a material can be phenomenologically described as that of a simple classical, damped harmonic oscillator. From Newton's second law, the relevant equation of motion [53] is given:

$$\frac{d^2P}{dt^2} + \gamma\frac{dP}{dt} + \omega_0^2 P = \frac{Nq^2}{m}E(\omega) \tag{1.11}$$

Where P is the polarization density, γ is the damping constant, ω_0 is the resonant frequency, q is the elementary charge, m is the mass, N is the number of oscillators participating, and E is the driving field. Solving equation 1.11, inserting into equation 1.7 and substituting $\omega_p = \sqrt{\frac{Nq^2}{m\varepsilon_0}}$, gives the following result for the dielectric function:

$$\varepsilon_r = \varepsilon_c + \frac{\omega_p^2}{\omega_0^2 - \omega^2 - i\gamma\omega} \tag{1.12}$$

In equation 1.12, ε_c is the static background dielectric function. The dielectric function shown above, known as the Lorentz-Drude model, is a widely used model for understanding and modeling dielectric functions in an array of materials [52].
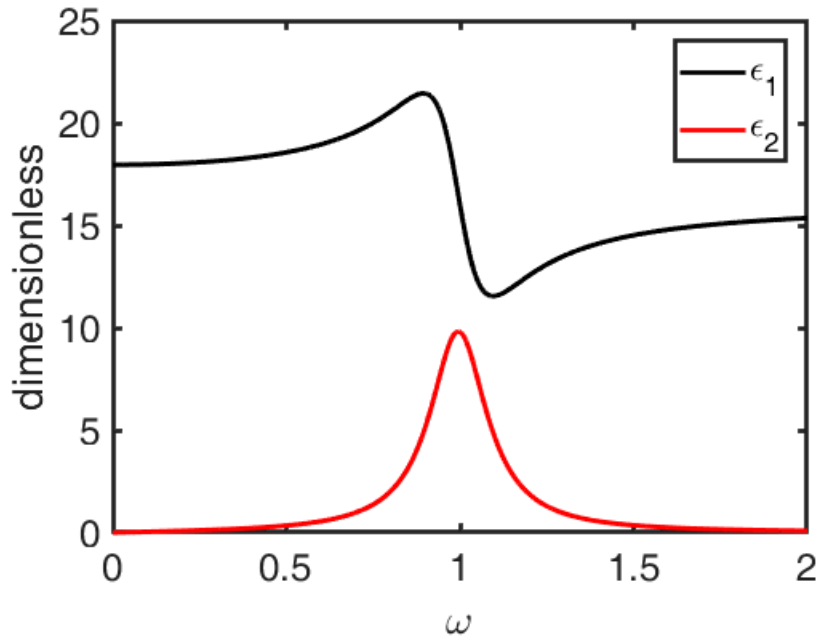
Figure 4: Real (black) and imaginary (red) parts of hypothetical Lorentz-Drude dielectric function.

An example Lorentz-Drude dielectric function is shown in Figure 4. The imaginary part (red), shows a characteristic lineshape near resonance that is approximately (though not quite) Lorentzian ($1/1+\omega^2$). In contrast, the real part shows a characteristic "dispersion" lineshape near resonance. Clearly, in the large ω limit, (as is approximately the case for XUV and X-ray regimes), ε_r approaches a constant real value, and the imaginary part vanishes.

1.2.6 Absorption and reflection: An intuitive comparison

According to equation 1.10, when $\tilde{N}$ is small (as is generally the case in the XUV or X-ray regime), R drops substantially. Counterintuitively, Equation 1.10 also implies that strongly absorbing materials (with large $\tilde{k}$) reflect more light. For materials in which $\tilde{k}$ becomes very large, (such as metals in the low frequency regime), R approaches unity, and the transmitted beam is attenuated within one or two wavelengths into the material. For small $\tilde{k}$, equation 1.10 implies that at normal incidence, reflectance and absorption spectra look qualitatively similar; however this is only very approximately true and becomes less correct when moving from normal incidence to more grazing angles.

The complex nature of the relationship between reflectivity and absorption can be clearly seen by examining the normal incidence reflectivity and the absorption for two different Lorentz-Drude oscillators Figure 5. In one model with low extinction coefficient (left),
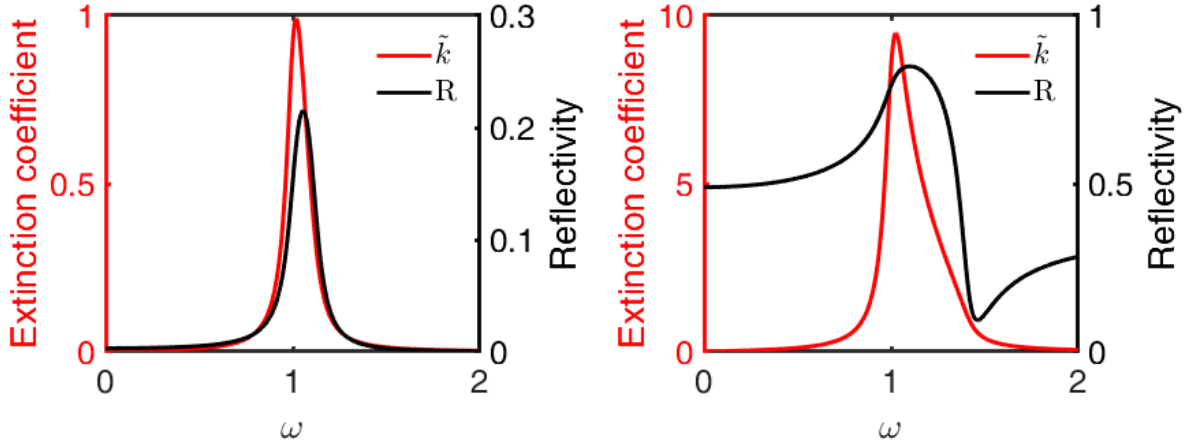
Figure 5: Extinction coefficient (red) and normal incidence reflectivity (black) for two different Lorentz-Drude oscillator models, in which reflectivity resembles (left) absorption, and differs from (right) absorption. Parameters used Left: ε_c , ω_p , ω_0 , γ = 1, 0.5, 1, 0.1 respectively. Right: ε_c , ω_p , ω_0 , γ = 16, 4, 1, 0.1 respectively.

reflectivity and absorption strongly resemble one another. In another model with higher extinction coefficient and core dielectric function, reflectivity shows a characteristic dispersion shape, while absorption still shows a single characteristic (though no longer Lorentzian) peak. The present discussion illustrates that because of the complex relationship between reflectivity and absorption, the simple correspondence between XUV absorption and the density of states does not hold for reflectivity and the density of states. Consequently, detailed analysis of XUV reflectivity is required to extract information about the dielectric function, and the microscopic information it reports on.

1.2.7 Bulk vs surface sensitivity of reflectivity

The expression in equation 1.10 is derived by solving Maxwell's equations assuming an infinitely sharp discontinuity at the interface. As such, it implicitly assumes that all reflection occurs at the interface, suggesting that reflectivity probes only the dielectric function at the interface, and is 100% surface sensitive. In real systems, the surface and bulk dielectric function may differ substantially due to a number of factors, including the breaking of the translational symmetry [54] that is assumed in the derivation of equation 1.3, the presence of topologically

protected surface states [55], or the surface preferential excitation of the sample in a pump-probe experiment. Consequently, the question of how sensitive reflectivity is to the surface or bulk dielectric function is of great interest in interpreting reflectivity results. Several studies have investigated reflectivity from an inhomogeneously excited solid to determine the effective probe sensitivity depth [48,56,57]. In one study [48], the authors use perturbation theory to solve the wave equation for a spatially dependent dielectric function of the form

$$\tilde{\varepsilon}(z) = \tilde{\varepsilon}_0 - \tilde{\eta}e^{-z/\delta} \tag{1.13}$$

where $\tilde{\varepsilon}_0$ is the bulk dielectric function, $\tilde{\varepsilon}_0 - \tilde{\eta}$ is the surface dielectric function, and δ is a parameter that describes the "steepness" of the dielectric function change near the surface. In the limit of small δ, the changes in the optical constants occur very close to the surface, and we would expect the reflectivity to resemble that of the bulk dielectric function $\tilde{\varepsilon}_0$. Conversely, in the limit of large δ, the dielectric function changes slowly within the material, and we expect the reflectivity to resemble that of the surface dielectric function $\tilde{\varepsilon}_0 - \tilde{\eta}$. By assuming linear polarization and normal incidence, the authors show that the observed reflectivity smoothly transitions between these two regimes as δ is varied. They define an effective sensitivity depth of $\delta = d_{obs}$ where the measured reflectivity is halfway between that of the bulk and surface values. They show that

$$d_{obs} = \frac{\lambda}{4\pi|\tilde{N}|} \tag{1.14}$$

where λ is the probe wavelength, and $\tilde{N}$ is the complex valued refractive index of the bulk. Note that d_{obs} is always less than or equal to the penetration depth of the probe $\lambda/(4\pi|\tilde{k}|)$, and can in fact differ by over an order of magnitude. For example, in Germanium at 31 eV, the probe penetration depth is approximately 53 nm, while d_{obs}= 3 nm. The above discussion is of course only valid for normal incidence, but at non-normal incidence, d_{obs} should scale linearly with the projection of the propagation vector along the surface normal. Additionally, this discussion is only strictly valid for low excitation. For a full analytical treatment valid in any regime, see [56,57]. These studies illustrate that XUV reflectivity is in general substantially more surface sensitive than would be suspected based on the probe penetration depth.

Chapter 2: Experimental apparatus for XUV transient reflectivity and recovery of static refractive index

Some content and figures of this chapter are reprinted or adapted with permission from Peter M. Kraus, Eric M. Gullikson, L. J. Borja, Scott K. Cushing, Michael Zürch, and Hung-Tzu Chang.

"Retrieval of the complex-valued refractive index of germanium near the $M_{4,5}$ absorption edge," J. Opt. Soc. Am. B., [Under Review], (2019)

In the first part of this chapter, the instrumentation developed to implement XUV transient reflectivity is described. The resulting design allows provides excellent temporal and energy resolution, and allows study of ultrafast dynamics in highly ordered crystalline solids. In subsequent chapters, studies of ultrafast dynamics in solids are described in more depth.

In the second section, the complex valued index of refraction of germanium in the extreme ultraviolet (XUV) is measured by multi angle reflectance of synchrotron radiation. The resulting index of refraction is higher resolution than previously measured values. It reveals new structures attributed to transitions from the 3d core orbitals to the $\Sigma_{5,2}{}^c$ and the $X_{5,2}{}^c$ conduction bands. Additionally, it is shown that the problem of total external reflection, which renders multi angle reflectance measurements insensitive to the refractive index at grazing incidence, can be overcome by employing measurements at angles of incidence away from the critical angle.

2.1   Experiment overview

The apparatus used in this work (Figure 6) consists of an 800nm Ti:sapphire laser, which is used to generate high harmonics (HHG), a toroidal focusing mirror, a sample, a variable time delay line, a variable line spaced grating, and an X-ray CCD camera to detect the reflected signal from the sample. The carrier-envelope phase (CEP) stabilized 800nm Ti:sapphire laser

(1.8mJ 1kHz) is spectrally broadened in a Neon filled hollow core fiber (1 Bar) to yield a white light continuum spanning 550-1000 nm. The pulses are compressed using a set of dielectric chirped mirrors (Ultrafast Innovations) and 2mm of ammonium dihydrogen phosphate (ADP) [58], yielding compressed pulses with 3.5fs temporal duration, as characterized by dispersion scan. [59] Few-cycle compression is a prerequisite for generation of an XUV continuum, which greatly enhances signal to noise over the required large XUV bandwidth in
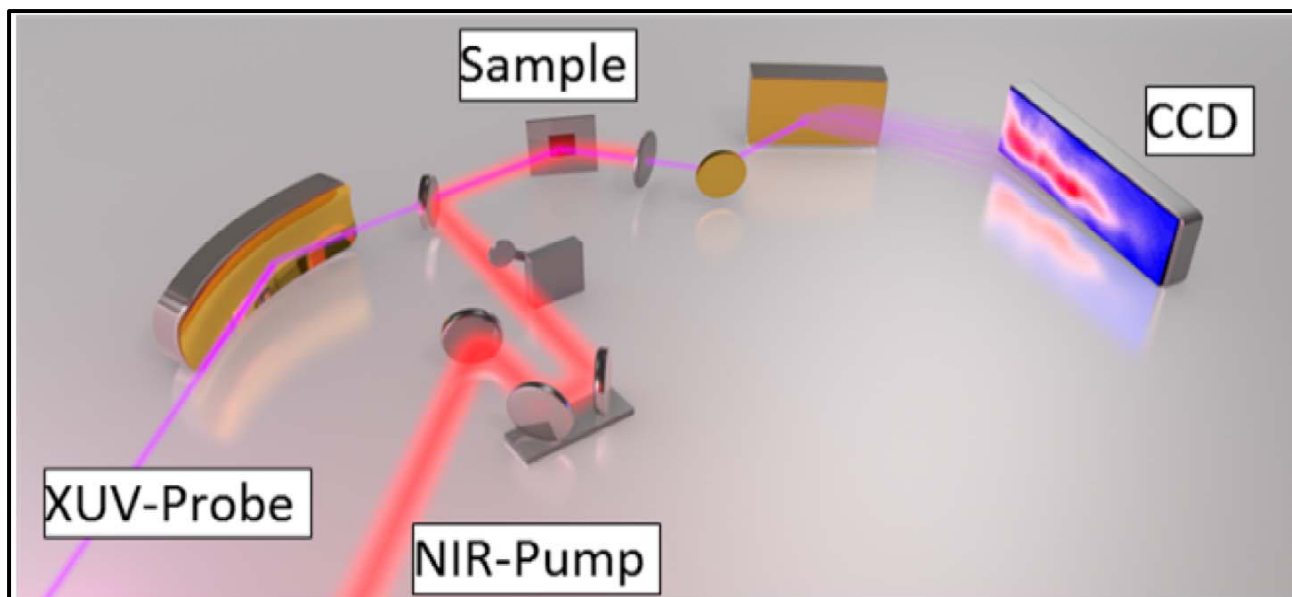
Figure 6: Experimental apparatus for pump-probe transient reflectivity. A time delayed XUV pulse probes transient reflectivity in single crystal germanium, after excitation with a few cycle NIR pump pulse.

the experiment. The resulting NIR and characterization are shown below in Figure 8. Briefly, the pump pulse (bottom left, red curve), is frequency doubled using a beta barium borate (BBO) optic, yielding a frequency doubled spectrum (bottom left, blue curve). The doubled frequency is then modified by introducing wedges of known dispersion, yielding a second harmonic spectrum as a function of wedge insertion (top left panel). A reconstruction algorithm then retrieves the phase and electric field of the linear spectrum, indicating a short pulse of 3.7 fs (FWHM).

The compressed output is split with a 60:40 beam splitter. Sixty percent of the energy (480 μJ) is used to generate the probe via HHG. High harmonics are produced by focusing into a Xe gas target with backing pressure ~24mTorr, yielding continuous harmonic spectra from 25-40 eV. The resulting XUV spectrum is shown in Figure 7. The spectrum is highly continuous

and shows strong CEP dependence, indicating that the XUV probe is a near isolated attosecond pulse.

Residual NIR from the generation process is removed with a 100 nm thick Al filter. The XUV probe is then focused onto the sample using a grazing incidence gold-coated toroidal mirror. The remaining 40% pump of the energy is time delayed using a retroreflector on a piezostage and recombined collinearly with the probe using an annular mirror. The NIR pump pulse is focused to 200 μm (FWHM) diameter onto the sample, and the XUV beam is focused to ~20 μm (FWHM) diameter.
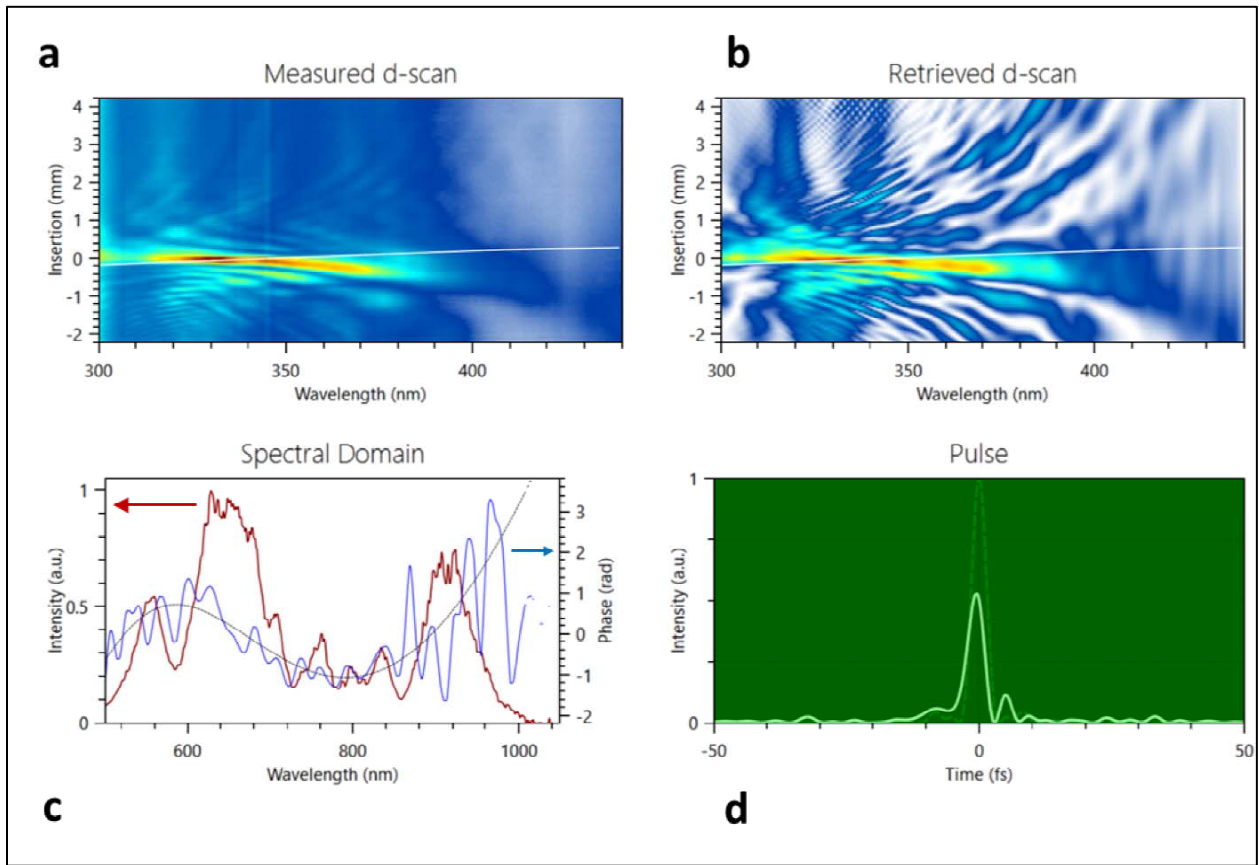
Figure 8 Characterization of pulses using Dispersion Scan. (a) Measured second harmonic intensity as a function of wedge insertion. (b) Retrieved second harmonic intensity using simulated pulse. (c) Pump spectrum (red), phase (blue) and polynomial fit of phase (black line). (d) Retrieved pulse intensity has a duration of 3.7 fs FWHM.
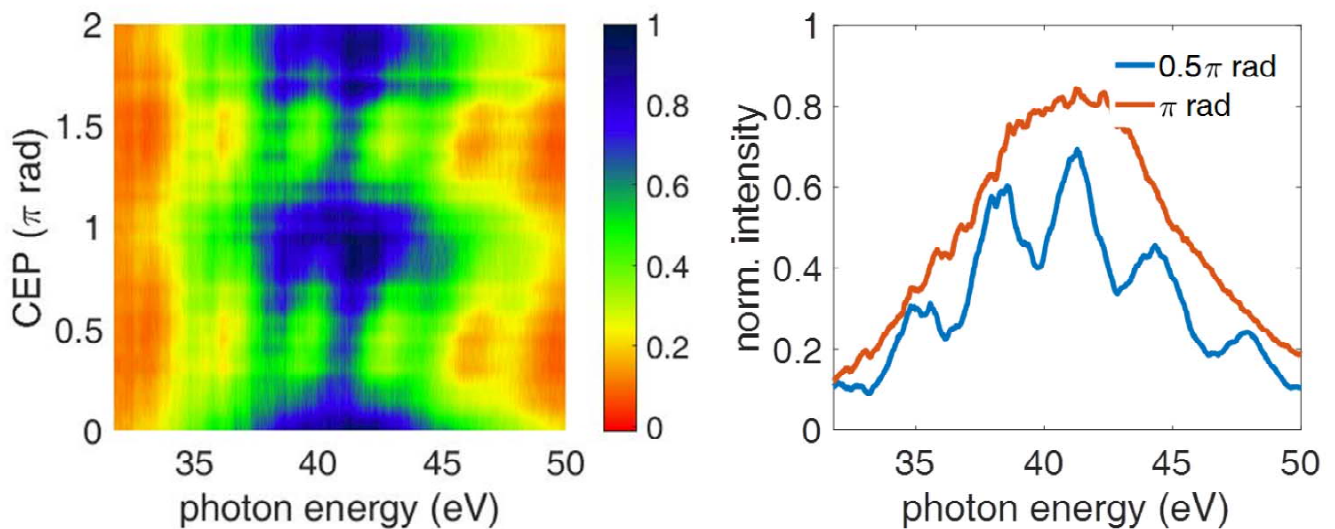
Figure 7: CEP dependence of XUV spectrum from HHG in Xe. Left, XUV spectrum for CEP values between 0 and 2π. Right: CEP values at $\pi/2$ and π allow turning of HHG spectrum from discrete to continuous.

2.1.1 Calibration of XUV spectrometer

Because the sample is part of the beam path in a reflectivity measurement, accurate calibration of the XUV spectrometer is essential, and the calibration must be performed any time the sample is moved. A motorized gas cell can be inserted approximately 1 inch before the sample, allowing observation of atomic absorption lines in neon [60] between 45-48 eV and argon [61] between 26-29 eV. These lines are used for an energy calibration of the spectrometer by a linear fit of pixel vs wavelength [62].
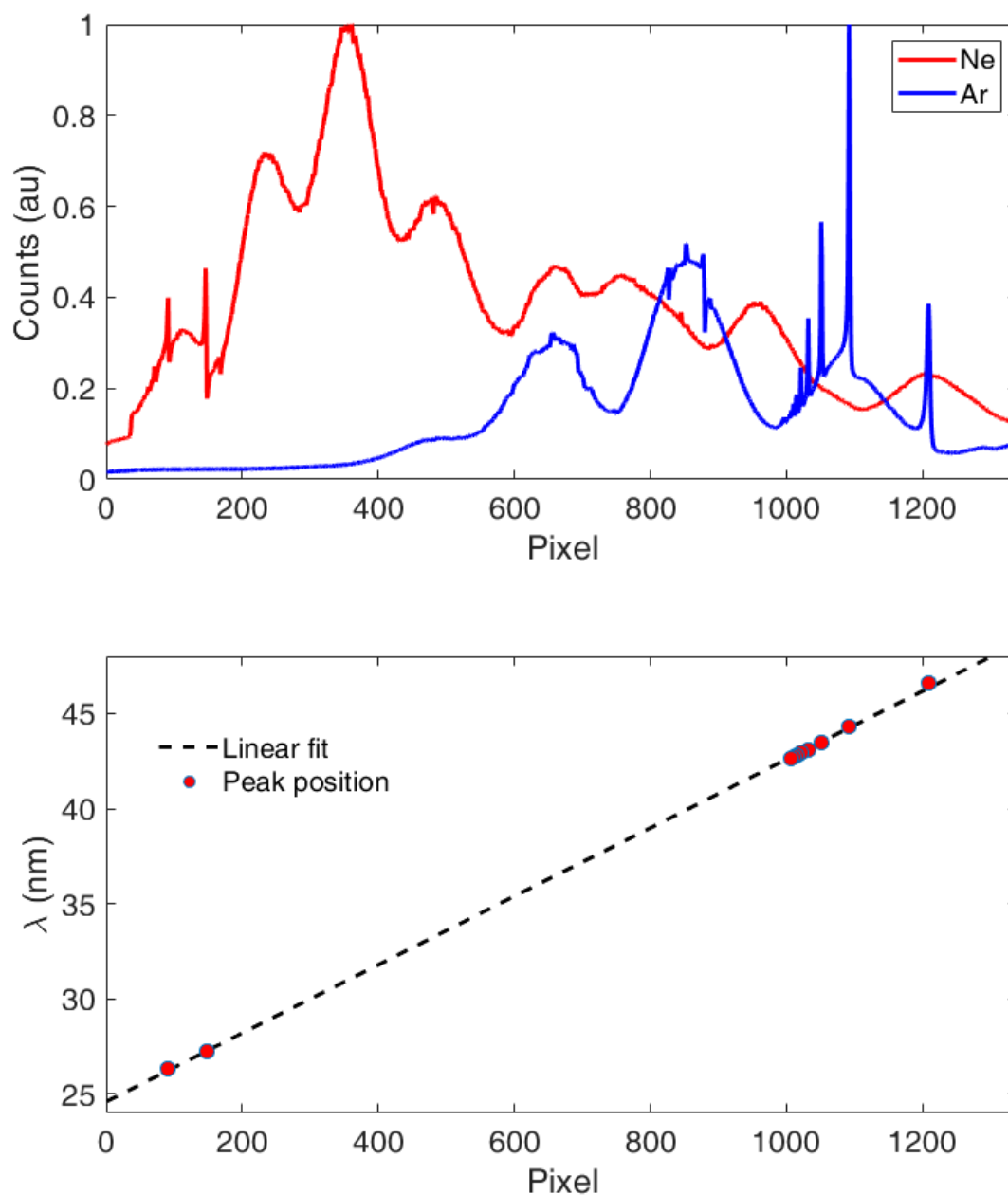
Figure 9(Top) Transmitted XUV spectra through gas cell containing Neon (red), and Argon (blue), showing atomic absorption lines used for energy calibration. (Bottom) Linear wavelength calibration obtained (black, dashed), from fit of atomic peak positions (red, scatter).

Example XUV transmittance spectra through Ne and Ar shown in Figure 9(top) show sharp atomic transitions corresponding to separate Rydberg series of 2p excited states in Neon, and 3s excited states in Argon, which have previously been assigned. [63,64] The resulting calibration obtained Figure 9(bottom) provides a linear relationship between pixel and wavelength, as would be expected from diffraction under small angles. Additionally,

determining the resolution by deconvoluting the natural line shapes of the atomic absorption lines in argon with the spectrometer resolution as described in Ref. [62]. We found our resolution to be 40 meV at 28 eV.

2.1.2 Implementation of reflection beam path

Implementing the reflectivity setup shown in Figure 6 required modification of a previously functioning absorption beam path. A top down view of the experimental chamber of the previous absorption beam path is shown in Figure 10. Briefly, the XUV beam generated by HHG is transmitted through a thin film sample mounted on an XY translation state, dispersed with an aberration corrected variable linewidth XUV grating, and imaged on a CCD.

The newly implemented reflectivity beam line is shown in Figure 11. In this configuration, the previous sample mount has been replaced with a mount which allows for rotation as well as XY translation. The beam path is then corrected by reflection off of a 2nd reflection off of an Au mirror with known reflectivity, dispersed with a new XUV grating, and imaged on a CCD. Implementing these changes involved minimal modification to the existing beam path, allowing for quick experimentation and iteration with multiple designs.
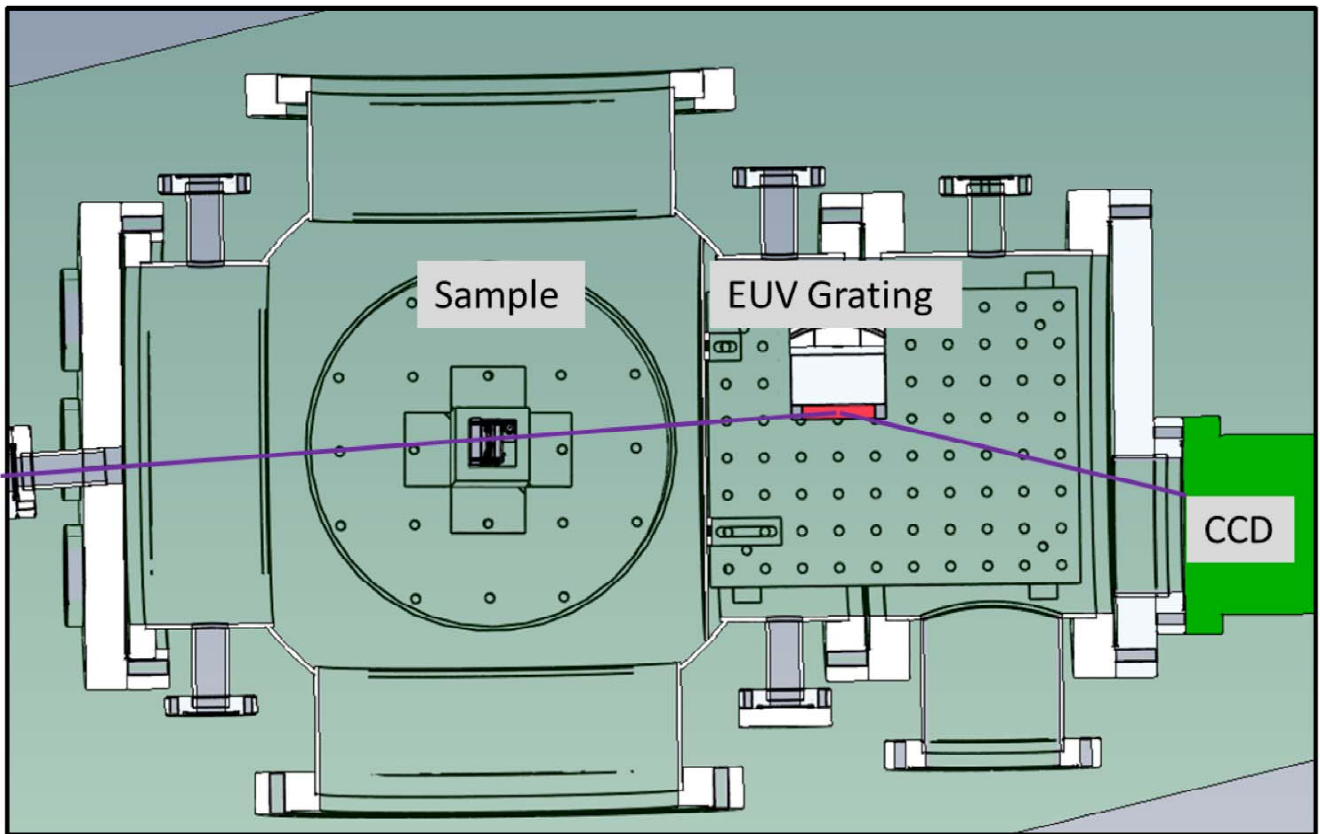
Figure 10: Top down view of experimental chamber of previous absorption beam path. XUV (purple), transmitted through sample on XY stage is dispersed with XUV grating and imaged on CCD.
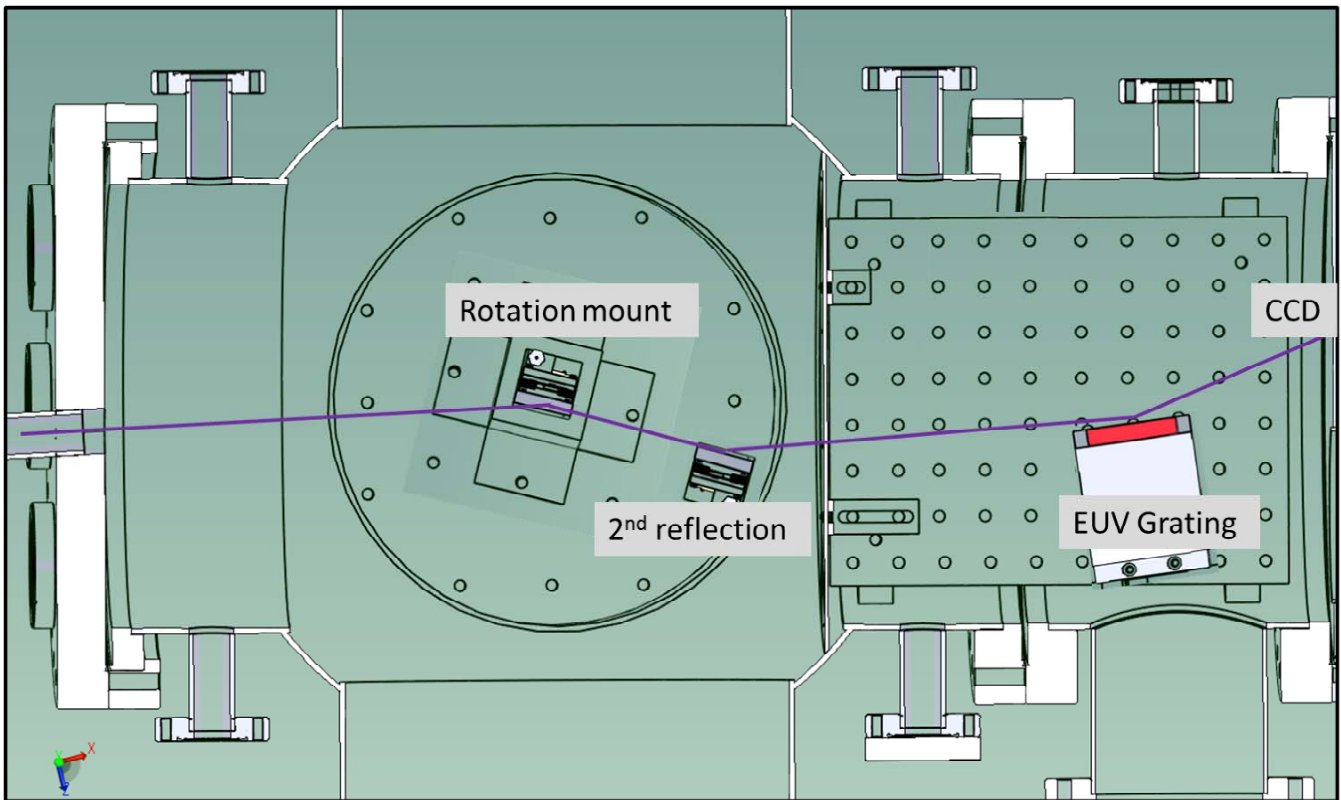
Figure 11: Top down view of experimental chamber of newly implemented reflectivity beam path. XUV (purple) is reflected off of sample on rotation mount with XY translation, corrected by a 2nd reflection off of an Au mirror, dispersed with XUV grating and imaged on CCD.

2.1.3 Time referencing for attosecond temporal stability

In order to maintain subfemtosecond temporal stability, a gas phase temporal referencing scheme, similar to previously published methods is adopted [65]. The motorized gas cell used for energy calibration allows for evaluation and stabilization of the pump-probe time delay. Passive stability of the setup is verified by recording time-dependent four wave-mixing signals by exciting the autoionizing states of neon around 45 eV with XUV/NIR pulses, perturbing the induced polarization decay with a time delayed NIR pulse. The simultaneous excitation of neon with XUV/NIR pulse is achieved by removing the aluminum
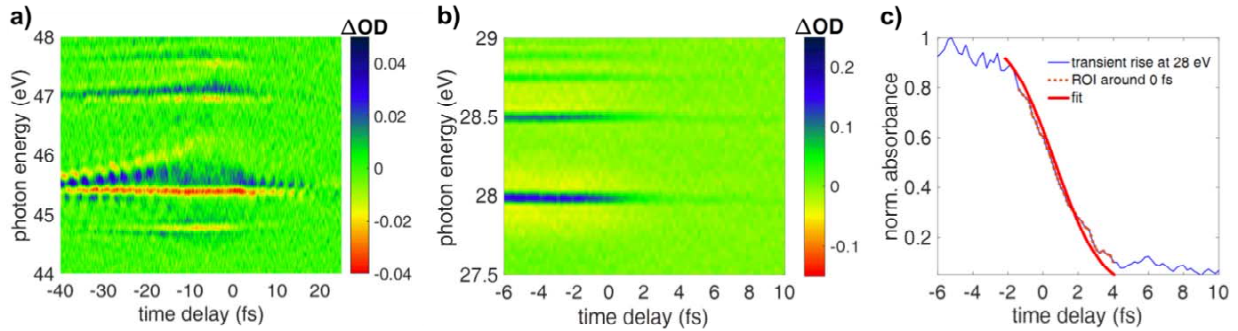
Figure 12: **Transient absorption measurement of gas transients for time-delay referencing**: (a) Collinear four wave mixing signal in the Neon 2s→3p transition, which is used for verifying passive stability of the setup. (b) Transient absorption measurement of 3s excitations to autoionizing np states in argon for time-delay referencing. (c) Lineout (blue line) of the 3s→5p transition at 28.02 eV. The fit (red line) to the rise of the transient feature (ROI shown as dotted orange line) is used for delay referencing.

filter after the HHG target. The transient is shown in Figure 12a. Clear oscillations with frequency of 1.6 eV (2.6 fs period) are present due to the simultaneous excitation of 2s inner valence electrons into 3s and 3d valence states by XUV/NIR pair, which are then probed by the second NIR pulse that couples the 3s and 3d valence states by a one photon transition to the common final 3p state. Here, the 2.6 fs oscillations serve as a verification of the passive stability of our setup.

Long-term stability for carrying out measurements over many hours is ensured by measuring a transient Argon autoionization line transformation near 28 eV, as shown in Figure 12b. The sharp rise of the line shape change is fit with an error function (Figure 12c) and can be used to detect the center of the rise time with an accuracy that is given by the sampling frequency. This delay correction scheme allows for a permanent absolute time referencing

over many hours, and gives real time feedback on the current pump intensity and pump-probe overlap through the transient changes in the optical density at the energy of the autoionizing line. Gas transients are recorded after every sample measurement over the full delay range, which amounts to a transient measurement ever 5-10 minutes. Many sample scans (10-100) are typically averaged to obtain a satisfactory signal-to-noise ratio.

2.2   Recovery of static refractive index of Germanium

The complex refractive index describes the linear optical properties of a material, directly providing the reflection of light from a surface and the absorptivity of the material [66]. The refractive index is intimately tied to the electronic structure of solids; in the visible wavelength regime, it reports on transitions from the valence to conduction band, while in the extreme ultraviolet (XUV) or X-ray regimes, it probes transitions from core states into the conduction band. The current industrial development of extreme ultraviolet lithography at 13.5 nm will eventually require the extension of existing optical metrology techniques into the extreme ultraviolet [67,68]. Such techniques require knowledge of the broadband complex refractive index. Because of the element-specific nature of core-conduction band transitions, XUV absorption, and the corresponding complex valued refractive index provide a wealth of information with high sensitivity to atomic number, spin state, and orbital character [38,69,70].

Additionally, as attosecond time-resolved measurements in solids become more common [15,18,19], there is increased interest in studying XUV refractive indices [50,51,71] as the center frequency of attosecond pulses necessarily lies in the extreme ultraviolet part of the spectrum. These properties make attosecond pulses very attractive for studying element-specific core-to-valence excitations, allowing the tracking of ultrafast oxidation state changes [72] and charge transfer processes [73,74]. Analysis of these measurements relies heavily on high quality refractive indexes in the XUV spectral range, which may not be available because synchrotron studies typically focus on harder x-rays.

Germanium (Ge) is a ubiquitous semiconductor, with diverse applications ranging from sensors to photovoltaics [75,76]; it has more recently been studied extensively using XUV time resolved spectroscopies to follow both electrons in the conduction band and holes in the valence band [21,50,77]. In these studies, carrier dynamics were tracked near the Ge $M_{4,5}$ absorption

edge from ~28-33 eV, and analysis required knowledge of the complex-valued dielectric function in this spectral range. The complex valued dielectric function of germanium has been retrieved in the visible to near-ultraviolet part of the electromagnetic spectrum through full ellipsometry of reflected light from a Ge surface [78,79] and the results have been related to underlying valence-to-conduction band transitions [80]. Characterization of the dielectric function at higher photon energies up to 25 eV was achieved through combined reflectance and transmittance measurements in combination with a Kramers-Kronig transform [81–83].

The complex refractive index of germanium in the XUV was previously obtained through multi-angle reflection measurements [84] and by Kramers-Kronig analysis of atomic photoabsorption cross sections [85]. Both studies revealed the clear signature of the Ge $M_{4,5}$–edge around 29.5 eV, but lacked the energy resolution required to observe more detailed structure above the edge. Another study obtained more detailed high-energy structures in the normal incidence reflection spectrum of Ge [86], but it did not retrieve a refractive index for those energies. In this work, we employ multi angle reflectance measurements to recover the complex-valued refractive index of germanium around the $M_{4,5}$–edge, providing access to the high energy structures previously observed in Ref [86], giving access to several new structures, and allowing unambiguous assignment of the features present.

2.2.1 Materials and methods:

Germanium single-crystal wafers of 500 μm thickness, <100> orientation, with surface roughness less than 1 nm, were purchased commercially from University Wafers and stored
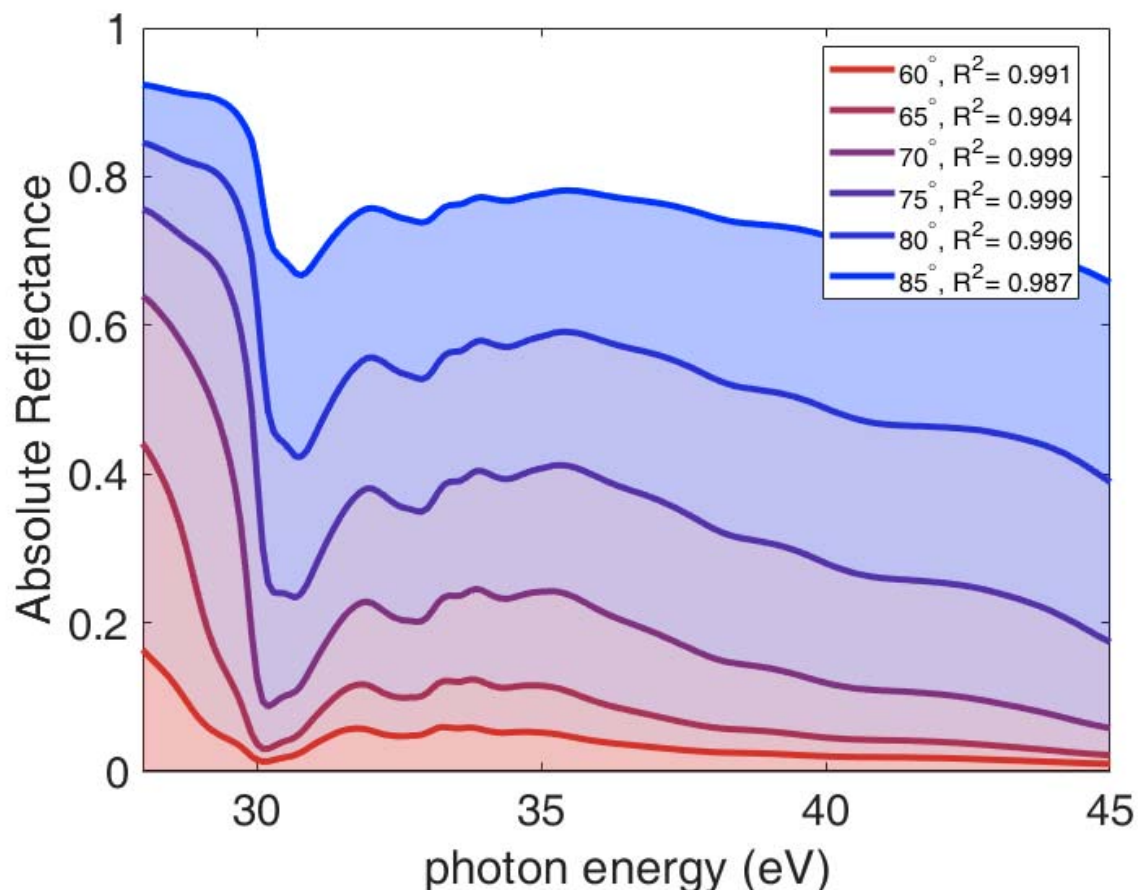
Figure 13 Experimentally measured Reflectance of Ge at 60°, 65°, 70°, 75°, 80°, and 85° from the normal at room temperature. R^2 shows quality of the overall recovery fit for the refractive index based on the data from each angle, obtained using equation 1 (see text).

under nitrogen until use. In Ref. [87] it was found that the oxide of Ge grows by less than one nm during one day, which minimizes possible surface contamination that could affect the measured refractive index. The absolute reflectance was characterized at the synchrotron facilities of the Advanced Light Source (ALS) (Beamline 6.3.2) at the Lawrence Berkeley National Laboratory (LBNL) by measuring the reflectance at six different angles of incidence (60, 65, 70, 75, 80, 85 with respect to the surface normal) for s-polarized XUV light. The reflectivity setup has been described elsewhere [88]. Beamline 6.3.2 uses a variable line spaced

plane grating and slit to select wavelengths with a wavelength precision 0.007% and a width of $\Delta\lambda/\lambda$=0.0123%. The beam is then focused onto the sample in a 10 μm x 300 μm spot size and reflectance is measured with an uncertainty of 0.08% in steps of 0.09 eV. The measured reflectance is shown below in Figure 13. The measured reflectance generally decreases with increasing angle of incidence. Moreover, there is a sharp drop and subsequent rise near 29.5 eV, which has previously been assigned to the Ge $M_{4,5}$ absorption edge attributed to transitions from the spin orbit split $3d_{5/2,\,3/2}$ core levels to the conduction band.

2.3 Results and discussion

2.3.1 Recovery of refractive index

The complex refractive index $\tilde{n}$ of a material in the XUV is typically written as $\tilde{n}(\omega) = n(\omega) + i\kappa(\omega)$, where $n(\omega)$ is the real part of the refractive index and $\kappa(\omega)$, is the imaginary part. In general, n describes the phase shift of the incident light per cycle, while κ describes the attenuation of the incident light per cycle. The absolute reflectance R_s for s-polarization is given by the modified Fresnel equation:

$$R_s = \left| \frac{\cos\theta_i - \sqrt{\tilde{n}^2 - \sin\theta_i^2}}{\cos\theta_i + \sqrt{\tilde{n}^2 - \sin\theta_i^2}} \right|^2 e^{-\sigma^2 q^2} \tag{2.1}$$

Here θ_i is the angle of incidence measured with respect to the surface normal and $e^{-\sigma^2 q^2}$ is the Debye Waller factor, which describes the attenuation of the reflected beam due to scattering at an interface with roughness σ, for incident light with scattering vector $q = 4\pi \sin\theta_i / \lambda$. [89] Under our conditions, σ=1 nm and $e^{-\sigma^2 q^2}$ ranges from 0.9-0.99. Consequently, surface scattering has a fairly small effect on the reflectance.

In order to retrieve the refractive index, a numerical nonlinear least-squares solver is employed to iteratively reconstruct n and κ using equation 2.1 and the reflectance at the 6 different angles shown in Figure 13. The quality of the fit, assessed by the coefficients of determination R^2 shown in Figure 13, is above 0.98, indicating that equation 2.1 can well describe the reflection behavior of the sample. To calculate the uncertainty in the recovered

refractive index, the revival algorithm used to recover n and κ is run on $\vec{R}_0 + \delta\vec{R}$, where $\vec{R}_0$ is the set of measured reflectances $\vec{R}_0 = [R(\theta_1), R(\theta_2) \dots, R(\theta_6)]$, $\delta\vec{R} = [\pm\delta R(\theta_1), \pm\delta R(\theta_2) \dots, \pm\delta R(\theta_6)]$, and $\delta R(\theta_n)$ is the uncertainty in the reflectance measured at angle θ_n [90,91]. In this work, $\delta R(\theta_n)$ was taken to be 0.08% of $R(\theta_n)$ based on the previously measured error of the beamline [88]. Because each of the six components of $\delta\vec{R}$ can take on two possible values $(\pm\delta R_i)$, the recovery algorithm was run $2^6=64$ times, once for each possible value of $\delta\vec{R}$. Error bars were taken from the recovered n and κ values maximally displaced from the refractive index associated with $[R(\theta_1), R(\theta_2) \dots, R(\theta_6)]$. The resulting refractive index, and corresponding uncertainty is shown in Figure 2. The mean errors for n and κ (0.06% and 5.9% respectively), differ by two orders of magnitude, indicating that this procedure is much more accurate for n than κ. (See section 2.3.3 for details).
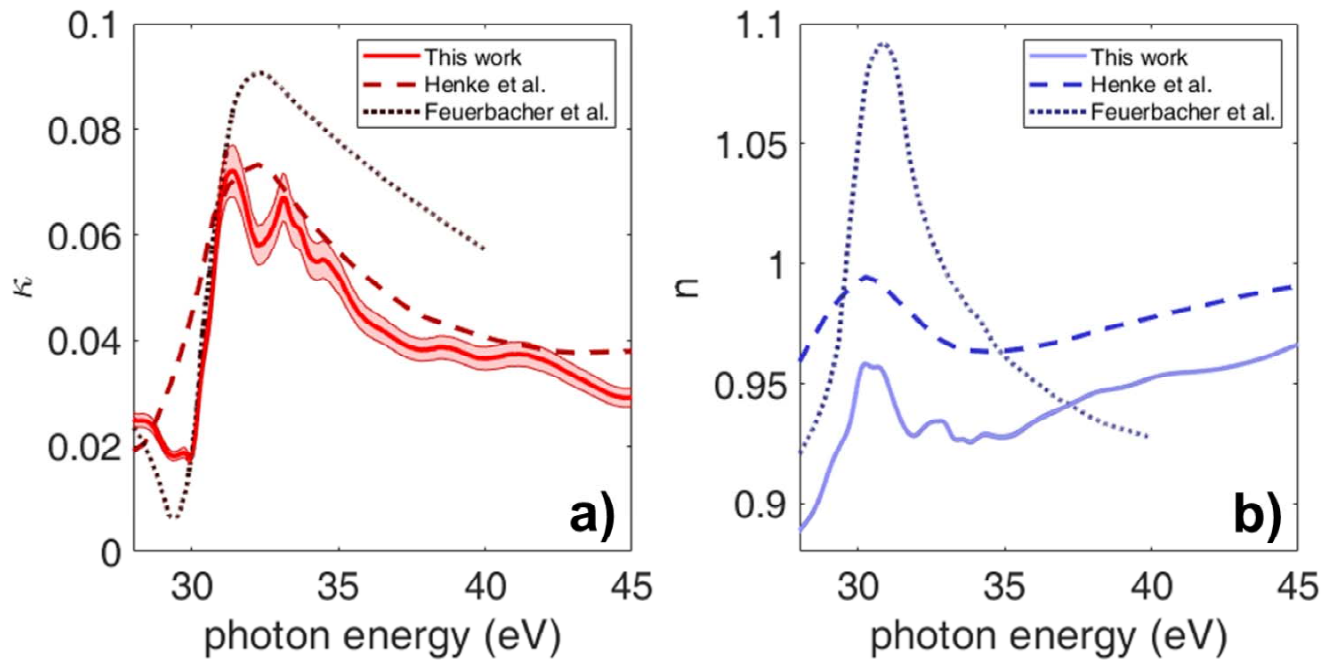
Figure 14 Retrieved complex refractive index. A) Retrieved κ (red, solid) compared to previous studies, along with error (red, shaded). B) retrieved n (blue, solid), compared to previous studies, along with error (blue, shaded).

The resulting refractive index recovered from the multi angle fit is shown in Figure 14, along with reference values obtained from previous studies [84,85] . Overall, the results obtained in this work agree quite well with those obtained by Henke et al. [85], ─and agree reasonably with

the results obtained by Feuerbacher et al. [84]. The recovered κ values show a sharp jump at 30 eV, which has been previously assigned, as noted, to the $M_{4,5}$ absorption edge. The subsequent drop in κ above 35 eV is consistent with core hole effects, which reduce the absorption cross section above the resonance due to scattering of the conduction band wave functions with the core-hole created by the XUV photons [92]. Additionally, there is a corresponding dispersive feature in n that is also present in previous work. The recovered n and κ values show the presence of multiple structures between 30 and 45 eV that have not been previously observed in the XUV refractive index. These are discussed in more detail in Sec. 2.3.3 Because κ and n ultimately both report on the same process, namely polarization of the material by the incident XUV light, κ and n are not independent. As a result, given knowledge of one quantity (n or κ), the other can in theory be found via the Kramers-Kronig relations [93]. Accordingly, comparison of the measured n or κ with the n or κ obtained by the Kramers-Kronig transform provides a useful check for self-consistency of our results. To evaluate the results for self-consistency, we applied the Kramers-Kronig transforms to the κ and n in Figure 2a, yielding κ_{KK} and n_{kk}, and computed the mean RMS error $E_\kappa = \sqrt{(\kappa - \kappa_{KK})^2}$, and $E_n = \sqrt{(n - n_{kk})^2}$, yielding E_κ=0.027 and $E_n = 0.021$. For comparison, the same values obtained from Kramers-Kronig analysis of Henke et al.'s work were $E_\kappa = 0.021$ and $E_n = 0.005$. Accordingly, our κ and n are reasonably consistent with the Kramers-Kronig relations, within expected error.

2.3.2 Analysis of Recovery

To analyze the accuracy with which n and κ can be determined from multi angle reflection data, we define the sensitivity function in the same manner as previous work [50,84]

$$S_f = (f/R_s)(\partial R_s/\partial f) \tag{2.2}$$

where R_s is the Fresnel reflectance (2.1) and f stands for n or κ. This function is the ratio of error
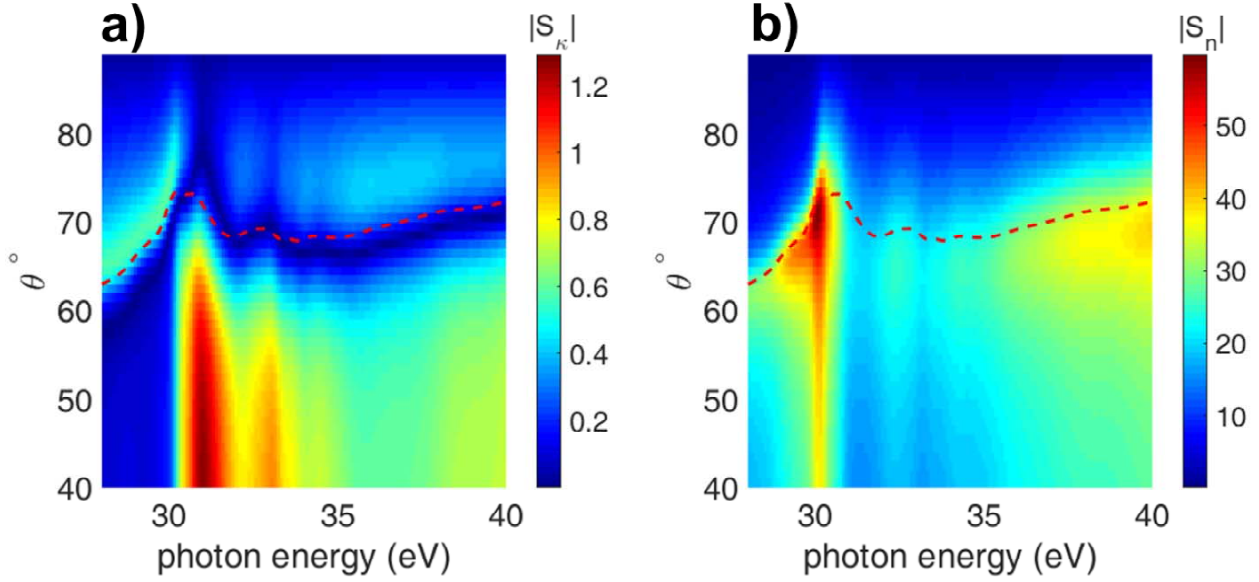
Figure 15 Sensitivity functions for S_k and S_n. Absolute values of the sensitivity functions S_k (A) and S_n (B) as a function of photon energy and angle of incidence. Estimated critical angle (ϑ_{crit} red dashed line) traces out region of low S_k and marks onset of large S_n.

in reflection to the error in the XUV optical constants, which thus provides an estimation of the sensitivity of the recovered refractive index to fluctuations in the input reflectivity. The corresponding sensitivity functions are shown in Figure 15. Because $\kappa \ll n$, we show the relative sensitivity (S_f) instead of absolute sensitivity, $(\partial R_s / \partial f)$, to highlight the relative sensitivity for these disparate quantities, however analysis of absolute and relative sensitivity show the same behavior.

      Overall, S_κ (Figure 15a) is at least an order of magnitude less than S_n (Figure 15b), indicating that the reflectivity measurements are much more sensitive to n than κ. This result explains the two-order of magnitude difference in the errors associated with the recovery of n and κ. Generally speaking $\lim_{\kappa \to 0} S_\kappa = 0$, therefore we attribute the relatively lower sensitivity of the reflectivity to κ as being due to the low κ value of germanium in this wavelength regime. Interestingly, S_κ shows a local minimum in sensitivity, which varies from 60-72° across the entire energy region surveyed. The local minimum is extremely close to the XUV critical angle of germanium, which is also 60-72° in this wavelength regime. Indeed, when $\vartheta_{crit} = \sqrt{2(1-n)}$ [94] is plotted along with S_κ and S_n (red line, Figure 15), it is apparent that for

$\theta_i = \vartheta_{crit}, S_\kappa \to 0$. This result can be easily explained by the fact that for $\theta_i = \vartheta_{crit}$, an evanescent wave forms, and the incident beam experiences total external reflection. As a result, the natural attenuation of the beam due to the complex phase shift associated with κ becomes less significant compared with the already present attenuation of the evanescent wave. Consequently, this work suggests that accurate determination of κ via multi angle reflection requires angles of incidence $\theta_i \neq \vartheta_{crit}$. In contrast, S_n shows no local minimum near ϑ_{crit}, and grows substantially with less grazing angles of incidence, thus requiring $\theta_i < \vartheta_{crit}$, indicating that accurate determination of n requires angles of incidence lower than ϑ_{crit}. This analysis reveals that grazing angle reflection may lead to poor determination of n and κ in the XUV, due to the possibility of total external reflection, and it indicates that, in this system, measurements near ϑ_{crit} are relatively insensitive to κ.

2.3.3 Analysis of Refractive Index

The structures observed in the recovered κ (Figure 14a), are highlighted in Figure 16a. Single peaks at 30.3 eV, 31.36 eV, 38.69 eV and 41.29 eV as well as doublet structures at 33.1/33.67 eV, and 34.45/35.12 eV are apparent. Of these structures, those at 31.36, 38.69 and 41.29 eV have not been observed previously.

As previously mentioned, the abrupt rise of κ at 30 eV is due to the onset of the $M_{4,5}$-edge from 3d-core states into unoccupied states in the conduction band. Because the 3d-core states have an essentially flat dispersion, near the $M_{4,5}$-edge, peaks in κ correspond to regions of the conduction band structure that have both flat dispersion (high joint density of states with respect to the core levels), and high p-character (as dictated by angular momentum selection rules for the XUV transition) [21,50].

Because the 3d-core states are spin-orbit split by 0.6 eV, peaks in κ should occur as doublets spaced by 0.6 eV. To analyze the peaks in κ for evidence of doublet structure, the 2nd derivative of κ with respect to energy is shown below in Figure 4b (black). The doublet spacing of 0.6 eV present in the 2nd derivative (black) reveals that the single peaks at 30.3 and 31.36 eV in κ are in fact doublets with this splitting. This suggests that the peaks at 30.3 and 31.36 eV in κ originate from transitions from the core states into single regions of the conduction band. The
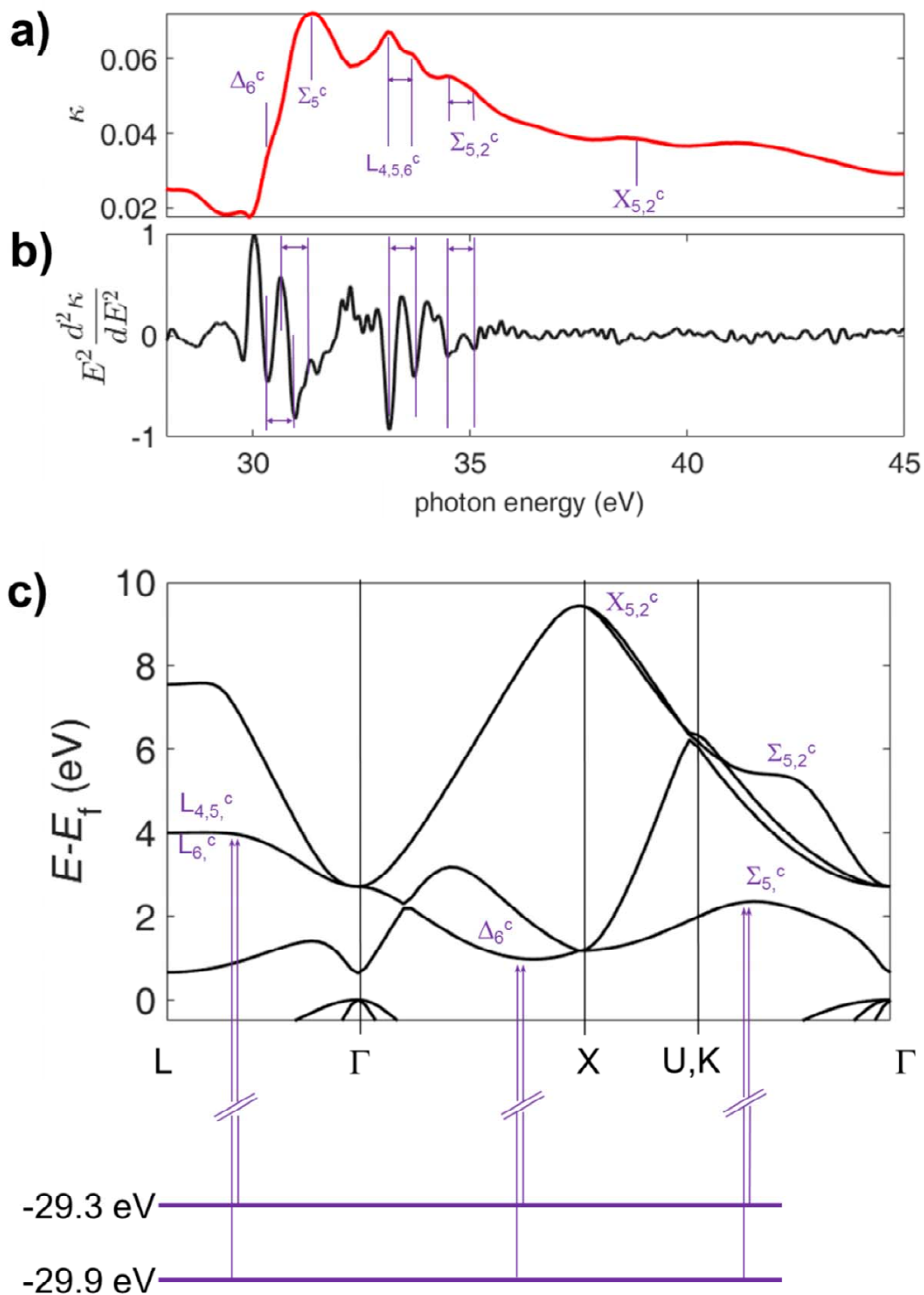
Figure 16 Recovered κ with assigned transitions in band structure. A) Recovered κ with specific transitions. B) 2nd energy derivative. Vertical bars spaced by 0.6 eV, corresponding to the 0.6 eV spin-orbit splitting of the 3d core levels. C) Band structure showing example transitions from 3d core levels.

peak at 38.69 eV, by contrast, shows no doublet structure within the noise, indicating that it may not originate from a single transition. The lack of a doublet structure in the peak at 38.69 eV could however by due to the weak nature of this transition.

In order to assign the features in Figure 16a, we use the energies of the peaks and consider angular momentum selection rules, along with the results a band structure adapted from [21], which are shown below in Figure 4c. The resulting assignments are summarized in

Table 1: Observed structures in κ and assignments

Peak Energy (eV)	Band Assignment	% p-character
30.30	Δ_6^c	46
31.36	Σ_5^c	45
33.10	$L_{4,5,6}^c$	76
33.67	$L_{4,5,6}^c$	76
34.45	Σ_5^c	71
35.12	$\Sigma_{5,2}^c$	71
38.69	$X_{5,2}^c$	93

Table 1. The peak at 30.3 eV is assigned to transitions into the mostly p-character Δ_6^c band, as the band structure calculations show this band to be 0.97 eV above the valence band maximum (VBM), which is known to be 29.3 eV above the $3d_{3/2}$ core level, yielding an expected energy of 30.27 eV for this transition. This assignment is similar to structures observed in near-normal incidence reflectance measurements in Ref. [86], but has not previously been observed in the complex refractive index. The peak at 31.36 eV is assigned to the mostly p-character Σ_5^c band, which has a flat region 2.1-2.3 eV above the VBM, giving an expected transition energy of 31.4-31.6 eV with respect to the $3d_{3/2}$ core level. This assignment stands in contrast with previous work on XUV reflectance [84], which was unable to resolve this transition and instead assigned it to a broadened transition at 32 eV. The doublet at 33.1/33.67 eV is assigned to transitions from the spin-orbit split core states into the $L_{4,5,6}^c$ bands, which have high p-character and should occur at 4 eV above the VBM, (at 33.3 eV with respect to the $3d_{3/2}$ core level). The doublet at 34.67 eV is tentatively assigned to the $\Sigma_{5,2}^c$ band, which occurs at 5.4 eV above the VBM (34.7 eV above the $3d_{3/2}$ core level). The peak at 38.69 eV is assigned to the high p-character $X_{5,2}^c$ band, which is 9.4 eV above the VBM, yielding an expected transition energy of 38.7 eV. Despite having a relatively large density of states, this peak is extremely weak in the recovered κ. The weak peak 41.29 eV roughly matches in energy with higher lying X bands, which have appreciable p-character density of states between 11.58-12.6 eV above the VBM, corresponding

to an expected transition energy of 40.88-41.89 eV, however due to the weak nature of the peak and the imperfect match with any specific band, this transition cannot be unambiguously assigned.

2.4   Conclusion

The high resolution complex-valued refractive index recovered in this work allows determination and assignment of many structures, which have not previously been observed in the refractive index. Further, this work reveals several new structures that have not been observed by any method, and these are assigned to the $\Sigma_{5,C}$ and the $X_{5,2,C}$ bands. Finally, our analysis indicates that multi angle reflection is much more sensitive to n than κ. This issue is in part attributed to total external reflection at the critical angle. Observation and assignment of these features will pave the way for analysis of time-resolved XUV studies in germanium. This work constitutes a substantial improvement on the previously available refractive index of germanium in the XUV, and it paves the way for future XUV studies of dynamics by transient reflectivity in germanium.

Chapter 3: Femtosecond XUV transient reflectivity of Germanium

Some content and figures of this chapter are reprinted or adapted with permission from Christopher J. Kaplan, Peter M. Kraus, Andrew D. Ross, Michael Zürch, Scott K. Cushing, Marieke F. Jager, Hung-Tzu Chang and Eric M. Gullikson.

"Femtosecond tracking of carrier relaxation in germanium with extreme ultraviolet transient reflectivity," Phys. Rev. B 97, 1–9 (2018)

Extreme ultraviolet (XUV) transient reflectivity around the germanium M4,5 edge (3d core-level to valence transition) at 30 eV is advanced to obtain the transient dielectric function of crystalline germanium [100] on femtosecond to picosecond time scales following photoexcitation by broadband visible-to-infrared (VIS/NIR) pulses. By fitting the transient dielectric function, carrier-phonon induced relaxations are extracted for the excited carrier distribution. The measurements reveal a hot electron relaxation rate of 3.2 ± 0.2 ps attributed to the X-L intervalley scattering and a hot hole relaxation rate of 600 ± 300 fs ascribed to intravalley scattering within the heavy hole (HH) band, both in good agreement with previous work. An overall energy shift of the XUV dielectric function is assigned to a thermally induced band gap shrinkage by formation of acoustic phonons, which is observed to be on a timescale of 4–5 ps, in agreement with previously measured optical phonon lifetimes. The results reveal that the transient reflectivity signal at an angle of 66° with respect to the surface normal is dominated by changes to the real part of the dielectric function, due to the near critical angle of incidence of the experiment (66°–70°) for the range of XUV energies used. This work provides a methodology for interpreting XUV transient reflectivity near core-level transitions, and it demonstrates the power of the XUV spectral region for measuring ultrafast excitation dynamics in solids.

3.1 Introduction

Understanding the electronic response of solids to ultrashort laser pulses is crucial for developing efficient optoelectronics, [95] hot carrier solar utilization, [96] and other semiconductor based devices. Recently, extreme ultraviolet (XUV) transient absorption was shown to be capable of simultaneously recording separate electron and hole dynamics in nanocrystalline germanium thin films in a single measurement. [21,97] This work confirmed intervalley scattering rates and revealed the time-scales of carrier-recombination at defect-rich grain boundaries of nanocrystals through a Shockley-Read-Hall mechanism. These results highlight the ability of XUV transient absorption to provide a spectrally resolved probe of complex dynamics in solids. [11,15,98] However, electron and hole relaxation kinetics measured in these films were ultimately limited by the high defect density in the thin film samples, and the results were not characteristic of the intrinsic, high purity, material itself. This discrepancy highlights drawbacks of XUV transient absorption in solids, namely that it can only be applied to very thin films (<100 nm). These thin films are difficult to obtain and can be of questionable relevance to representative semiconductors, due to their low thermal conductivity and defect rich structure. Developing a tool to provide a spectrally resolved, sub-femtosecond probe of carrier dynamics in well-defined, single crystal samples remains a significant challenge in unraveling ultrafast processes in solids.

In contrast to absorption, XUV reflectivity allows spectroscopic access to dynamics in optically thick, well-defined samples, greatly extending the set of systems in which XUV spectroscopy can be applied. [99–103] Static XUV reflection spectra from high harmonic sources have been demonstrated and shown to provide excellent surface sensitivity. [49,104] Quite recently, XUV transient reflectivity (XUV TR) was used for time-resolved spectroscopic observation of surface electron dynamics in metal oxides. [51] This work highlighted the sensitivity of reflectivity to the full dielectric function $\epsilon(\omega) = \epsilon_1(\omega) + i\epsilon_2(\omega)$, including both the dispersive part $\epsilon_1(\omega)$, and the absorptive part $i\epsilon_2(\omega)$. Despite these advances, questions such as the relative sensitivity of XUV TR to electronic or lattice dynamics, and the role of the real vs imaginary parts of the dielectric function have yet to be explored. These questions are made

more difficult by the fact that few XUV TR experiments to date have been performed on single crystal samples. Accordingly, comparison of XUV TR to the wide body of optical transient reflectivity in single crystal semiconductors is difficult.

To surmount these challenges, here we develop XUV transient reflectivity to measure the time-resolved XUV dielectric function of single crystal germanium, a widely employed group IV semiconductor. By monitoring reflectivity around the Ge $M_{4,5}$ absorption edge subsequent to excitation with a few-cycle 800 nm pump pulse, the XUV core-level transitions provide a spectrally resolved, ultrafast probe of carrier dynamics in the valence and conduction bands. The time-resolved XUV dielectric function is retrieved from the data, allowing spectral separation of electrons, holes, and band shift contributions to the observed transient reflectivity. Analysis of the recovered transient dielectric function reveals that the XUV TR signal contains information from both the real and imaginary parts of the dielectric function and that the real part is more significant at the reflection angle chosen. Further, kinetic analysis of the retrieved dielectric function allows extraction of electron, hole and lattice relaxation timescales. The measurements reveal a hot electron relaxation rate of 3.2±0.2 ps attributed to the X–L intervalley scattering and a hot hole relaxation rate of 600±300 fs ascribed to intravalley scattering within the heavy hole (HH) band, both in good agreement with previous work. An overall energy shift of the XUV dielectric function is assigned to band gap renormalization due to the formation of acoustic phonons, which is observed to be on a timescale of 4±1 ps, in agreement with previously measured optical phonon lifetimes.

3.2 Methods

3.2.1 Transient Reflectivity

The apparatus (Figure 17) consists of an 800 nm Ti:sapphire laser, which is used to generate high harmonics (HHG) [105], a toroidal focusing mirror, a Ge(100) sample, a variable time delay line, a variable line spaced grating, and an X-ray CCD camera to detect the reflected signal from the sample.

In the experiment, a NIR (near infrared) 5-fs pulse, spanning a bandwidth from 550-1000 nm, is focused collinearly with a time-delayed subfemtosecond XUV pulse created by high harmonic generation (HHG) [105] onto a single crystal germanium [100] wafer (Figure 17) at an angle of 66° from the normal. This angle was constrained by the geometric configuration of the apparatus, but the value is fortuitous because it is near the critical angle in the XUV wavelength range of interest, which will be discussed further below. While the apparatus has the capability to measure subfemtosecond processes, the results here focus on the many-femtosecond to picosecond timescales to perform an analysis of the transient reflectivity dielectric function and carrier-phonon processes in germanium. The NIR pulse photoexcites carriers across the direct band gap of germanium (0.8 eV, indirect gap 0.66 eV), yielding a carrier density of ~ 3 x 10^{20} cm^{-3} (Figure 17), which corresponds to an excitation of 0.6% of the germanium atoms. The resulting excited carrier distribution is then probed via transitions from Ge 3d (J=5/2 and 3/2, spin-orbit splitting 0.57 eV) core states to unoccupied states in the valence and conduction bands [106] by measuring the transient reflectivity defined as $\Delta R/R = \left[R_p(E,\tau) - R_0(E)\right]/R_0(E)$, where $R_0(E)$ and $R_p(E,\tau)$ are the intensity of reflected signal from the static (unpumped, 0), and excited sample (pumped, p), respectively. The Ti:sapphire amplifier produces 1.7 mJ, 25 fs pulses at a 1 kHz repetition rate. The pulses are then compressed to sub 5-fs duration (corresponding to less than 2 optical cycles) and 800 µJ pulse energy using self-phase modulation in a neon-filled hollow core fiber and chirped mirror compressor (Ultrafast Innovations optics). Few-cycle compression is a prerequisite for generation of an XUV continuum, which greatly enhances signal to noise over the required large XUV bandwidth in the experiment. The usable compressed pulse bandwidth extends from 550-1000 nm, and the pulses are characterized using a dispersion scan [107] showing a pulse duration of <5 fs. The compressed output is split with a 60:40 beam splitter. Sixty percent of the energy (480 µJ) is used to generate the probe via HHG. High harmonics are produced by focusing into a Xe gas target, yielding continuous harmonic spectra from 25-40 eV. Residual NIR from the generation process is removed with a 100 nm thick Al filter. The XUV probe is then focused onto the sample using a grazing incidence gold-coated toroidal mirror. The remaining 40% pump of the energy is time delayed using a retroreflector on a piezostage and recombined collinearly with the probe using an annular mirror.
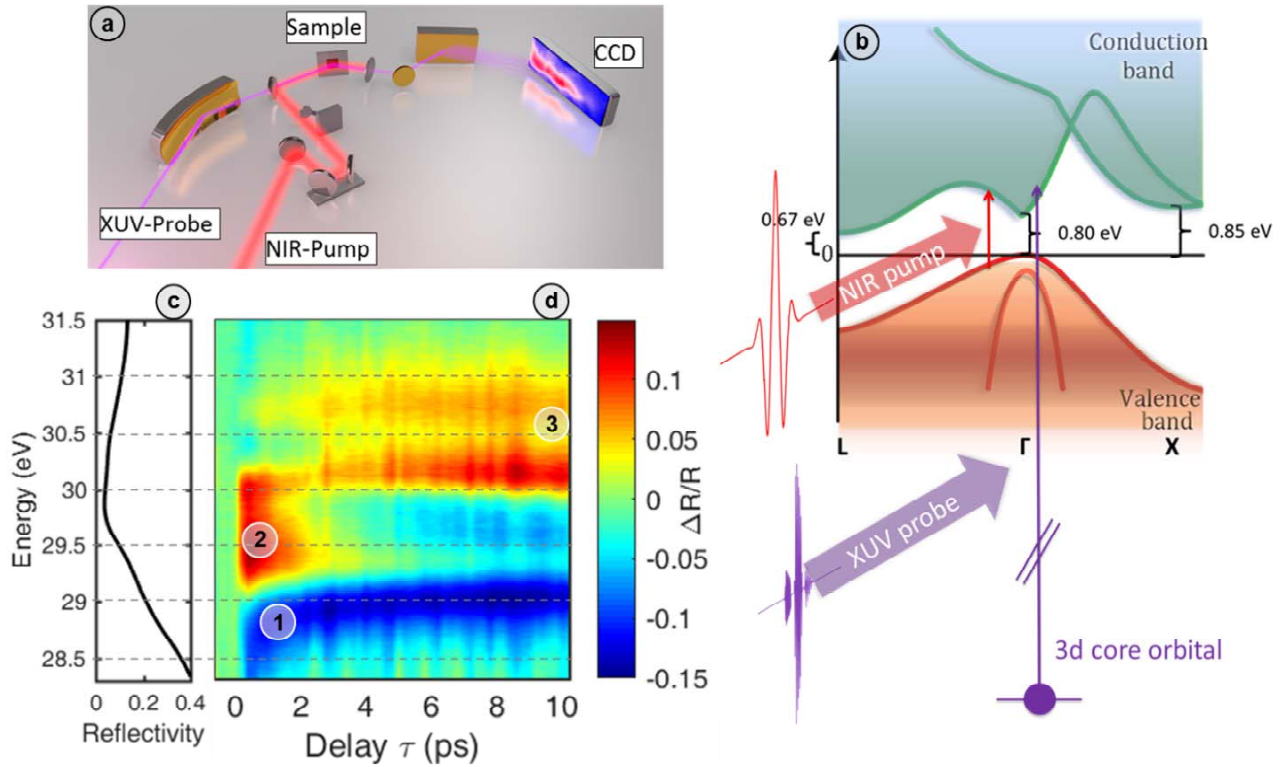
Figure 17: Femtosecond Transient Reflectivity in germanium. (a) A time delayed XUV pulse probes transient reflectivity in single crystal germanium, after excitation with a few cycle NIR pump pulse. (b). The NIR pump promotes electrons from the valence band (red) to the conduction band (green). Subsequently, reflectivity of the XUV probes the excited carrier distribution via transitions from 3d core states to the valence and conduction bands at the $M_{4,5}$ edge. (c) Static reflectivity of germanium at 66° angle of incidence, s-polarization. (d). Raw transient reflectivity data measured, with marked reflectivity features 1, 2 and 3 as described in text.

The NIR pump pulse is focused to 200 μm (FWHM) diameter onto the sample, and the XUV beam is focused to ~100 μm (FWHM) diameter. Single crystal germanium [100] wafers, undoped, were obtained from commercial sources. Any ambient oxide is not removed. The static (unpumped) dielectric function of the sample was measured by fitting reflectivity measured at 6 angles with synchrotron radiation, s-polarized, to the Fresnel equations [45], as described in the previous chapter.

3.2.2 Kinetic Modeling

To model the kinetics of the time-resolved dielectric function (discussed later), the carrier dynamics were compared to a 3 temperature model (3TM) adapted from previous work [108,109] which includes the effects of carrier diffusion, Auger recombination, and the spatial dependence of the carrier distribution.

$$\frac{\partial n_e}{\partial t} = \frac{\partial}{\partial x}\left(D_a \frac{\partial n_e}{\partial x}\right) - \frac{n_e}{\tau_{Aug}(n_e)} + S(x,t) \tag{3.1}$$

$$D_a = D_0 T_a^{-1}\sqrt{T_e} \tag{3.2}$$

$$C_e \frac{\partial T_e}{\partial t} = \frac{D_a C_e}{n_e}\frac{\partial n_e}{\partial x}\frac{\partial T_e}{\partial x} - \frac{C_e}{\tau_{eo}}(T_e - T_o) - \frac{C_e}{\tau_{ea}}(T_e - T_a) + E_g \frac{n_e}{\tau_{Aug}(n_e)} + \left(\hbar\omega - E_g\right)\cdot S(x,t) \tag{3.3}$$

$$C_o \frac{\partial T_o}{\partial t} = \frac{C_e}{\tau_{eo}}(T_e - T_o) - \frac{C_o}{\tau_{oa}}(T_o - T_a) \tag{3.4}$$

$$C_a \frac{\partial T_a}{\partial t} = \frac{\partial}{\partial x}\left(C_a D_a \frac{\partial T_e}{\partial x}\right) + \frac{C_e}{\tau_{ea}}(T_e - T_a) + \frac{C_o}{\tau_{oa}}(T_o - T_a) \tag{3.5}$$

In equations 3.1-3.2, n_e is the excited carrier density, D_a is the temperature dependent ambipolar electronic diffusion coefficient of germanium [110], D_0 is the ambipolar electronic diffusion coefficient at room temperature, [25] T_a and T_o are the temperatures of the acoustic and optical phonon baths, T_e is the excited carrier temperature, τ_{Aug} is the auger recombination rate, [111] and $S(x,t)$ is a source term, (a hyperbolic secant squared pulse with 5 fs full width at half max, with 800 nm wavelength). In equations 3.3-3.5, C_e, C_o, and C_a refer to the heat capacities of the electronic, optical phonon, and acoustic phonon baths respectively, τ_{eo}, τ_{ea}, and τ_{oa} refer to the electron-phonon, and phonon-phonon coupling times. Additionally, C_a is the thermal diffusion coefficient of germanium. The heat capacity of the acoustic phonons is modeled using an Debye model with a Debye temperature of 374 K. [112]

The resulting carrier density profile obtained from the model is shown in Figure 19. The carrier density shows dynamics expected for an inhomogeneously excited sample. Initially, the carrier density profile shows an exponential decay as a function of depth, due to attenuation of the pump in the material. Rapidly, diffusion causes a reduction in the steepness of the depth profile, and
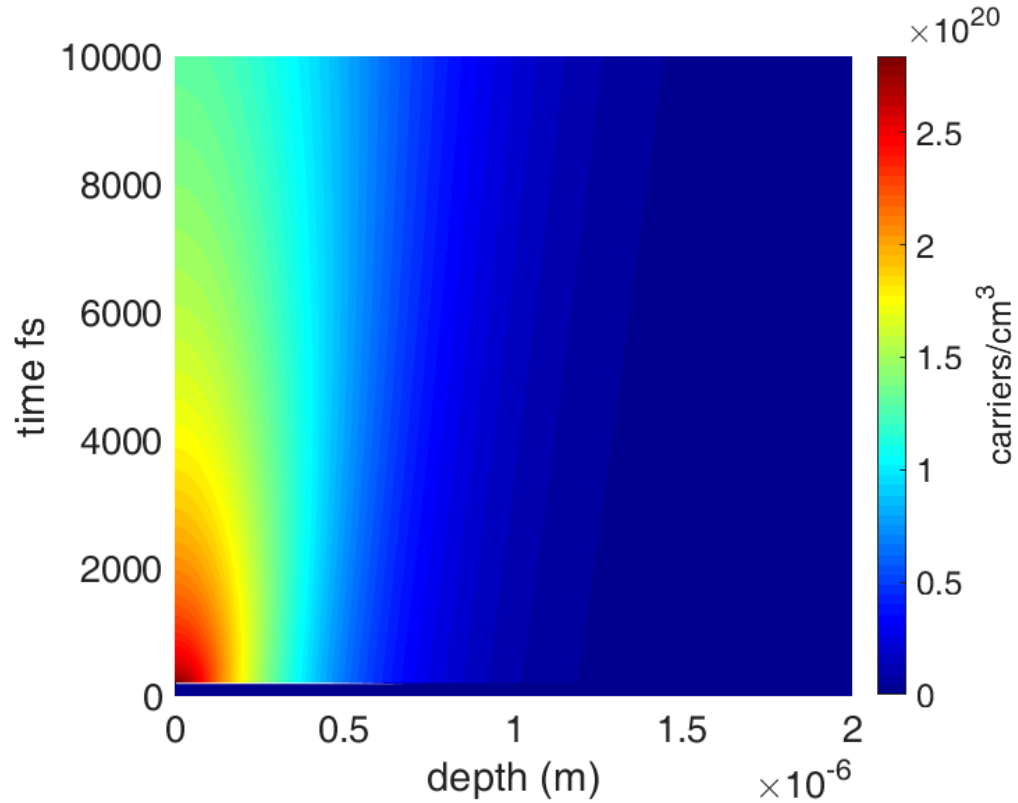
Figure 19: Simulated time dependent carrier density profile within sample, obtained from model described in section 3.2.2. Surface carrier density shows rapid decay in time due to auger recombination, and diffusion of the excited carrier distribution into the bulk.
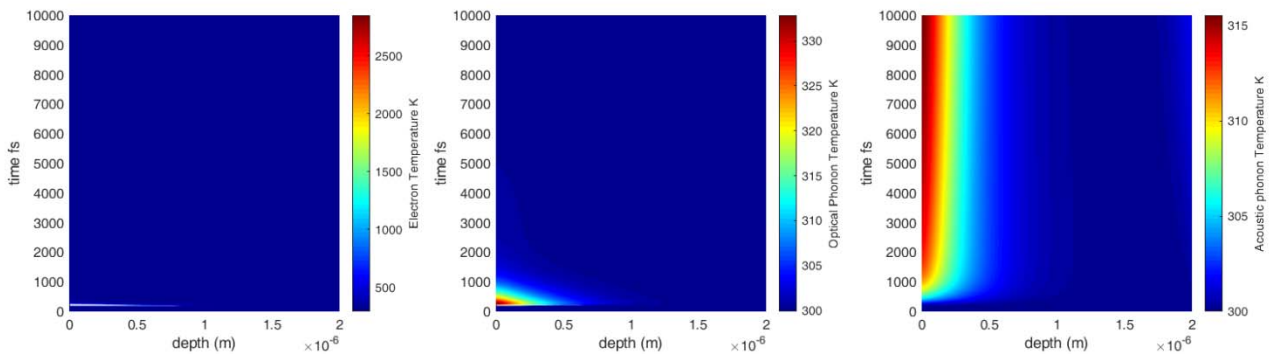
Figure 18: Simulated temperature dynamics obtained from model. (Left), electron temperature, (middle) optical phonon temperature, (right) acoustic phonon temperature.

auger recombination causes further depletion at the highest density regions (the surface).

The resulting carrier, optical phonon, and acoustic phonon temperatures are shown in Figure 18. The 3 temperature system shows well documented behavior in which the pump laser rapidly excites the carrier bath, which then cools by scattering with optical phonons via deformation potential scattering on a sub picosecond timescale [113–115], which then subsequently transfer energy to the acoustic phonon bath on a multi picosecond timescale.

3.3 Results and Discussion

3.3.1 Transient Reflectivity

The static reflectivity spectrum shown in Figure 17c, is characterized by a sharp decrease and subsequent increase of the reflectivity around the Ge $M_{4,5}$ edge (29.2, 29.8 eV), corresponding to transitions from the $3d_{5/2,3/2}$ core states into unoccupied states in the valence and conduction bands. The onset of the reflectivity increase around 30 eV mimics the evolution of the imaginary part of the refractive index, i.e. the absorbance of the material.

The transient XUV reflectivity changes, $\Delta R/R$ as a function of pump-probe delay and reflected photon energy are shown in Figure 17d. The transient features observed can be broadly classified as follows: a decrease in reflectivity from 28-29 eV that persists for at least 10 ps (feature 1), an increase in reflectivity from 29-30 eV (feature 2) that decays within 3 ps, and a pair of features at 30.1 eV, and 30.7 (feature 3) that gradually grow in on a many-picosecond timescale.

Ultimately, the transient features in Figure 17d need to be linked to the pump-induced creation of holes in the valence band (below 29.2-29.8 eV), electrons in the conduction band (above 29.8-30.4 eV), and the subsequent relaxation processes [21]. Both features 1 and 2 lie below the formal onset of the conduction band (29.8 eV), requiring a detailed analysis (discussed below) to make this link and to spectroscopically assign features 1, 2 and 3. The analysis also considers the 3d spin-orbit splitting of the major features due to electrons and holes.

3.3.2 Decomposition of transient reflectivity into carriers and energy shift

The recorded transient reflectivity (Figure 17a) results from changes in the real and imaginary parts of the dielectric function of germanium due to state-blocking by excitation of both electrons and holes and energy level shifts due to changes in core-hole screening and phonon dynamics. In order to disentangle and recover these separate effects from the XUV transient reflectivity data, we start with the premise that the changes to the dielectric function can be fit by sum of a few complex oscillator terms. Thus, a fit of the transient reflectivity data is made via equation 3,6 to an excited state transient dielectric function, ϵ_{exc}, of the following form:

$$\epsilon_{exc}(\omega) = \epsilon_{shift}(\omega) + \epsilon_{carrier}(\omega)$$
$$= \epsilon_{shift}(\omega) + \epsilon_{holes}(\omega) + \epsilon_{electrons}(\omega)$$
$$\epsilon_{exc}(\omega) = \epsilon_0\big(\omega - E_{shift}\big) + \frac{\omega_{p,h}^2}{\omega_{0,h}^2 - \omega^2 - i\omega\Gamma_h} - \frac{\omega_{p,e}^2}{\omega_{0,e}^2 - \omega^2 - i\omega\Gamma_e} \qquad \textbf{(3.6)}$$

where $\epsilon_{shift}(\omega)$ and $\epsilon_{carrier}(\omega)$ represent contributions to the dielectric function from global shifts and the carriers (electrons + holes) respectively. In equation (3.6), ϵ_0 is the ground state dielectric function (measured by multi angle reflection), and $\epsilon_0\big(\omega - E_{shift}\big)$ describes the impact of global shifts to the excited state dielectric function, which physically correspond to energy shifts of the core-level or the unoccupied conduction band states. The two Lorentzian terms are Lorentz-Drude oscillators, one for the electron and one for the hole contributions to the excited state dielectric function. The Lorentz-Drude model is frequently used to model the dielectric function in the optical, UV, or XUV frequency ranges [113,116].

The two oscillators are described by the parameters $\omega_{p,h}, \omega_{p,e}, \omega_{0,h}, \omega_{0,e}, \Gamma_h,$ and Γ_e, which include the amplitude, central frequency, and width of excited electron and hole induced changes to the dielectric function. At each time-delay point the broadband transient reflectivity signal is fit to equation (3.6), giving a parameterization of the excited state dielectric function in

terms of electron, hole, and global shift contributions, and allowing separation of the transient contribution from each term.

Previous work accounted for the spin-orbit splitting of the core-hole by deconvolving the dynamics under the assumption that the $3d_{5/2}$ and $3d_{3/2}$ core states give rise to a statistical distribution of transient features, with ratios 3:2 [21,77]. In the presented model, this would be accounted for by splitting each oscillator into two components, spaced by the spin-orbit splitting (0.57 eV), with a set amplitude ratio of 3:2. Fitting using this model is unable to match the
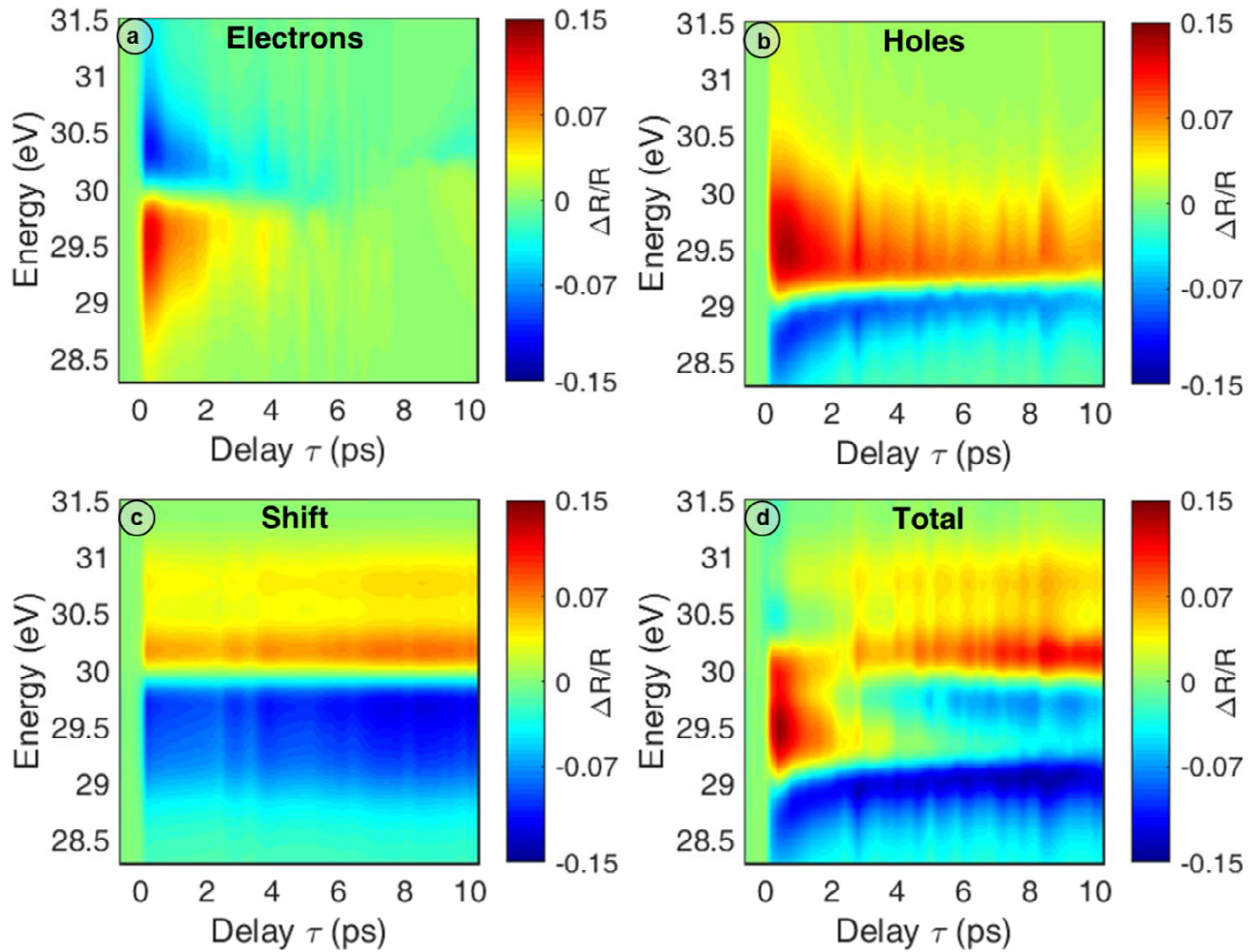
Figure 20: Transient Reflectivity Modeling and Decomposition. (a) Electron contribution to $\Delta R/R$ computed from dielectric function fit in equation 3.1. (b) Hole contribution to $\Delta R/R$ computed from dielectric function fit. (c) Shift contribution to $\Delta R/R$ computed from dielectric function fit. (d) Total recovered $\Delta R/R$ computed from dielectric function fit.

experimental data. This could be due to the broad nature and complex shape of the $M_{4,5}$ transition, especially in the dispersive part of the dielectric, [106] and it will be shown below that the real part of the dielectric function dominates the reflected signal at the specific angle used here. There could also be a non-statistical branching ratio from the two spin-orbit core-level states [117–119]. Both of these could result in the $M_{4,5}$ being experimentally better fit by single, broadened transitions, one each for electrons and holes. Consequently, we use only two oscillators, one for the electrons, and one for the holes, to model changes to the dielectric function near the $M_{4,5}$ edge. As shown below, this simple model provides a very good description of the observed dynamics, further justifying the simplifying assumption of a single oscillator each for electrons and holes.

The extracted reflectivity contributions for the holes, electrons and shifts (Figure 20a-c) allow assignment of the features in the experimental data. The total recovered transient reflectivity (Figure 20d) closely tracks the experimental data (Figure 17d) indicating that the model captures the dynamics present. The transient reflectivity contributions of both holes and electrons show a dispersive line profile at each time delay. This dispersion line has opposite signs for electrons and holes, and it changes sign at the center energy of the carriers, resulting from the fact that the electrons and holes have opposite effects on available states for XUV transitions. Holes contribute a depletion from 28.3 to 29 eV and an increase from 29 to 31 eV, which narrows, but persists for the entire 10 ps duration of the measurement (Figure 20a). Electrons contribute an increase from 28.3 to 30 eV and a depletion from 30 to 31.5 eV, which decays within approximately 4 ps (Figure 20b). The global shift contributes a depletion below 29.9 eV and an increase above 29.9 eV, which gradually increases on a longer timescale.

Interestingly, both the electron and hole $\Delta R/R$ contributions in Figure 20a,b show broadband changes spanning from a 3.2 eV range from 28.3 to 31.5 eV, including changes within the band gap region ~29-30 eV. This is because $\Delta R/R$ is sensitive to both ϵ_1 in addition to ϵ_2. Previous work has observed changes to the dispersive ϵ_1 in the gap region of semiconductors following interband excitation. [120] Accordingly, we attribute $\Delta R/R$ in the gap region to pump-induced changes in ϵ_1.

3.3.3 Assignment of the time resolved dielectric function

The transient dielectric function, $\Delta\epsilon(\omega) = \epsilon_{exc}(\omega) - \epsilon_0(\omega)$ was recovered from the fit of the experimental data to equation 3.6 and is shown in Figure 21a and Figure 21b. The real part, $\Delta\epsilon_1$ shows a transient depletion from 29-30 eV right at the M$_{4,5}$ edge, persisting for 4 ps, and an increase below 29 eV, which persists out to 10 ps. The imaginary part, $\Delta\epsilon_2$ shows a persistent increase from 28.5 to 29.3 eV (just below the M$_{4,5}$ edge), and a transient depletion from 29.9 to 31 eV (just above the M$_{4,5}$ edge), which is replaced by an increase growing in within around 4 ps. Both $\Delta\epsilon_1$ and $\Delta\epsilon_2$ shift toward the M$_{4,5}$ edge (29.6 eV) on a multipicosecond timescale.

To aid in assignment of the features in the transient dielectric function, the carrier contributions to the transient dielectric function ($\Delta\epsilon_{carrier} = \Delta\epsilon_{electrons} + \Delta\epsilon_{holes}$) are shown in Figure 21c,d. Comparing the carrier contributions to the total contributions reveals that most of the features of $\Delta\epsilon_{1,total}$ and $\Delta\epsilon_{2,total}$ near the M$_{4,5}$ edge come from the carrier contributions to the transient dielectric function. Indeed, the depletion in $\Delta\epsilon_{1,total}$ below 29 eV and transient increase from 29-30 eV are well captured by the carrier contribution, $\Delta\epsilon_{1,carrier}$. Similarly, the increase below 29.6 eV and depletion above 29.8 eV present in $\Delta\epsilon_{2,total}$ is almost entirely captured by features in the carrier contribution, $\Delta\epsilon_{2,carrier}$.

Near the Ge M$_{4,5}$ edge, the XUV dielectric function is dominated by direct, interband transitions from the 3d core-levels, to unoccupied states in the valence and conduction bands. [86,121] Accordingly the imaginary part of the linear dielectric function can be written as [122],

$$\epsilon_2(\omega) = 8 \left(\frac{\pi}{m\omega}\right)^2 \sum_f |P_{fi}|^2 J_{fi}(\omega) \tag{3.7}$$
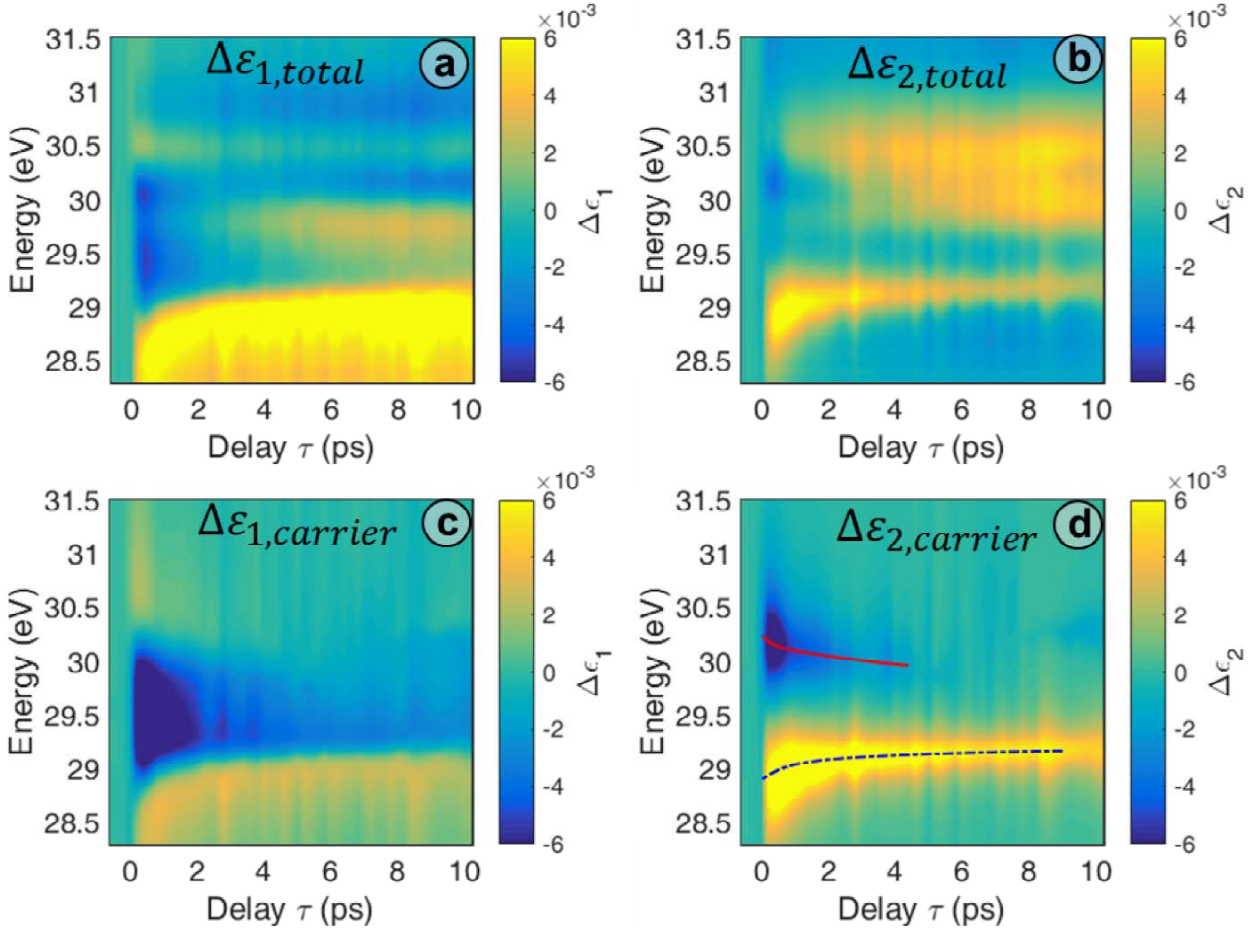
Figure 21 Recovered Time resolved dielectric function: (a) Transient dispersive $\Delta\epsilon_1$ retrieved from model. (b) Transient absorptive $\Delta\epsilon_2$ retrieved from model. (c) Carrier contribution to $\Delta\epsilon_1$ retrieved from model. (d) Carrier contribution to $\Delta\epsilon_2$ retrieved from model, showing carrier center energies of electrons (red line), and holes (blue line), respectively.

where e is the electron charge, m is the electron mass, P_{fi}, is the transition dipole matrix element between the initial and final states, J_{fi} is the joint density of states, f runs over all unoccupied states, and i refers to the 3d core states. Inspecting equation 3.7 reveals that carriers created by the pump can modify the XUV dielectric function either through state blocking (represented as a change in the joint density of states) or though renormalization of the 3d core hole potential manifesting as a change in the transition matrix element and the joint density of states). Consequently, the amplitude $\Delta\epsilon_2$ can be directly related to modifications of the density of states (i.e. state blocking by an excited carrier distribution), weighted by the transition dipole moment.

Because $\Delta\epsilon_2$ is directly related to the change in XUV absorption of the material [123], we can interpret the transient features in $\Delta\epsilon_{2,carrier}$ near the band edge as arising from state blocking of the $M_{4,5}$ transition by photoexcited carriers. The NIR pump promotes electrons from the valence band (VB) to the conduction band (CB), creating holes in the VB. The electrons in the CB reduce the available density of states for transitions from the 3d core-levels, resulting in the transient depletion of $\Delta\epsilon_2$ from 30-31 eV (Figure 21d). Similarly, holes in the VB increase the available density of states for core-level transitions, resulting in a positive $\Delta\epsilon_2$ below the band edge. The assignment of $\Delta\epsilon_2$ features to state blocking is supported by recent XUV transient absorption in germanium in which similar state blocking contributions were observed near the $M_{4,5}$ edge. [21]

3.3.4 Enhanced sensitivity to ϵ_1

To better understand the relationship between the measured transient reflectivity in Figure 20d and the recovered transient dielectric function, we computed the transient reflectivity contributions from the measured real and imaginary parts of the transient dielectric function (Figure 22a,b). For example, the imaginary contribution (Figure 22a) was computed as follows:

$$\frac{\Delta R}{R}(\Delta\epsilon_2) = \frac{\Delta R}{R}\big(Re(\epsilon_0) + iIm(\epsilon_{exc})\big)$$

(**3.8**)

where ε_0 and ε_{exc} are the (static) ground and excited state dielectric functions from equation 3.6. Despite the fact that dispersive $\Delta\epsilon_1$ and absorptive $\Delta\epsilon_2$ are both of similar magnitudes, the majority (74 ± 10 %) of the $\Delta R/R$ signal observed over the range of 28.3-31.5 eV can be attributed to the $\Delta\epsilon_1$ (real) contribution (Figure 22a). The $\Delta\epsilon_2$ (imaginary) contribution (Figure 22b) by contrast is smaller, contributing only 26 ± 10 % of the reflectivity changes from 28.3-31.5 eV. The insensitivity of the measured transient reflectivity signal to $\Delta\epsilon_2$ near the $M_{4,5}$ edge can be explained by examining $dR/d\epsilon_1$ and $dR/d\epsilon_2$, which are shown in Figure 22c. For small $\Delta\epsilon$ the magnitude of the computed derivatives in Fig. 4c provides an estimate of the sensitivity of the transient reflectivity to the real and imaginary parts of the dielectric function. Over the range of 28.3 to 31.5 eV, $dR/d\epsilon_1$ contributes 72% of the total derivative, indicating that relative sensitivity of $\Delta R/R$ to $\Delta\epsilon_1$ can be mainly explained by the static ground state dielectric function.

Interestingly, due to the zero crossing at 29.8 eV, from 29.7 to 29.9 eV $\Delta\epsilon_2$ contributes less than 5% to the total derivative, indicating a substantial lack of sensitivity to $\Delta\epsilon_2$ in this region.

More intuitively, the lack of sensitivity to $\Delta\epsilon_2$ at 29.8 eV can explained by the fact that at this energy, the angle of incidence is near the critical angle for germanium. This is illustrated in Figure 22d, which shows $dR/d\epsilon_2$, computed as a function of the angle of incidence (heat map), overlaid with the critical angle (red line), computed as $\sqrt{2(1-n)}$, where n is the real part of the ground state refractive index (recovered from the multi angle fit described in the SI). Interestingly, the critical angle closely tracks the zero of $dR/d\epsilon_2$, indicating that $dR/d\epsilon_2$ can be selectively tuned to greater or lower values by changing the angle of incidence nearer or further from the critical angle. Consequently, near-critical-angle transient reflectivity allows for selective sensitivity to ϵ_1 in many systems. In light of recent work demonstrating that the real part of the index of refraction shows enhanced surface sensitivity [51], the prospect of selective probing through the dispersive ϵ_1 provides a promising approach to achieve enhanced surface sensitivity with XUV transient reflectivity.
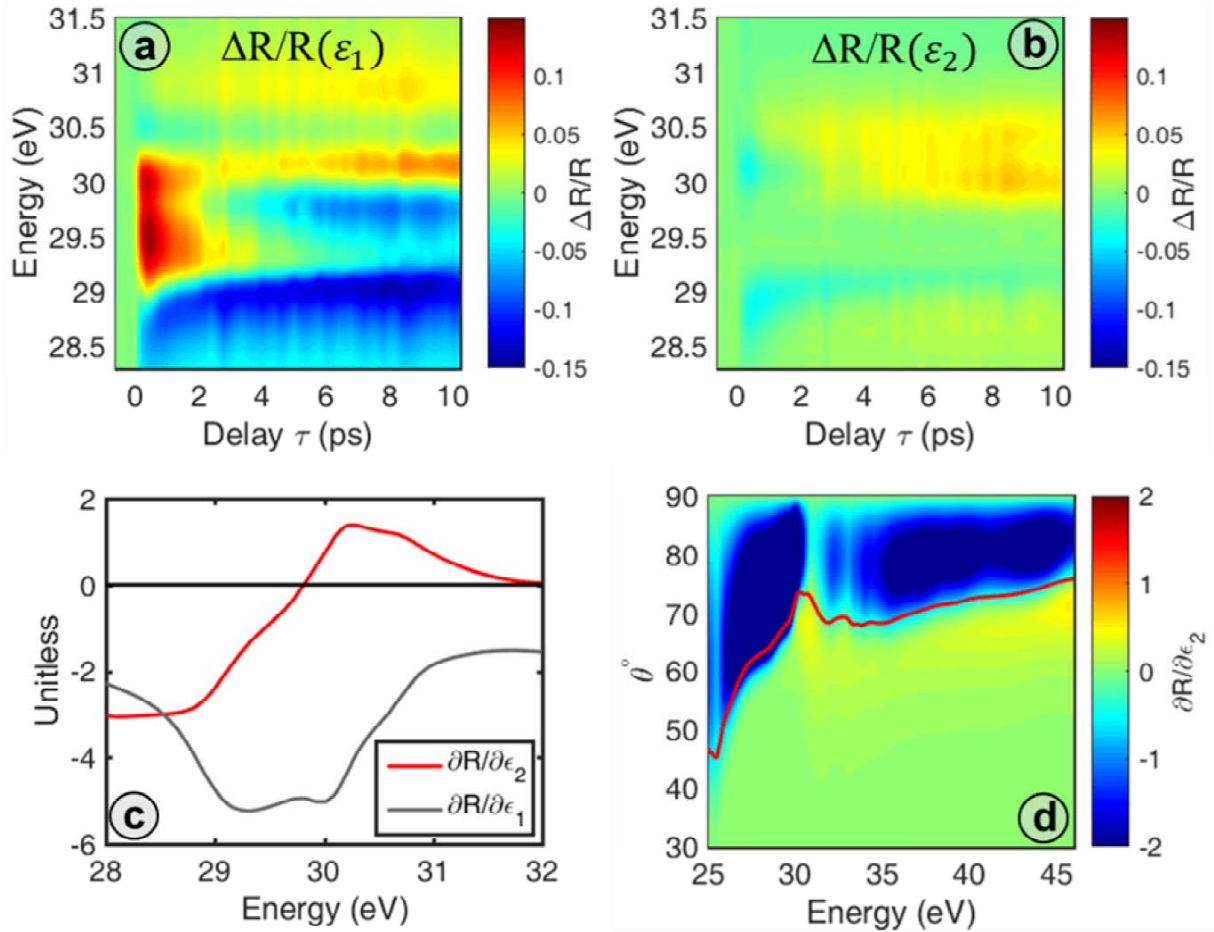
Figure 22 Sensitivity of Transient Reflectivity to ϵ_1: (a) $\Delta R/R$ computed with static ϵ_1 and transient ϵ_2 retrieved with model. (b) $\Delta R/R$ computed with static ϵ_1 and transient ϵ_2. (c) Red, $dR/d\epsilon_2$ at experimental angle of incidence (66), computed from static dielectric function, showing zero at 29.8 eV. Grey, $dR/d\epsilon_1$ at experimental angle of incidence (66), computed from static dielectric function, showing no zero. (d). Heatmap: $dR/d\epsilon_2$ as a function of angle of angle of incidence, computed from static dielectric function. Red line: critical angle for XUV computed from static dielectric function, clearly tracking the zero of $dR/d\epsilon_2$.

3.3.5 Carrier and phonon thermalization kinetics

The dielectric function extracted in Figure 21a,b allows determination of carrier dynamics initiated by the NIR pump. The electron and hole positions, extracted by the fit to equation 1, are shown in Figure 23a, along with bi-exponential fits. Both features show a rapid shift toward the band edge, ($\tau_1 = 600\pm300$ fs for holes, $\tau_1 = 400\pm300$ fs for electrons), followed by slower shifts toward the respective band edges ($\tau_2 = 4.8\pm0.7$ ps for holes, $\tau_2 = 5.5\pm1.2$ ps for electrons), which are similar within experimental error.

The timescale of the initial rapid decay of the carrier features toward the band edge is consistent with thermalization of the hot carrier distributions by carrier-carrier and carrier-phonon scattering following excitation with the pump. Because these dynamics have been studied in detail recently in the XUV, [21] and thoroughly in the past, [110,115,124] we only provide a brief discussion here. For holes, thermalization is dominated by intravalley scattering within the heavy hole band, which should occur on a timescale of approximately 600 fs. [115] Consequently, we assign the 600 fs hole relaxation time to intravalley scattering within the HH band. For electrons, the rapid decay toward the band edge is dominated by intervalley scattering from the Γ and L valleys to the X valley, due to its high density of states. [115,124] Accordingly, we attribute the 400 fs timescale to electron thermalization, mediated by Γ-X and L-X intervalley scattering. Note the large error bars on this number specified above.

The timescale of the slower shifts toward the respective band edges (τ_2=4.8 ps for holes, τ_2=5.5 ps for electrons) is too slow to be attributed to thermalization of the excited electronic distribution (as seen Figure 23a), which has been observed to occur in <1 ps. [125] Instead, we propose that the slower carrier shifts track the renormalization of the band gap by acoustic phonons created by electron-phonon and phonon-phonon scattering. [126] Initially, the pump produces an excited electron distribution with nearly 8000 K of excess kinetic energy. These carriers should then thermalize via carrier-phonon scattering (~10s-100s of fs), resulting in a buildup of optical phonons. [24] Optical phonons then decay via anharmonic decay into 2 lower-energy acoustic phonons. [127] The resulting acoustic phonons then modify the band gap via either electron-phonon coupling, or thermally induced lattice expansion. [128–130] The observed timescales are inconsistent with previous work which observed thermally induced lattice expansion in Germanium on a much longer time scale (75 ps). [131] Accordingly, we attribute the band gap shrinkage to renormalization by acoustic phonons, which results in the apparent movement of the carrier energies in Fig. 4a toward the band gap. In this case, we can then identify the time constants of 4.8 ps and 5.5 ps (similar within error) as decay times for anharmonic decay of an optical phonon into 2 acoustic phonons. Our measured decay times match well with LO lifetimes of 4 ps, previously measured in Ge. [26] Accordingly, we attribute the 4.8 and 5.5 ps timescales to decay of the LO phonon population, which tracks the thermally induced bang gap shift.

Lineouts along the maximum of the electron and hole features from 3d are incorporated into Figure 23b, showing the decay of the electron and hole contributions to the absorptive $\Delta\epsilon_2$. Both contributions decay rapidly, although the decay cannot be well fit with a single exponential. By definition, the carrier contribution to ϵ_2 is directly proportional to excited carrier density, weighted by the XUV transition dipole element (equation 3.6), hence decay of the transient dielectric function modification reports on two processes: depletion of the excited carrier distribution and intervalley scattering of the carrier distribution between regions of different XUV oscillator strengths.

The fact that the electron- and hole-induced dielectric changes (Figure 23b) show substantial decay within 10 ps means that surface recombination cannot explain the kinetics observed, as carrier recombination is observed to occur on the μs timescale. [132] To further understand the origin of the electron and hole kinetics, we modeled the spatial evolution of the excited carrier distribution after excitation (SI), including Auger recombination, and a temperature dependent diffusion constant. [25,108–110,112] Because the pump is much larger than the probe, diffusion parallel to the surface of the wafer is neglected, and only diffusion normal to the surface is considered. [110] By assuming that $\Delta\epsilon_2$ is proportional to the surface carrier density, our simulations (blue solid line in Figure 23b) recreate the hole kinetic trace (blue circles) using an initial carrier density of 3×10^{20} cm^{-3}. Based on the agreement with simulations, we attribute the depletion of the hole signal to diffusion of holes out of the probe interaction region, in conjunction with Auger recombination, in which an electron and hole recombine and transfer excess energy to another electron or hole. These results agree with previous work in germanium, in which carrier diffusion was shown to play a substantial role in hole bleaching on a 6 ps timescale. [110]

By contrast, the electron contribution to $\Delta\epsilon_2$ decays more rapidly and is almost entirely gone by 3 ps. This depletion cannot be explained by a combination of diffusion and Auger recombination, as both of these processes should lead to a persistent signal for over 10 ps. Previous studies have shown that initial excitation in germanium results in rapid transfer of population from the Γ–X valleys, via deformation potential interaction (~200 fs), followed by slow transfer of population of electrons from X–L within ~3 ps [110,115]. Because the L valley is mainly Ge 4s character, while the X valley is mainly Ge 4p character, XUV transitions from the 3d core state to the L valley are forbidden by angular momentum selection rules, while transitions to the X valley are allowed. [21] Thus, electron scattering from the X to the L valleys should result in a depletion of

electron signal. Accordingly, we model the depletion of the electron contribution to $\Delta\epsilon_2$ by considering Auger recombination, diffusion, and a single exponential decay representing X-L intervalley scattering Figure 23b, red line. This allows extraction of an X–L population transfer time constant of 3.2±0.2 ps, which is in good agreement with previous results. [115]

The transient band shift extracted from equation 2 is shown in Figure 23c. It is fit with a combined step function and biexponential decay and rise of the redshift (note negative numbers on the graph) with time constants of 1.8±0.4 ps and 4.0±1.0 ps. The timescale of the rapid initial redshift is too rapid to distinguish in the longer time experiments emphasized here, and it is accordingly attributed to a carrier induced dynamic redshift of the conduction band due to screening by carriers. [133] The observation is additionally supported by a similar carrier induced dynamic redshift in XUV transient absorption in germanium. [21] Previous work has shown that the redshift of the conduction band should scale as the cube root of the excited carrier density. [134] Accordingly, the 1.8 ps decay of the redshift is thus attributed to a depletion of carriers, via Auger recombination and diffusion. Because the rate of Auger recombination goes as n^3, (where n is the carrier density) initially, recombination is relatively faster, and it slows down as recombination occurs. Accordingly, the recovered 1.8 ps timescale retrieved for the band shift should not result in complete depletion of the carriers within 1.8 ps, and this is consistent with the observation of excited carriers out to 10 ps. Finally, the 4 ± 1.0 ps growth of the redshift is attributed to band gap renormalization by the population of acoustic phonon modes, which matches previously measured optical phonon lifetimes. [135] Within error, the agreement of the 4 ps redshift with the 4.8 and 5.5
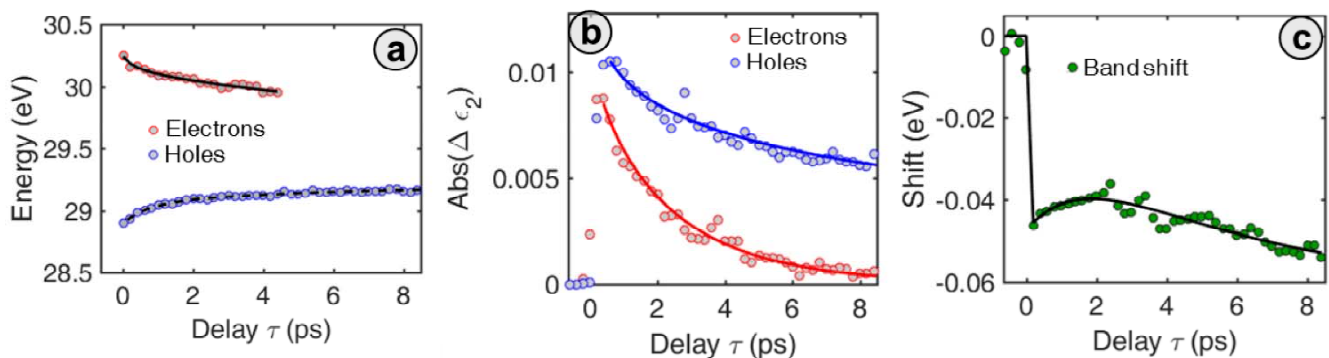
Figure 23: Kinetics Extracted from Dielectric fit (a) Electron (red) and hole (blue) positions (central energies) obtained from equation 3 with bi-exponential fits. The electron position stops at 4 ps due to depletion of electron signal. (b) $\Delta\varepsilon_2$ obtained for electrons (red) and holes (blue) with fits from model (see text) (c) Red shift extracted from modeled dielectric function, along with biexponential fit.

ps timescales shown in Figure 23a provides further support to the assignment of these processes to phonon decay, since all three timescales should ultimately report on the same process. The recovered time constants, their associated errors, and the assigned processes are summarized below in table 2. Although the LO phonon lifetimes derived from the band shift, electron carrier center, and hole carrier center differ slightly, the time constants retrieved are consistent within error. The impact of acoustic phonon induced gap shrinkage is expected to differ for different bands [108,136]. Because the 4 ps timescale obtained from the band shift (Figure 23c) is obtained from a global shift of the entire static spectrum, it should be the most reliable, since it should average out differences in the valley specific band shifts. Accordingly, we take the 4 ps timescale to be the LO phonon lifetime, in good agreement with previous work.

Table 2: Recovered time constants and assigned processes

Time constant	Error	Process	Source
600 fs	300 fs	Hole relaxation	Carrier center
400 fs	300 fs	Electron relaxation	Carrier center
1.8 ps	400 fs	Diffusion/Recombination	Band shift decay
3.2 ps	200 fs	X-L Electron scattering	Electron signal decay
4.0 ps	1.0 ps	LO Phonon lifetime	Band shift growth
4.8 ps	700 fs	LO Phonon lifetime	Carrier center
5.5 ps	1.2 ps	LO Phonon lifetime	Carrier center

3.4 Conclusion

XUV transient reflectivity at the Ge $M_{4,5}$ edge was developed, and a framework for interpreting the XUV spectral changes in terms of electron, hole, and phonon contributions spectral contributions was reported. This framework allows simultaneous, independent measurement of electron, hole, and phonon thermalization processes as well as recovery of the time dependent dielectric function following photoexcitation. Further analysis reveals that under our experimental conditions near the critical angle, the XUV TR is dominated by changes to the real part of the dielectric function. Retrieval of the real ϵ_1 and imaginary ϵ_2 allows tracking of carrier centers of

53

energy and relative populations, allowing independent thermalization rates to be simultaneously measured. Hot electron relaxation via Γ-X and L-X intervalley scattering are observed within 400±300 fs, hot hole relaxation via intravalley scattering within the HH band are observed within 600±300 fs, in agreement with previous work. [115] Additionally, electron X–L intervalley scattering was observed within 3.2±0.2 ps. Band gap renormalization by electron-phonon coupling via acoustic phonons, previously unresolvable in XUV absorption measurements, was observed within 4-5 ps, in good agreement with previously measured optical phonon lifetimes. [26] The agreement of the observed relaxation kinetics with those previously measured using optical methods highlights the fact that XUV transient reflectivity can be used quantify the carrier dynamics and band gap shifts in semiconductors, and the method can overcome the thin sample issues associated with XUV Transient absorption. The framework put forth in this work allows for rigorous interpretation of XUV Transient Reflectivity spectral components, and opens the door for attosecond investigation of ultrafast process in materials that are inaccessible by absorption methods.

Chapter 4: Attosecond Transient Reflectivity of Germanium

The interaction of coherent light with matter can modify the electronic structure of a solid through dressing of the band structure with photons, leading to new material properties. Here, attosecond transient reflectivity is developed to allow possible observation of rapid oscillatory behavior in the valence and conduction bands of germanium during photoexcitation. A period of oscillation observed is consistent with coherent electron-hole pairs, however systematic experimental error cannot be ruled out as the origin of the oscillation. Additionally, other signals above and below the Fermi-level are observed, which may be consistent with the creation and population of Floquet-Bloch bands. However, without further work, these features cannot be definitively assigned to Floquet-Bloch bands. While definitive discovery and assignment of various short time dynamics are elusive, this work lays the groundwork for future investigations of attosecond dynamics of semiconductors with attosecond transient reflectivity, and it identifies potentially interesting behavior that warrants further investigation.

4.1 Introduction

Coherent light-matter interactions in atoms and molecules can lead to hybridized photon-matter states, referred to as laser-dressed states [137]. Dressed states are critical in the description of optical properties of atoms and molecules in laser fields and for the implementation of schemes for optical pumping and laser cooling. Recently, laser dressing of electronic bands in solids [138] has gained substantial interest due to the potential for engineering material properties. Theoretical work has described how to turn semiconductor quantum wells into a Floquet topological insulator by microwave frequencies [139], create topologically protected states in graphene under mid-infrared irradiation [140], and switch material properties between Weyl semimetal, Dirac semimetal, and topological insulator states

by 800 nm laser pulses [141]. Successful demonstrations to laser-switch material properties include the realization of Floquet topological insulators by coupled waveguides [142], transient laser-induced phase transitions, [143–145] and the excitations of collective modes in superconductors [146]. Here, attosecond transient reflectivity is used to monitor even shorter real-time photoexcitation dynamics in germanium, with the intent to reveal the possible creation of laser dressed states, as well as the excitation of coherent electron-hole dynamics with periods from < 10 fs.

Floquet-Bloch states in solids, which are replicas of the Bloch bands by integer multiples of the photon energy of the dressing laser pulses, were first experimentally reported on the surface of a topological insulator under laser irradiation [147,148] by angle-resolved photoemission spectroscopy (ARPES). ARPES is extremely powerful for measuring the band structure as well as femtosecond to picosecond dynamics, while attosecond measurements add the new capability to observe real-time electron dynamics.

Attosecond metrology [149] has resolved electron transport and excited states lifetimes following XUV single-photon ionization in solids [150–152] and nanoparticles [153,154] on timescales of a few tens to hundreds of attoseconds and monitored the dynamics of laser-dressed states in noble gases. [155–158] Strong-field induced attosecond electron dynamics by visible to near-infrared (VIS/NIR) pulses can lead to high-harmonic generation in solids [31,159,160]. The underlying field-driven transient electron dynamics can be resolved by attosecond transient absorption [17]. Extreme ultraviolet (XUV) transient absorption of solids has been powerful in revealing transient band polarizations and Stark shifts on time scales corresponding to multiples of the center frequency of the VIS/NIR pump pulses [16–18] and in observing carrier dynamics after photoinjection of electrons into the conduction band (CB) [11,15] However, attosecond transient absorption is limited to thin samples, which are rarely single crystals. The periodic structure of single crystals is required for the formation of the laser-dressed Floquet- Bloch states, due to the requirement of a periodic potential in both time, through the laser pulses (the eigenfunctions of which are called Floquet states), and space, through the crystal structure (the eigenfunctions of which are called Bloch states).
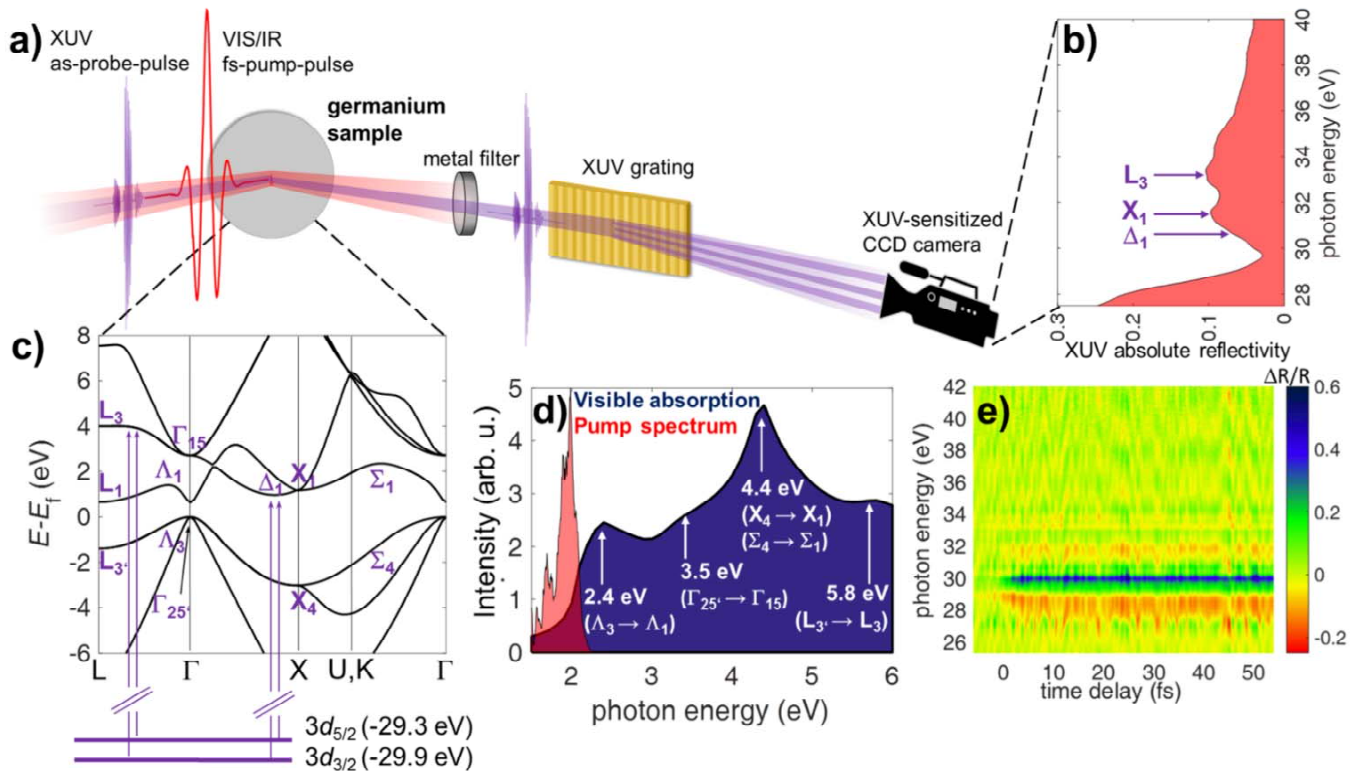
Figure 24 Concept of the experiment: A) Scheme of the experimental setup. B) Static XUV reflectivity of germanium. C) Band structure of germanium. The violet arrows indicate XUV transitions. D) Spectrum of the VIS/NIR pump pulses (red) and visible absorption spectrum (blue, adapted from ref (28)). The maxima of the absorption spectrum are assigned to specific regions in the band structure. E) Transient reflectivity signal of germanium. Positive delays correspond to VIS/NIR pulses preceding the XUV pulses.

4.2 Methods

4.2.1 Transient Reflectivity

To overcome the limitations of current attosecond and photoemission techniques, and to provide a new technique that can follow the full dielectric response of a solid, attosecond transient reflectivity in the XUV was developed as discussed above and used to monitor the possible coherent electron excitation dynamics in possible laser-induced Floquet-Bloch states of germanium. Transient reflectivity is sensitive to the real and imaginary parts of the refractive

index and thus monitors the complete dielectric response of the sample to external fields. In the experiment, intense VIS/NIR pump pulses photoexcite germanium and simultaneously dress the valence and conduction bands. Extreme ultraviolet attosecond pulses produced by high-harmonic generation at 30 eV interrogate the dynamics at the Ge $M_{4,5}$ edges by promotion of electrons from the 3d core orbitals into unoccupied valence bands (VBs) and CBs. Transient reflectivity encodes spectral signatures of holes, electrons and band-gap renormalization in the transient reflectivity through changes of the real and imaginary part of the refractive index.

The experimental setup shown in Figure 24a has been designed to obtain absolute intensity calibrated reflectivities from the sample. The static XUV reflectivity of Ge in Figure 24b can be interpreted in a similar way as an absorbance [161]. This correspondence holds best for normal incidence and is approximately true for other angles, so long as the real part of the refractive index is near unity, which is generally the case in the XUV. The dip and sharp rise around 29.5 eV in the static reflection spectrum (Figure 24b) correspond to the onset of core-to-conduction band transitions, which increases the absorption. Other maxima in the reflection spectra can be assigned to valleys in the CB when there is a high density of states that have p-orbital character. The changes in curvature around 30 eV and the maximum around 30.5 eV correspond to the Δ_1 and X_1 points in the band structure in Figure 24c, respectively, while the maximum around 33.5 eV corresponds to the L_3 valley.

4.2.2 Band-Structure calculations

Density functional theory (DFT) within the Vienna ab-initio simulation package (VASP) is used to calculate the band structure of germanium (Figure 24c). The same calculations were employed in ref. [21]. A generalized gradient approximation and Hubbard (GGA+U) approach were used. Details on the computational method and parameters can be found in ref. [21].
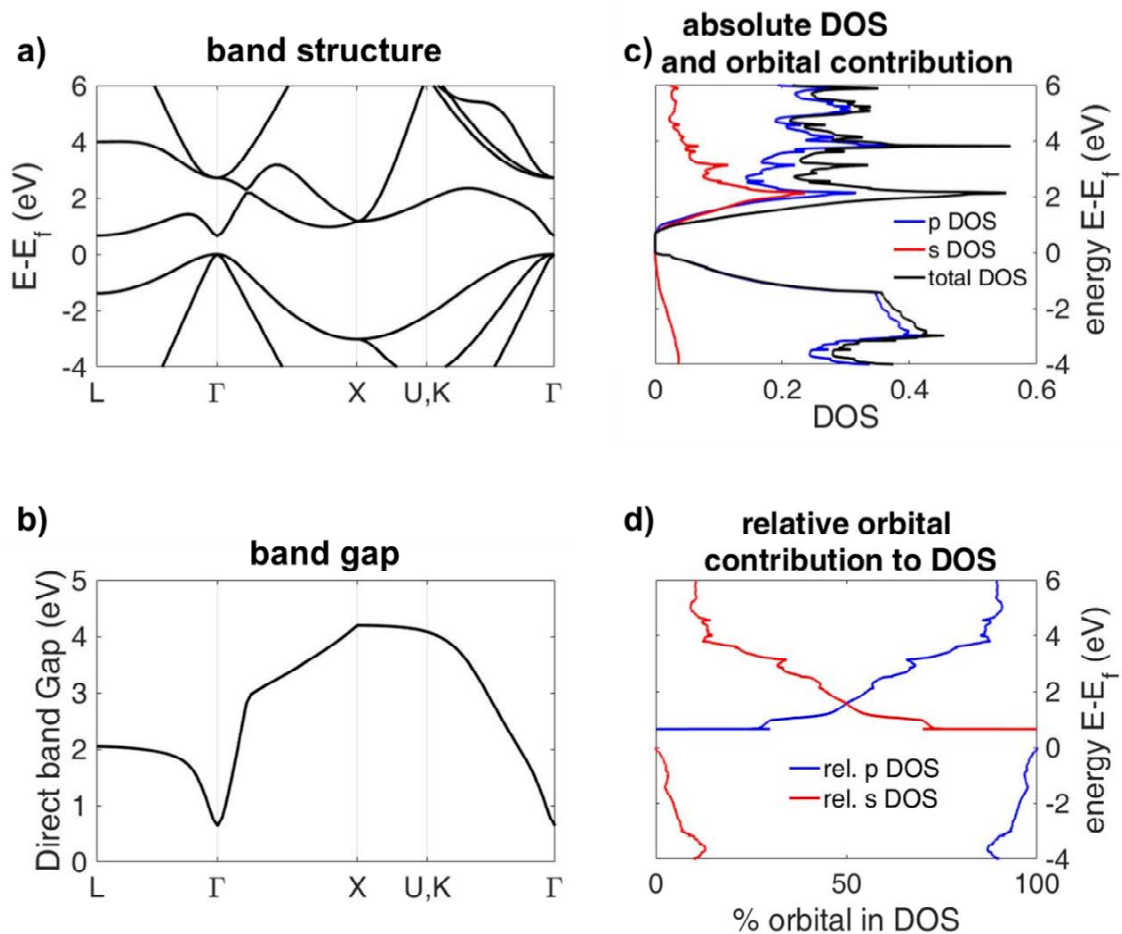
Figure 25: Band structure, band gap and DOS of Ge (a) Band structure of Ge. (b) Direct band gap for all k points of the band structure shown in (a). (c) Absolute density of states (DOS) and s-orbital (red) and p-orbital (blue) contributions to the DOS. (d) Relative percentage of orbital contributions to the band structure.

The band structure is shown in Figure 25a for completeness. The direct band gap for the same points in k-space is shown in Figure 25b. The absolute density of states (DOS, black) is shown in Figure 25c together with the relative p-orbital (blue) and s-orbital (red) contributions. The percentage of the relative orbital contributions to all energies is shown in Figure 25d.

The absolute and relative orbital contributions to the DOS (Figure 25c,d) indicate that most of the VB has p-character. Thus the XUV transitions from 3d orbitals will mainly probe holes in the VB. The CB has stronger s-orbital character, nevertheless hybridization of atomic orbitals leads to significant p-orbital contributions. However, the regions at the Γ and L valley,

where the direct band gap (Figure 25b) is directly accessible by one-photon excitation, mostly consist of 4s orbitals, which makes the XUV probe less sensitive to the dynamics in these regions of the CB.

4.2.3 Assignment of the UV/VIS spectrum

The visible absorption spectrum of germanium is shown in Figure 24d and was adapted from ref. [79] The assignment was based on the band structure shown in Figure 25a,b and the previous assignment by Brust et al. in ref. [80] . The direct band gaps from the $\Lambda_3 \rightarrow \Lambda_1$ to the $L_3 \rightarrow L_1$ transitions were found to be around 2 eV in our DFT calculations. The $L_3 \rightarrow L_1$ transition was assigned to the rising onset of the absorption at 2.1 eV, and the $\Lambda_3 \rightarrow \Lambda_1$ transition to the maximum at 2.3 eV in ref. [80] .The more recent measurement of the absorption spectrum in [79] found the maximum in the absorption spectrum at 2.4 eV which agrees exactly with the center frequency of the experimentally observed dynamics. The direct band gaps from the $X_4 \rightarrow X_1$ to the $\Sigma_4 \rightarrow \Sigma_1$ transitions are around 4 eV in the calculation in Fig Figure 25 . The maxima from 4.3 to 4.4 eV in ref. [80] were assigned to this transition.

4.2.4 Data analysis of attosecond transient reflectivity signals

For all Fourier analyses shown in the discussion, the rising part of the signal for each energy was subtracted by smoothing the signal at each recorded photon energy over 50 delay points (each delay point has a time separation of 67 as). This subtraction isolates the oscillatory components of the signal, which would otherwise be overshadowed by a strong and broad dc component that is due to the slowly rising part of the signal. Physically, this slowly rising signal is due to the gradual photoinjection of carries from the VB into the CB. While this method has merits, it also exposes the experimental analysis to artifacts. In the sections below, an analysis is first made and then a critique of the assessment in considered in detail.
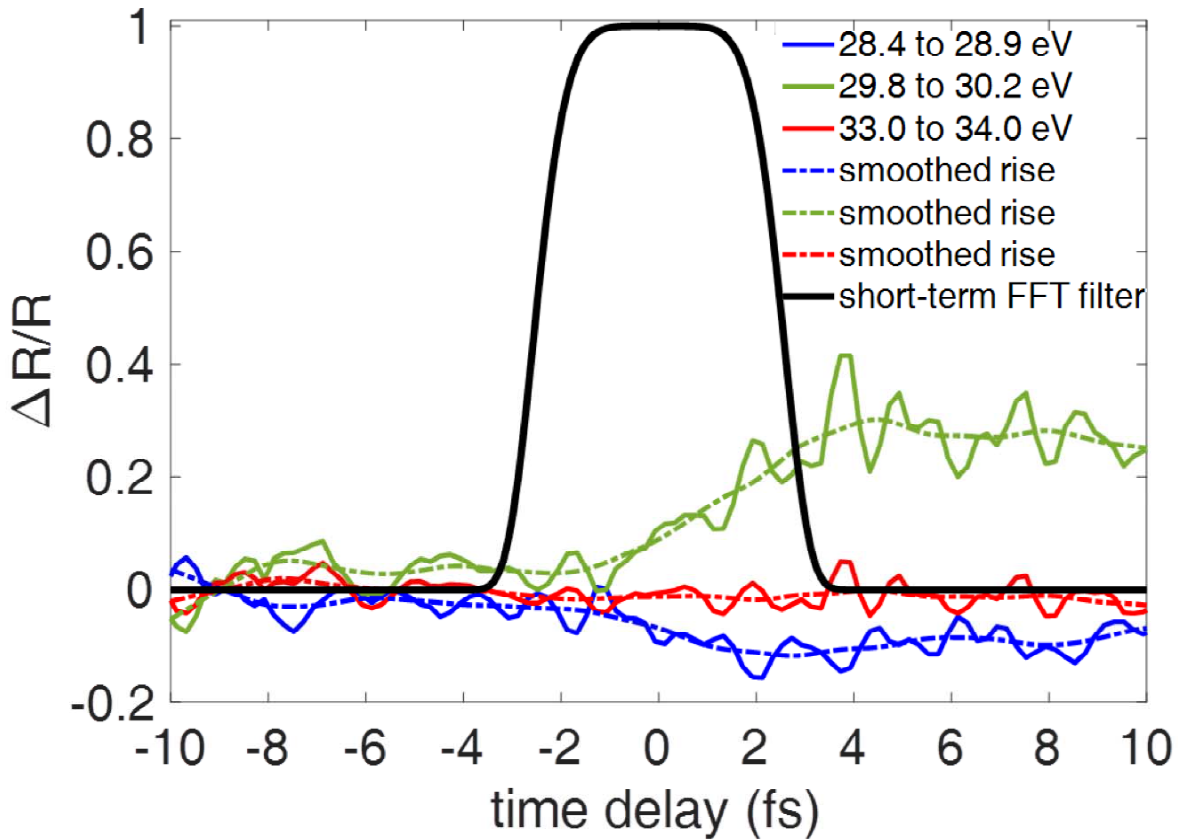
Figure 26: Energy lineouts and time-window for short-term FFT Energy lineouts at various energies from the transient reflectivity scans of germanium are shown. For Fourier-transforming the data, the slow rise of the reflectivity signal, which is due to the gradual carrier excitation, is treated as background by smoothing the signal over 50 data points (shown as dash-dotted lines) and subtracting these values for every energy prior to Fourier-transforming. This procedure removes a strong DC component in the Fourier transform, which otherwise overshadows the other frequency components. For the short-time FFT the Fourier transform is additionally temporally gated by the time window (black line).

For the short-time Fourier transform, which is sometimes also referred to as Gabor transform, a 3rd order Gaussian time window with 5 fs FWHM is slid along the data, and a Fourier transform is calculated for selected delay points of the time window as shown in Figure 26. Just as the Nyquist frequency poses an upper limit to the fastest resolvable oscillations given by the sampling interval, the Rayleigh frequency poses a lower limit, which is given by the total length of a time scan, or in the case of a short-time Fourier transform by the FWHM of the time window. These frequencies pose the axis limits of the frequencies shown in Figure 27 e,f.

4.3 Results and Discussion

4.3.1 Transient Features

In the experiment, sub-5 fs VIS/NIR pump pulses with a spectrum spanning from 550 nm -1000 nm (1.2 eV- 2.3 eV, Figure 24d) centered at 680 nm (ω = 1.8 eV) simultaneously photoexcite carriers above the band gap (indirect: 0.66 eV, direct: 0.8 eV) and presumably dress the bands.

A transient reflectivity signal over the first 50 fs after photoexcitation is shown in Figure 24e. The spectral signatures of electrons and holes contribute to the two strong transient signals with opposite signs at 28 eV and 30 eV, respectively [50]. A detailed analysis shows that the holes have the strongest contribution to the transient signal due to their strong p-orbital character.

Figure 27a zooms into the time delay region when pump and probe pulses are coincident in time at one particular laser intensity indicated in the figure, and a lower laser intensity is shown in Figure 27b. Fast oscillations across the whole recorded XUV spectrum from 25 eV to 45 eV appear to be present. Energy lineouts of the reflectivity changes are shown in Figure 27c,d. The transient reflectivities exhibit multi-frequency oscillations. Multi-frequency oscillations faster than 2ω (i.e. 3.6 eV, corresponding to a 1.2 fs beating) are apparent between 2 fs and 6 fs. Oscillations at a frequency of 2ω are expected for transient polarizations and Stark shifts of the band structure [17,162] or field-induced tunneling [15], which are processes that follow the absolute value of the electric field of the pump pulses. Fourier transforms of Figure 27a,b are shown in Figure 27e,f .Three strong frequency components (vertical axis) appear to be at 2.4 eV, 3.6 eV, and 4.5 eV in Figure 27e. In addition, these frequencies are repeated in multiples of the fundamental pump energy (1.8 eV) in the photon energy axis.

First, the frequencies in the frequency (horizontal) axis are analyzed. The frequencies at 2.4 eV and 4.5 eV appear within the frequency-resolution of the FT almost exactly at energies where the visible absorption shows maxima (Figure 24d), which correspond to the energies where the pump pulses create the largest population of electron-hole pairs in the Λ valleys (2.4 eV) as well as the X and Σ valleys (4.5 eV). The initial coherence of the electron hole-pairs maps to an oscillation in the time domain signal with a periodicity proportional to the inverse energy

separation. Thus the detection of frequencies commensurate with the energy of band-gap excitations could be interpreted as a direct observation of a coherent evolution of an electron-hole pair. The frequency at 3.6 eV is twice the center frequency of our VIS/NIR pump pulses and could indicate a transient polarization of the bands. The inset in Figure 27e shows a zoom of the photon energies from 29 - 32 eV for frequencies from 5 to 8 eV on a different color axis. Another frequency at 5.7 eV visible, which is close to the local maximum at 5.8 eV in the absorption spectrum corresponding to $L_3 \rightarrow L_3$ excitation, and a broad component at 7 eV is present, which is close to a 4ω (7.2 eV) component.
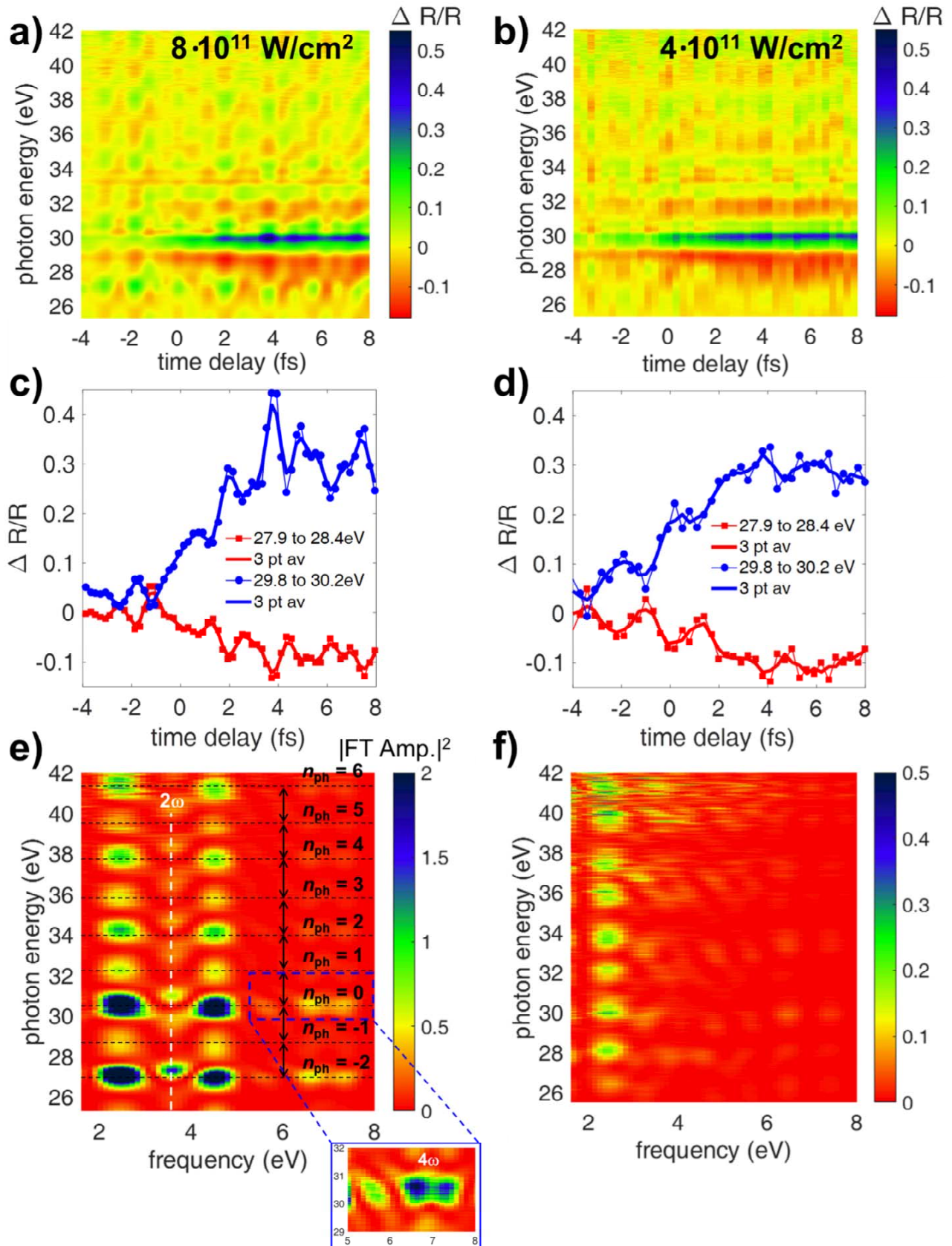
Figure 27 Experimental observation of attosecond electron dynamics in Floquet-Bloch bands: (a) Attosecond oscillations of the reflectivity changes at 8E11 W/cm² and (b) 4E11W/cm². (c,d) Outlines of the reflectivity changes from (a,b) for selected energies. (e,f) Fourier transforms of (a,b) during the main interaction between germanium and the pump pulse from 0.9 fs to 7.7 fs.

While 2.4 eV is close to edge of our visible absorption spectrum, electron-hole pairs at 4.5 eV can only be excited by a two- or three-photon transition. This is supported by examining the oscillations of the lower intensity transients in Figure 27d, the Fourier transform of which is shown in Figure 27f. The oscillations, and thus the magnitudes in the Fourier transform are weaker. Importantly, the 4.5 eV oscillation frequency, which is accessed by multiphoton transitions, is not present anymore.

In the photon energy (vertical) axis, all frequencies in Figure 27e,f appear to be repeated by an energy separation of 1.8 eV, which is equal to the center frequency of the pump pulses. This could be consistent with laser dressing of all bands, which causes the occupied VB and CB to be repeated in multiples of the photon energy. Previously, the concepts of Floquet theory and laser dressing have been applied to interpret the broadening of sidebands in attosecond transient absorption measurements of atoms [155–158]. This motivated the search for such features, although as noted below, the evidence is not yet convincing. In general, Floquet-Bloch bands are periodic in both energy and momentum, and the excitations of coherent electron-hole pairs add periodicity in time. Consequently, the strong features around 30.5 eV would potentially be consistent with the electron-hole pairs between the undressed VB and CB. The features at 32.3 eV and 28.7 eV could correspond to dressing with +1 and −1 photon, respectively. The oscillations at the highest photon energy around 41.3 eV would correspond to dressing by +6 photons, as indicated in Figure 27e. Interestingly, every odd multiple of the frequency pattern in Figure 27e (e.g. at 32.3 eV, 35.9 eV, etc.) is less intense than the even multiples (e.g. at 34.1 eV, 37.7 eV, etc.), which can be interpreted as a consequence of the sensitivity of XUV transient reflectivity to the parity of the state into which the transition occurs. The parity of the transition changes for dressing with an odd number of photons, which reduces the XUV transition strength for probing holes with p-orbital character. This effect seems to be stronger for higher intensities, as it is not clearly observed in Figure 27f.

4.3.2 Error analysis and alternative explanation

The dynamics and oscillations described in section 4.3.1, while interesting, contain some substantial problems, which render the claims of observation of both coherence and Floquet

states suspect. To illustrate this, we show the lineouts from Figure 27c, extended out to 50 fs, Figure 28. In this plot, the oscillations at the VB (27.9-28.4 eV), and conduction band (29.8-30.2 eV), are shown in red and blue, respectively. As is clear in the plot, the oscillatory behavior lasts out to 50 fs. Because the explanation described in the previous section suggests that oscillations within the VB and CB are due to a laser-induced coherence between the valence band and conduction band, the oscillations present in these bands should die out with the coherence lifetime of the system, which can be estimated to be around 10 fs based on photon echo measurements in GaAs [22]. As such, the persistence of the oscillations out to >50 fs is
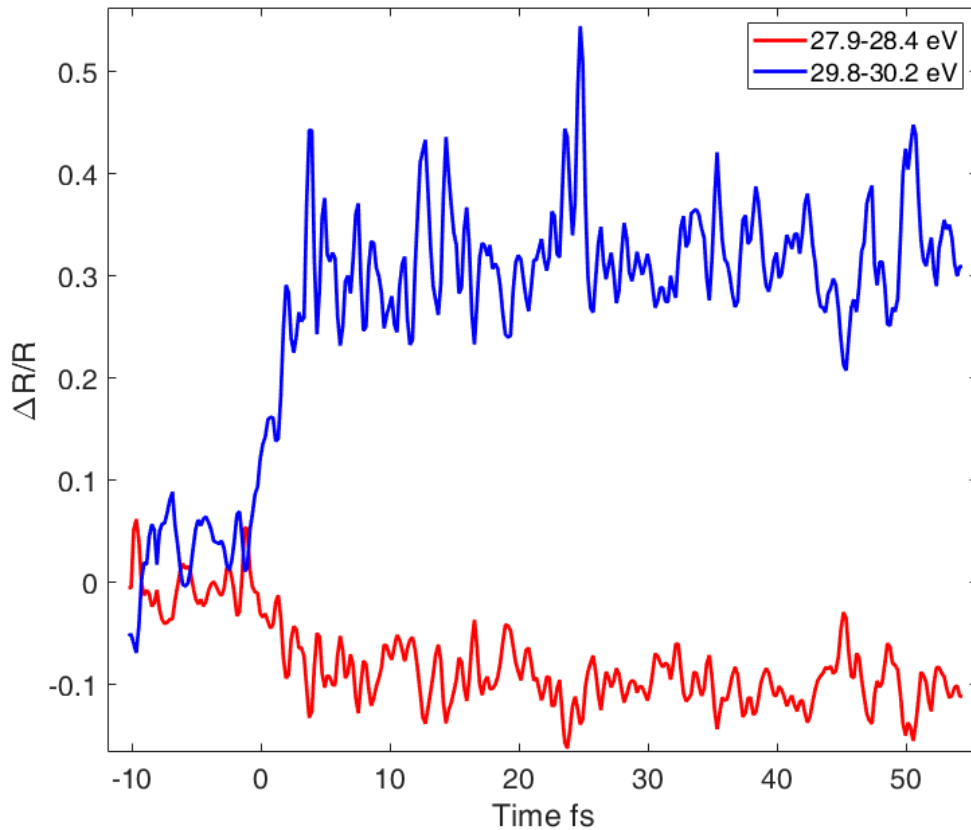
Figure 28: Lineouts of transient reflectivity, showing oscillations lasting out to 50 fs. (Red) 27.9-28.4eV averaged dR/R. Blue, 28.9-30.2eV averaged dR/R.

implausible. Accordingly, the oscillations at the VB and CB energies cannot be definitively attributed to coherences, and are likely instead due to some systematic error. More problematically, the oscillations that seem to be present in the VB and CB cannot be reliably

reproduced, and are in fact absent from many datasets with higher signal to noise, as show in Figure 29.
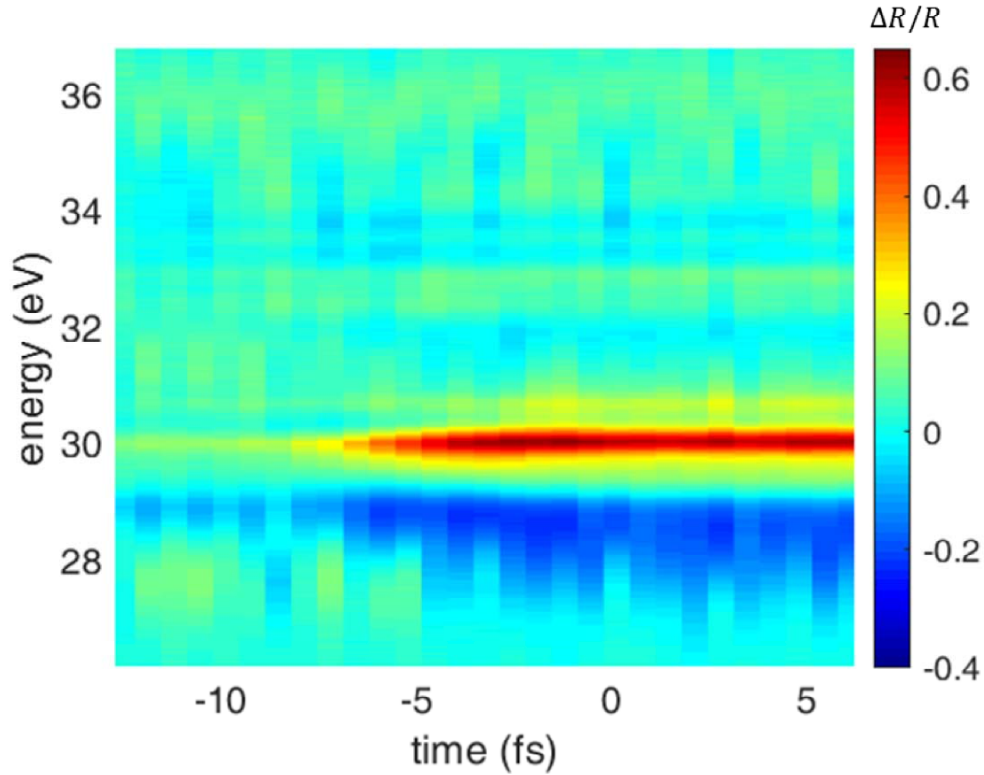
Figure 29: Transient reflectivity showing no oscillations. Step size 667 as.

Similarly, the oscillations at higher photon energies, which manifest as a series of spots in the vertical dimension of Figure 27e spaced by $\hbar\omega$ eV, possibly attributed to the creation of Floquet dressed copies of the original VB-CB coherence, are also suspicious. Namely, the Floquet dressing of the VB-CB coherence should also result in the creation of new transient reflectivity features in Figure 27a, and only during the time overlap of the two pulse. Because no such features are apparent, we suggest that the presence of oscillations at higher photon energies may actually be due to the same systematic error that resulted in oscillatory behavior near the VB and CB. The vertical $\hbar\omega$ spacing of the oscillations in the vertical dimension (shown in Figure 27e) is highly consistent with fluctuations of the high harmonic spectrum, which can result in periodic noise spaced by $\hbar\omega$ in the energy domain. Accordingly, we cannot rule out the

hypothesis that the periodic structure of the oscillations in the vertical dimension, are simply due to high harmonic modulation.

In order to confirm the assignment of the oscillatory structure observed to coherences and the formation of dressed states, more experiments are required. First, reproducibility of the oscillations at the VB and CB energies must be established, to confirm the basic hypothesized laser induced VB-CB coherence. Second, varying the pump wavelength while holding constant the wavelength of the HHG driver would allow independent testing of the creation of the Floquet states. Inspecting equation 4.5 below reveals that the energy of the Floquet states should depend on the frequency of the dressing laser. Thus, if the pump laser frequency is changed while holding the HHG driver constant, the spacing of the structure in Figure 27e should be observed to exactly match the frequency of the pump laser, and the assignment of the structure to the creation of Floquet states can be supported.

4.3.3 Dressed State Calculations

In this section a model for the laser-matter interaction with germanium is presented, to develop the notion of laser dressing and the production of possible Floquet Bloch bands. The laser-matter interaction is formulated using Floquet theory, where both the periodicity of the laser field is explicitly taken into account, and the periodicity due to the periodic potential of the crystal is considered. Laser dressing during photoexcitation would lead to the creation of replicas of the valence and conduction band separated by the photon energy. In addition, the replicas and original bands would be energetically shifted as a function of the laser intensity, reminiscent of a Stark effect. Solving the time-dependent problem further reveals that the laser-induced bands should be transiently populated during the laser-matter interaction, leading to attosecond electron dynamics of the photoexcited charge carriers.

We wish to solve the time-dependent Schrödinger equation for a time-dependent Hamiltonian $\mathcal{H}(t)$ and wave function $\Psi(t)$:

$$i\frac{\partial\Psi(t)}{\partial t} = \mathcal{H}(t)\Psi(t) \tag{4.1}$$

The time-dependent electronic Hamiltonian (atomic units are used throughout this discussion) for electrons in band-structure solids is

$$\mathcal{H}(t) = \sum_{\lambda} \epsilon_{\lambda}(k)\hat{a}^{\dagger}_{\lambda,k}\,\hat{a}_{\lambda,k} - E(t)\sum_{\lambda,\lambda'}\mu_{\lambda\lambda'}(k)\hat{a}^{\dagger}_{\lambda,k}\,\hat{a}_{\lambda,k} \tag{4.2}$$

Where the indices k and $\lambda(\lambda')$ refer to the electron wave numbers and band labels respectively. Further, $\hat{a}^{\dagger}_{\lambda,k}$ is the creation operator for an electron with wave number k in band λ, and $\epsilon_{\lambda}(k)$ is the electron energy for a given band λ and wave number k. The electric field is denoted as *E(t)*, and $\mu_{\lambda\lambda'}(k)$ is the interband transition dipole moment. The two terms describe (from left to right), the Hamiltonian for the electronic band structure of the solid (in the following abbreviated as $\mathcal{H}_0$) and the interband excitations of the electrons (also called inter-band polarizations). In principle, the acceleration and field-driven dynamics of the electrons within one band, called intra-band polarization, also occurs, which is the term giving rise to Bloch oscillations. This term is dominant in off-resonant dynamics driven by longer wavelengths, or in insulators with larger band gaps.

We now choose a basis for the wave function in the laser field $\Psi(t)$:

$$\Psi(t) = \sum_{n,v} C_{n,v}(t)e^{-i(\epsilon_v + n\omega)t}\phi_{n,v} \tag{4.3}$$

Where n is an integer, which can be interpreted as the number of photons that the band structure is dressed with, $C_{n,v}(t)$ are time dependent coefficients, and $\phi_{n,v}$ are the field-free wave functions, i.e. the bands v with energies ϵ_v.

Inserting this ansatz for the wave functions into equation 4.2, and multiplying by $\langle\phi_{n',v'}|$ gives:

$$i\frac{\partial C_{n',v'}(t)}{\partial t}e^{-i(\epsilon_{v'}+n'\omega)t} = \sum C_{n,v}(t)e^{-i(\epsilon_v+n\omega)t}\,\langle\phi_{n',v'}|\mathcal{H}(t) - (\epsilon_v + n\omega)\delta_{v,v'}\delta_{n,n'}|\phi_{n,v}\rangle \tag{4.4}$$

The summation as denoted on the right hand-side represents the Fourier components of the full Hamiltonian. This Fourier representation of a Hamiltonian in a laser field is the Floquet Hamiltonian:

$$H_F = \begin{bmatrix} \ddots & \vdots & \vdots & \vdots & \vdots & \vdots & \ddots \\ \cdots & \widehat{H}^0 - 2\omega\delta_{v,v'} & \widehat{H}^1 & \widehat{H}^2 & \widehat{H}^3 & \widehat{H}^4 & \cdots \\ \cdots & \widehat{H}^{-1} & \widehat{H}^0 - \omega\delta_{v,v'} & \widehat{H}^1 & \widehat{H}^2 & \widehat{H}^3 & \cdots \\ \cdots & \widehat{H}^{-2} & \widehat{H}^{-1} & \widehat{H}^0 + 0\omega\delta_{v,v'} & \widehat{H}^1 & \widehat{H}^2 & \cdots \\ \cdots & \widehat{H}^{-3} & \widehat{H}^{-2} & \widehat{H}^{-1} & \widehat{H}^0 + \omega\delta_{v,v'} & \widehat{H}^1 & \cdots \\ \cdots & \widehat{H}^{-4} & \widehat{H}^{-3} & \widehat{H}^{-2} & \widehat{H}^{-1} & \widehat{H}^0 + 2\omega\delta_{v,v'} & \cdots \\ \ddots & \vdots & \vdots & \vdots & \vdots & \vdots & \ddots \end{bmatrix} \quad \textbf{(4.5)}$$

This Hamiltonian can be used and substituted into Equation 4.4, leading to a set of coupled rate equations

$$i\frac{\partial \vec{C}(t)}{\partial t} = H_F(t)\vec{C}(t)$$

$\textbf{(4.6)}$

which are the underlying equations that are solved to compute the population dynamics shown in Figure 30c.

4.3.4 Floquet Model Calculations

A schematic of laser-induced modifications of a band structure leading to the formation and coherent population of Floquet-Bloch bands is illustrated in Figure 30. Figure 30a zooms in the band structure of Figure 24c, highlighting the VB and CB. In the presence of a static DC electric field, the band structure would already be dressed by the Bloch frequency of the electrons, which describes the motion of an electron in a periodic potential under a constant force. In the presence of an electric field, the frequency of which is close to resonant with the band gap, dressing of the band structure by energies quantized in multiples of the center
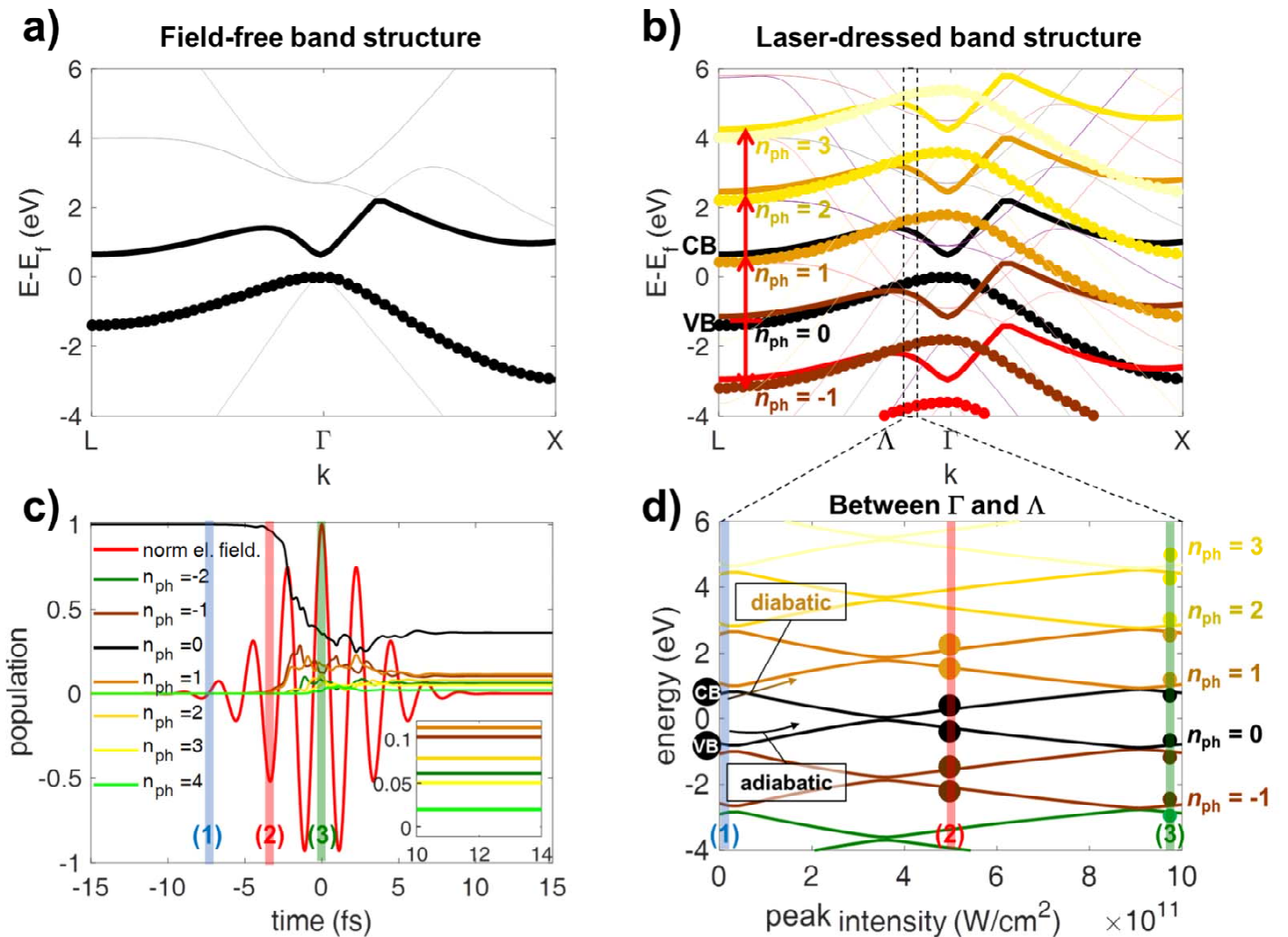
Figure 30 Simulations of electron dynamics in Floquet-Bloch bands: (a) Field-free band structure of germanium. (b) Laser-dressed band structure of germanium. (c) Population of all bands dressed with n photons, i.e. one line in (c) corresponds to the population of all bands in (a) with the same color. (d) Stark shifts of the laser dressed bands for the Λ valley as marked in (b).

frequency of the pump spectrum is the dominant effect. Bloch oscillations could become dominant for off-resonant long-wavelength pump pulses and wide band-gap insulators. The dressing of the band structure with low intensity pulses (i.e. in the absence of transient polarizations and Stark shifts of the bands) is shown in Figure 30b. Laser dressing closes the band gap, as new laser-dressed bands arise within the field-free band gap. This can be interpreted as a laser-induced phase transition from a semiconductor to a conductor, which is related to the previously demonstrated transient conductivity switching of dielectrics as described in ref. [163].

The carrier excitation into the laser-dressed bands is calculated and shown in Figure 30c, and the laser-induced modifications to the band structure as a function of intensity are shown in Figure 30d for a selected point in k-space between the Λ and Γ valley. The model in Figure 30c reduces the band structure to five critical points carrying the highest joint density of states between 0 and 6 eV in the VB and CB, and it allows dressing of the band-structure with up to 20 photons. In Figure 30c we show the populations of all bands for a given number of dressed photons, which corresponds to all bands of the same color in Figure 30b, in order to illustrate the successive population buildup in higher laser-dressed states. Figure 30c shows populations, as opposed to coherences, which could be consistent with strong frequencies at 2.4 and 4.5 eV. In the simulations, the initial population starts in the undressed VB. This population is depleted when the laser field rises. Higher laser-dressed Floquet bands are gradually being populated. Bands that are dressed with a lower number of photons are populated before those dressed with a higher number of photons. The population of the Floquet-Bloch bands persists after the laser pulse, consistent with multiphoton excitation into higher energy CBs of the field-free band structure [147] and resulting in highly excited carriers. Significant population buildup in Floquet-Bloch bands dressed with up to $n = \pm 4$ photons is shown in Figure 30c.

During laser-matter interaction, the bands are transiently shifted in energy. Figure 30d shows these energy shifts by isolating the dressed and undressed VB and CB at one point in k space between the Γ and Λ valley with a direct band gap of 1.5 eV. In the early rising part of the electric field (marked as time (1) in blue in Figure 30c and d), direct single-photon excitation can promote carriers from the VB into the CB. When the field oscillations pass a value that exceeds a crossing of the Stark shifted energies in Figure 30d, the electronic populations can cross the

bifurcation of the energy curves adiabatically or diabatically. Diabatic crossings lead to the population of photon-dressed states. This causes the rise of populations for bands dressed with n = ±1 photons in Figure 30c (marked as time (2) in red). Multiple crossings of these bifurcations can cause gradual buildup of populations in those photon-dressed states. For the highest intensity (marked as time (3) in green), more bifurcations are crossed, and more population is transferred into higher photon-dressed states. If the bands are degenerate, or if more than only two bands are close in energy, the couplings become more complicated and will generally give rise to more bifurcations than those displayed in Figure 30d, which facilitates a more efficient population transfer into Floquet-Bloch bands dressed with a higher number of photons. If one bifurcation of the bands occurs in a single half-cycle, population buildup occurs in steps with a periodicity of 2ω. If multiple crossings occur in one half-cycle of the field, the population can bifurcate at several points, and oscillation components higher than 2ω become possible. The strong Stark shifts displayed in Figure 30d would not be directly observed as energy shifts in the transient signal, as all band energies of germanium (i.e. before and after XUV-probing) will shift by a similar magnitude, leaving the energy of the XUV transition nearly unchanged [17]. Importantly,

4.5 Conclusion

Much work still remains before the assessment of the present experiments as due to Floquet Bloch bands and electronic coherences can be validated. If such speculation regarding,the results can be confirmed, it could pave the way towards coherent manipulation of the optoelectronic properties of semiconductor devices and possibly other materials. While the pulsed laser intensities employed in the current study exceed the continuous wave (cw) damage threshold, theoretical work has already emphasized the possibility to use cw microwave frequencies for laser-engineering material properties [139]. Attosecond transient reflectivity is an important new method in this context for investigating the electron dynamics in the newly formed bands. Moreover, attosecond transient reflectivity has the potential to become a preeminent technique in solid-state attosecond science due to its general applicability. The possible observation of electronic coherences in bulk single-crystalline germanium demonstrate how attosecond science can be employed in the future to track electronic coherences in

chemically and biologically relevant systems, where coherences are speculated to be responsible for the efficiency in photosynthetic light harvesting. [164]

Chapter 5: Ultrafast core exciton dynamics in MgO

In this chapter XUV transient reflectivity is used to investigate ultrafast dynamics of XUV-induced polarization in MgO, a wide band gap insulator. In the first section the basic concepts of core-level excitons are introduced, and the particular coupling of core-level excitons to the lattice in MgO is described in more detail. In the second section, the experiment is outlined. In the third section, a procedure for recovering the complex valued refractive index from reflection data is described and the static refractive index is analyzed. Subsequently, transient reflectivity of MgO is presented and analyzed, revealing that the underlying dynamics can be described as arising from an optical laser induced coherence of core-level states populated by the XUV pulse.

5.1 Introduction

Attosecond science has investigated core-excited state dynamics in gases, in which coherent electronic states near discrete resonances can be observed and controlled by a strong laser field [165]. Thus far, the same degree of understanding and control in solid state systems, in which many-body dynamics introduce substantially more complexity, has remained out of reach. In this work, we investigate core excited dynamics in a solid, and show that excitons –a quasiparticle made of one electron and one hole bound by an attractive potential –can play the same role as atomic resonances. Attosecond transient reflectivity measurements are performed on single crystal Magnesium Oxide (MgO), a wide band gap insulator, known for its strong excitonic effects [166]. First, an XUV attosecond pulse excites electrons from the Mg 2p core states into the conduction band. Due to poor screening by the surrounding electrons, the excited electron is still strongly attracted to the resulting core hole, resulting in a series of discrete excitonic peaks. Due to the broad band nature of the attosecond pulse, multiple excitonic states are populated. Then, a strong 4 fs near-infrared laser pulse couples the excitonic states, resulting

in strong lineshape modifications in the time domain. This experiment, together with theoretical simulations, suggests that these features are due to an 800 nm laser induced coherence between different excitonic states, and that the reflectivity lineshape can be continuously controlled by tuning the laser field strength.

5.1.1 Excitons in solids

As discussed in Chapter 1, when a photon with sufficient energy interacts with a solid, it can initiate an electronic transition, leading to the creation of an excited electronic state. The resulting excited electronic state can, under some conditions lead to the formation of an exciton, which is an electrically neutral, quasi bound electron-hole pair stabilized by the Coulomb interaction between the electron and the remaining localized hole [167]. The exciton is a quasi-particle, a fictitious entity created by the many body interaction between the excited electron and its environment. Consequently, excitons are not eigenstates of any Hamiltonian, and they have finite lifetimes [168]. The electron-hole system is in many cases spherically symmetric, and it is thus directly analogous to a hydrogen atom- consequently in some cases, the excitonic states are hydrogenic, and their energy can be approximated by [169]:

$$E = E_g - E_{ex}/n^2 = E_g - \frac{e^2}{\varepsilon r n^2} \tag{5.1}$$

where E_g is the energy of the electronic transition in the absence of the exciton, E_{ex} is the exciton binding energy, n is the principle quantum number of the exciton e is the electron charge, ε is the dielectric constant of the medium, and r is the exciton radius. Because E_x is in general a positive quantity, the energy given in equation 5.1 is less than E_g, reflecting the fact that the electron-hole Coulomb interaction provides stabilization. Consequently, in absorption spectra, excitons manifest as a series of peaks within the band gap, converging toward the conduction band [170]. These principles are illustrated in Figure 31. The above treatment is only valid for strong screening of the electron-hole Coulomb interaction, which is typically the case in inorganic semiconductors.
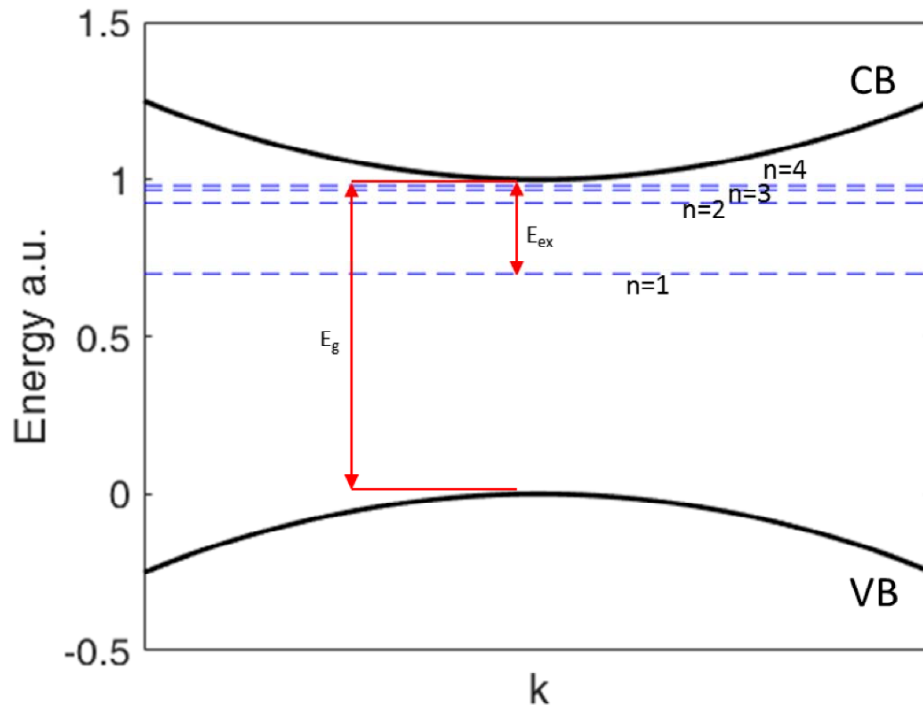
Figure 31: Schematic representation of exciton states within a semiconductor: Excitation from the valence band (VB) to the conduction band (CB) occurs at the band gap energy (E_g). The n=1, n=2, n=3, and n=4, states of an exciton manifest as a series of states converging toward the conduction band. The energy difference between the n=1 state and E_g is the binding energy of the exciton, E_x.

Because the formation of an exciton involves polarization of the medium, the exciton binding energy in equation 5.1 explicitly depends on the dielectric function of the material. Consequently, the degree of polarizability of the medium has a profound influence on the behavior and properties of the excitons created. In materials with high polarizability (large dielectric constant), such as inorganic semiconductors, Wannier-Mott excitons are created [171]. Because of the highly effective charge screening in these materials, Wannier-Mott excitons are characterized by low binding energy, often on the order of a few tens of meV and a large spatial extent often on the order of 10 nm. By contrast, in materials with low polarizability (small dielectric constant), such as organic semiconductors, or insulators, Frenkel excitons are created [172]. Frenkel excitons are characterized by large binding energies on the order of 1 eV and small spatial extents on the order of 1 nm, and they require a different theoretical treatment from the one in 5.1. [173]

In the XUV and x-ray regime, electronic transitions occur from core levels into the conduction band, and accordingly, the excitons produced under these circumstances are very different. They are more characteristic of Frenkel excitons in that their binding energy is quite

high. Previous work has shown that the optical properties of some core excitons can be recreated using the so called Z+1 approximation, in which the atom on which the excitation occurs is replaced by an atom with an additional proton, and optical properties are then calculated for this new "impurity model" with other standard methodologies. [174,175]

5.1.2 Strong lattice coupling to core excitons in MgO

Core excitons are known to couple to phonons in many materials, resulting in a drastic modification of the exciton properties. The coupling of a core exciton to an optically active phonon has been treated theoretically by Mahan. [176] By assuming that the excited electronic state couples to a single phonon mode Mahan derives a time dependent dipole of the form:

$$d(t) = e^{-i\omega_{ex}t - t\gamma - \varphi(t)} \tag{5.2}$$

where ω_{ex} is the excitation frequency of the electronic transition, γ is the lifetime of the excitation, and $\varphi(t)$ is the phase induced by coupling to the phonon mode, which is given by:

$$\varphi(t) = \left(\frac{M_0}{\omega_0}\right)^2 [(2N+1)(1 - \cos \omega_0 t) - i(\omega_0 t - \sin \omega_0 t)] \tag{5.3}$$

Here M_0 is a coupling constant, N is the population of the phonon mode, and ω_0 is the frequency of the phonon mode. According to equations 5.2 and 5.3, coupling of the excited state to vibrations in the lattice results in a complex phase shift of the associated time dependent dipole, reducing the lifetime and in turn modifying the absorption lineshape from a simple lorentzian (in the absence of coupling), to a broadened form which roughly resembles a Gaussian. From this model, the absorption spectrum can be computed as:

$$S(\omega) \propto -\omega Im[\tilde{d}(\omega)] \tag{5.4}$$

where $\tilde{d}(\omega)$ is the Fourier transform of equation 5.2. The effect of phonon coupling on an absorption lineshape is given in Figure 32, which shows calculated absorption profiles for the zero coupling ($M_0 = 0$) case, and strong coupling ($M_0 = 1$) case.

Magnesium oxide (MgO), is widely known to have strong excitonic effects at the Mg $L_{2,3}$ edge (transitions from the 2p core to conduction band). These effects have been previously
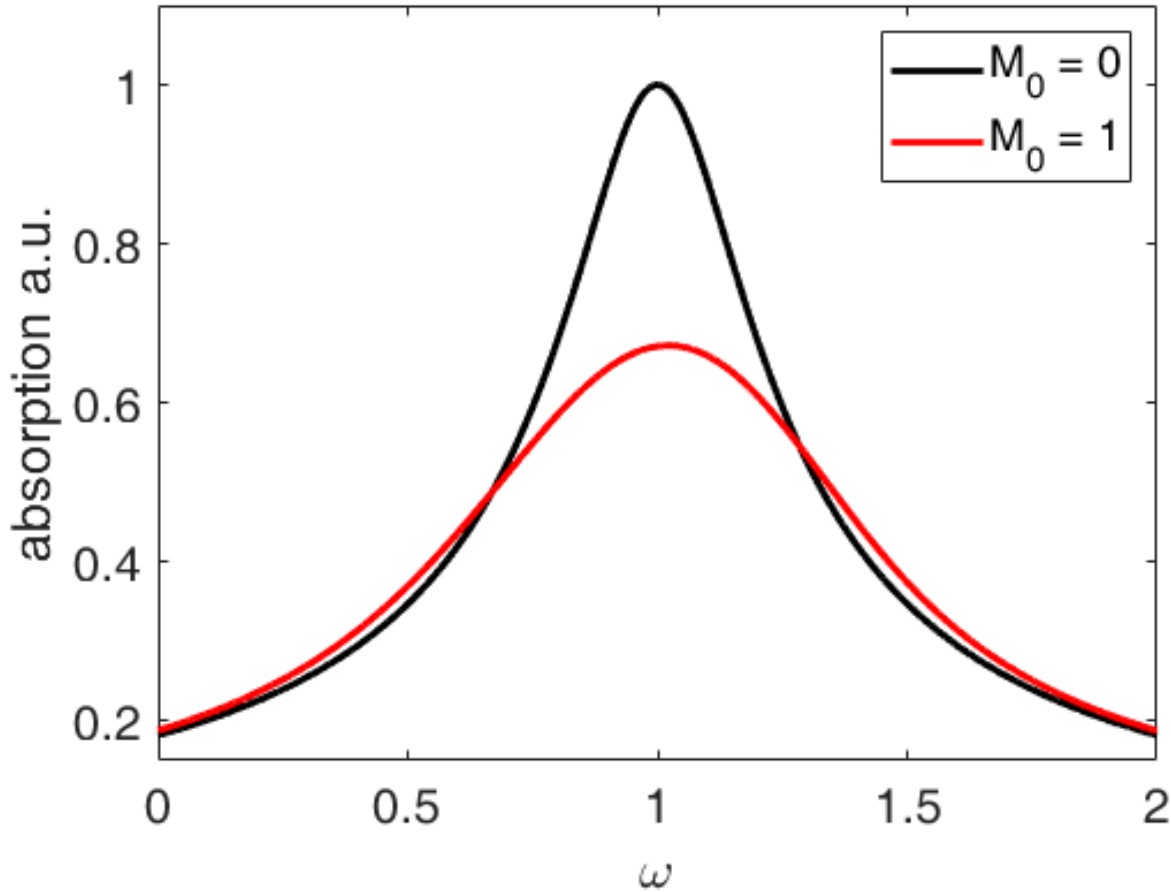
Figure 32: Impact of phonon coupling on absorption lineshape. Black, Lorentzian absorption lineshape calculated from equation 5.2 with no phonon coupling ($M_0 = 0$). Red, broadened absorption lineshape resulting from phonon coupling to dipole, as described by equation 5.2. For phonon coupling, the parameters ω_0, N,γ, and ω_{ex} were 0.06, 0.109, 0.37, and 1 respectively.

observed in electronic structure calculations, which show that excitonic effects must be included in order to properly account for the experimentally observed band structure. [175] Additionally, excitonic effects have been observed in x-ray absorption measurements [177], and by the presence of sharp peaks in x-ray reflection measurements [178,179]. Excitons at the Mg $L_{2,3}$ edge are known to couple very strongly to an LO phonon ($\omega_0 = 0.06$ eV), resulting in substantial broadening of the absorption lineshape, and a reduction of the lifetime of the $L_{2,3}$ excitation. [179,180]

5.2 Experimental

The experimental setup is described in previous chapters. A carrier envelope phase stabilized Ti:Sapphire laser is spectrally broadened with a neon filled hollow core fiber resulting in a broad band spectrum (500-1000 nm) and 900μJ pulse energy, which is compressed using dielectric chirped mirrors (Ultrafast Innovations). Residual third order dispersion is removed with 2 mm of ammonium dihydrogen phosphate [36], yielding nearly single cycle pulses with duration 3.5 fs, as characterized by dispersion scanning. The majority of the pulse energy (560 μJ) is focused into an Ar containing gas cell for high harmonic generation (HHG), yielding continuous XUV spectra with bandwidth from 30-70 eV. Residual NIR is removed using a 100 nm Al filter, and the transmitted XUV light is focused onto a single crystal MgO wafer (purchased commercially and used without modification). Reflected XUV light is dispersed using an XUV grating and imaged with a CCD, yielding an energy resolved reflection spectrum of the sample, with energy resolution ~50 meV at 50 eV. The remaining NIR (340 μJ) is time delayed and recombined with the XUV light using an annular mirror, with NIR intensity of approximately 10^{12} W/cm^2.
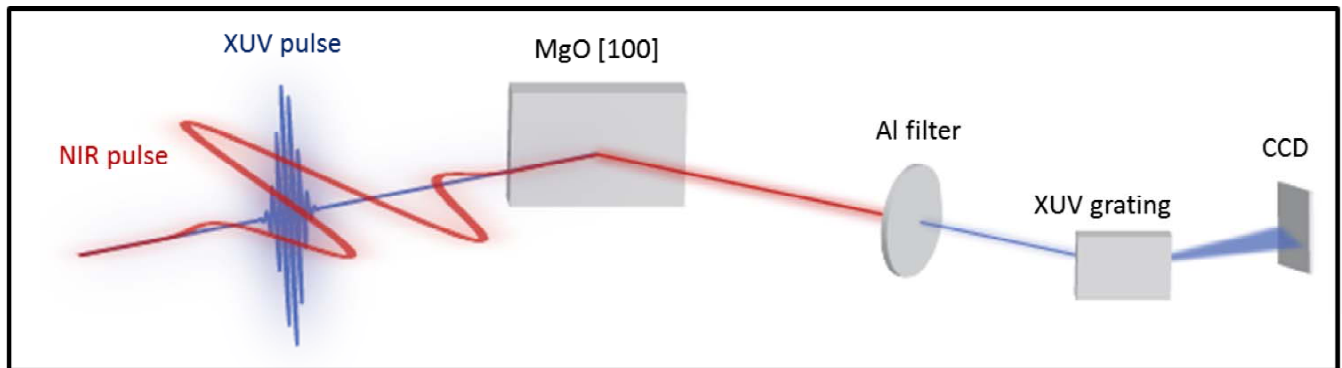
Figure 33: Experimental setup for XUV transient reflectivity of MgO. Angle of incidence 66° from normal, NIR p-polarized, XUV s-polarized.

5.3 Results

5.3.1 Static reflection spectrum

The static reflection spectrum of MgO 100 is shown in Figure 34. The static reflection spectrum shows a series of peaks at 53.4, 57.8, 60.0, and 65.37 eV, which have previously been observed in XUV reflectivity experiments, and assigned to Mg core-level excitons. [179] The first peak (at 53.4 eV), occurs below the conduction band edge, which has previously been measured at 53.72 eV [179], conclusively demonstrating its excitonic character and suggesting
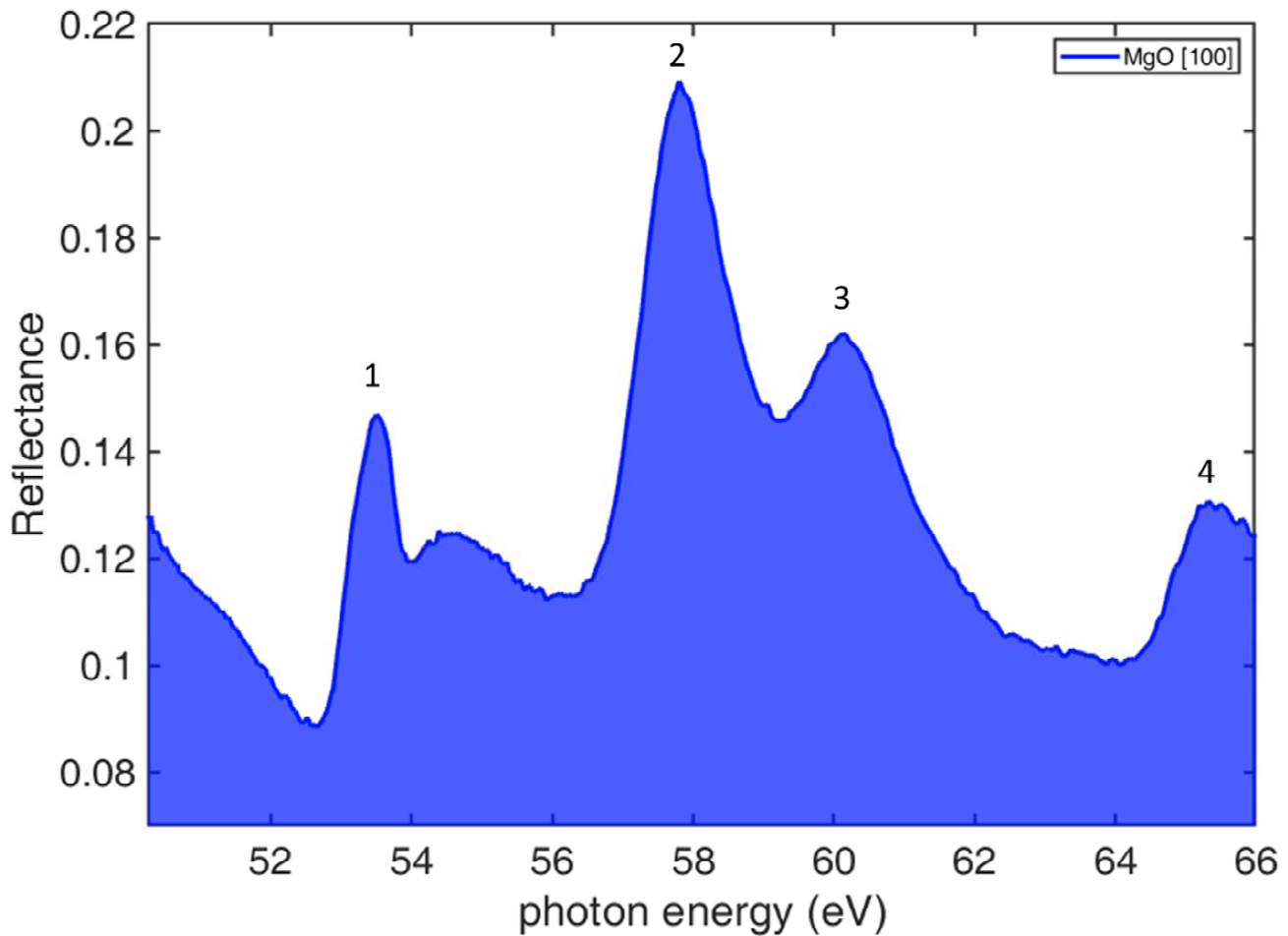
Figure 34 Static Reflection spectrum of MgO [100] for s polarized XUV radiation at 66° angle of incidence with respect to the surface normal. Sharp peaks present at 53.4, 57.8, 60.0, and 65.37 eV are consistent with previously observed core excitons.

an approximate binding energy of 0.32 eV. This value is much larger than those found in valence excitons, and it is consistent with values for other core excitons in solids [181].

5.3.2 Recovery of the complex valued refractive index

In order to more carefully analyze electronic transitions underlying the static reflection spectrum in Figure 34, we employ modified Kramers-Kronig analysis to convert the static reflection spectrum into the complex valued refractive index. Because the optical properties of dispersion, refraction, reflection, and absorption all depend on the complex susceptibility function, they are not independent, and in principle, complete knowledge of one of these observables allows retrieval of the others. This is because the complex valued susceptibility function $\chi(\omega) = \chi_1(\omega) + i\chi_2(\omega)$ itself is analytic. Consequently for suitably defined $\chi(\omega)$ the real and imaginary parts are linked as follows: [182]

$$\chi_1(\omega) = \frac{1}{\pi}\mathcal{P}\int_{-\infty}^{\infty}d\omega'\frac{\chi_2(\omega')}{\omega' - \omega} \qquad \chi_2(\omega) = -\frac{1}{\pi}\mathcal{P}\int_{-\infty}^{\infty}d\omega'\frac{\chi_1(\omega')}{\omega' - \omega} \qquad \textbf{(5.5)}$$

Where $\mathcal{P}$ denotes the principal part of the integral. The equations in **5.5** are known as the Kramers-Kronig relations, and they directly imply a large set of related equations which are widely applied in diverse fields such as electron energy loss spectroscopy [183], optics, [184] and signal processing. [185] One such equation often employed in the analysis of reflectivity data allows recovery of the complex reflection phase, given the reflected intensity:

$$\theta(\omega) = \frac{1}{\pi}\int_0^{\infty}d\omega'ln\left|\frac{\omega' + \omega}{\omega' - \omega}\right|\frac{d}{d\omega'}ln\left(\sqrt{R(\omega')}\right) \qquad \textbf{(5.6)}$$

where $R(\omega)$ is the reflected intensity and $\theta(\omega)$ is the phase of reflected light [186]. Evaluation of equation 5.6 requires complete knowledge of $R(\omega)$ over $\omega \in [0,\infty)$ which in practice is of course impossible. To evaluate equation 5.5, the experimentally measured reflectivity (Figure 34) is padded with previously measured reference data [187], as shown below in Figure 35a. Padding the experimentally measured reflectivity data (red) with reference data mitigates the error that comes from applying equation 5.6 to a finite energy range [93]. Because equation 5.6 is derived assuming normal incidence, application to non-normal incidence does not give the exact phase, but instead gives a pseudophase (Figure 35b). The problem of recovering the true optical phase from non-normal incidence reflectance data has been solved previously, which
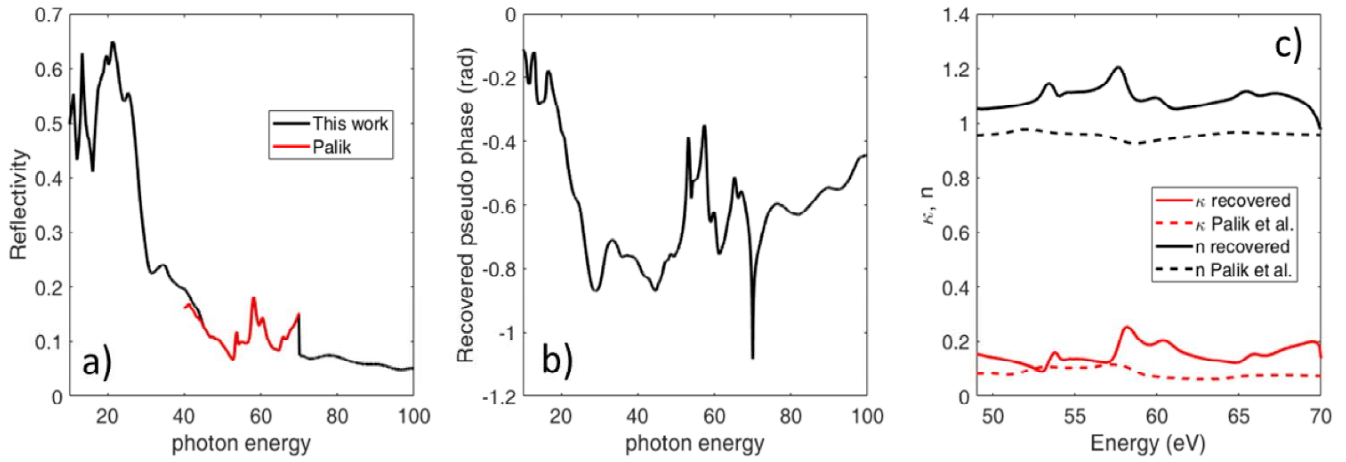
Figure 35: Kramers-Kronig Recovery of complex refractive index from reflection. A) Measured reflectivity (red), padded with reference data (black). B) Pseudo phase obtained from application of 5.5 to the padded data in A). C) Recovered real (solid, black), and imaginary (solid, red), parts of refractive index compared to previously obtained results.

allows the true phase to be recovered from the pseudophase via an analytic correction. [188] Once the true phase, and reflectivity are known, the complex valued refractive index can be obtained by solving the Fresnel equations, yielding the refractive index shown in Figure 35c. The retrieved real (black), and imaginary (red) part of the refractive index show peaks at 53.5, 57.7, 60.2 and 65.4 eV, which matches closely with previously measured values for bulk excitons in MgO, indicating that these features are due to bulk excitons, not surface excitons. [189]

The static refractive index retrieved in Figure 35c contains contributions from bulk excitons, as well as ionization from the valence band, and core level transitions into the continuum conduction band states. [179] To isolate and extract the excitonic contribution to the optical properties, the static absorption spectrum was computed using equation 1.9 and background subtracted with a procedure described elsewhere. [179] The static absorption spectrum obtained is shown in Figure 36.(black). The contribution from ionization out of the valence band (blue, dashed line) was obtained by fitting the pre edge absorption spectrum to the form $(E - E_{VB})^{-a}$, where E_{vb} is the valence band edge (45.95 eV) taken from [179]. The contribution from transitions into conduction band states (yellow, dashed lined) was obtained by fitting the post edge spectrum to the form $(E - E_{CB})^b$, where E_{CB} is the conduction band energy (53.72 eV), taken from [179]. The contribution from transitions into higher lying conduction band states far away from the band edge (green dashed) was obtained by fitting the background between 58 and 65 eV to a broadened linear function. After subtracting these contributions, the

red dashed spectrum shows clear isolated peaks which allow determination of exciton linewidths and positions clearly.
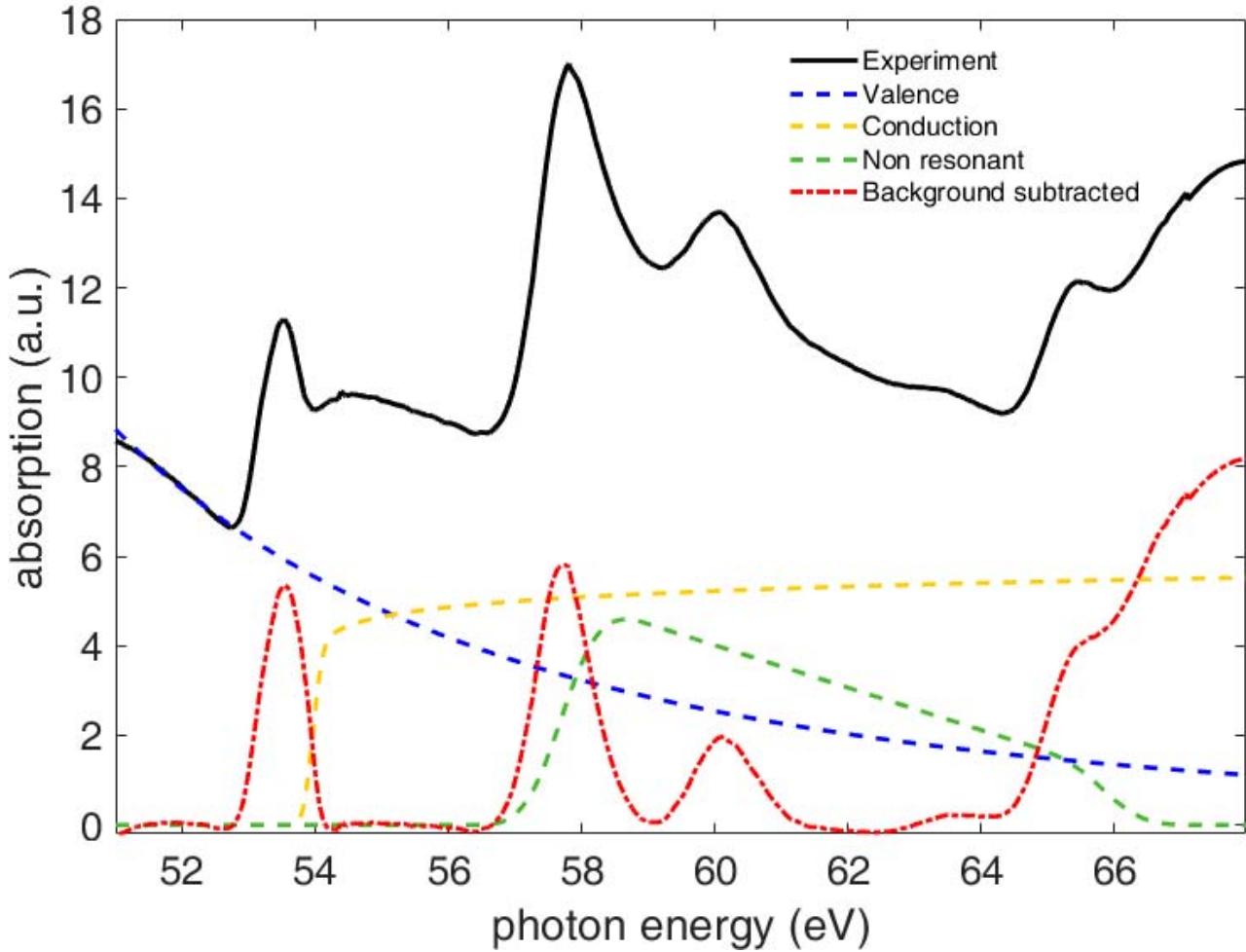
Figure 36: Decomposition of MgO absorption spectrum. (Black, solid) absorption spectrum computed from refractive index obtained by Kramers-Kronig analysis. (Blue, dashed) contribution from valence band ionization. (Yellow, dashed) contribution from transition into conduction band.(Green, dashed) contribution from transitions into higher lying conduction bands far from edge. (Red, dashed) Background subtracted absorption showing remaining contributions due to exciton features.

The resulting exciton linewidths, positions and assignments are shown in table 3.

Table 3: Recovered exciton parameters and assignment

Exciton	Energy (eV)	Width (FWHM, eV)	Assignment
1	53.52	0.20	Mg 3s (bulk)
2	57.74	0.28	Mg 3s/3d (bulk)
3	60.16	0.31	Mg 3s/3d (bulk)
4	65.38	0.24	Mg 3s/3d (bulk)

5.3.3 Transient reflectance of MgO

The experimentally measured transient reflectance (described in section 5.2) is shown in Figure 37a. The recorded $\Delta R/R$ shows complex lineshape modification at negative time delay (XUV first) which persists for less than 10 fs. The lineshape modifications (shown in Figure 37b)
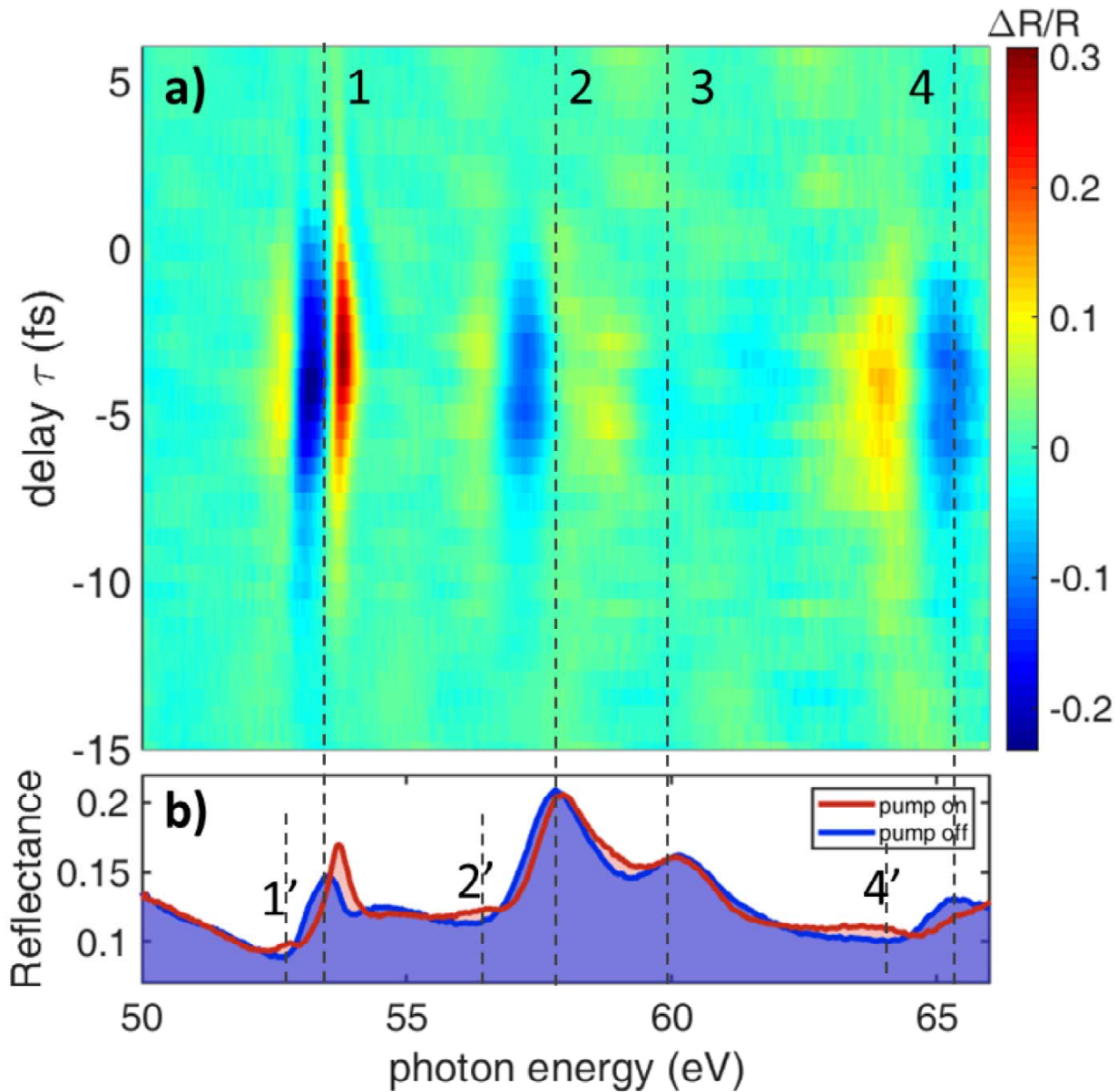
Figure 37 Transient reflectance of MgO [100] measured at 66° angle of incidence, NIR p-polarized, XUV s-polarized. B) Lineshape modifications during pump probe overlap change static reflectance (blue), yielding pump on spectra (red).

are characterized by a sharpening and blueshift of peaks 1,2 and 4, as well as the creation of new peaks 1', 2' and 4'.

The observed transient reflectivity in MgO is qualitatively different from what was observed in germanium (see chapters 3 and 4), suggesting that the dynamics observed have different underlying physical mechanisms. While the transient signals in germanium occur after time zero (NIR first), and persist for >10 ps, in MgO the transient modification occurs before time zero and lasts for less than 10 fs. This qualitative difference can be explained by contrasting the substantially different electronic structures of germanium and MgO. Germanium is a semiconductor (E_{gap} = 0.8 eV), and thus carrier excitation dominates the optical response, leading to long-lived reflectivity changes after time zero, which only decays due to recombination of the excited carriers. In contrast, MgO is an insulator (E_{gap} = 7.8 eV), and thus carrier excitation (which requires a 6 photon transition) is highly unlikely for 800 nm light. Consequently, the experiment in MgO allows selective observation of the NIR induced modification of the XUV reflection in the absence of carrier excitation.

Transient modification of the XUV susceptibility in systems for which valence transitions are high energy has been long studied in gas phase systems such as Helium [165], Argon [13] and more recently in the solid state system SiO_2. [190] In these studies, modification of the XUV absorption spectrum is explained as a complex phase shift applied by the NIR laser to the XUV induced polarization in the material. This laser induced phase shift can come about from a number of underlying physical mechanisms, but typically involves coupling the XUV excited dipole to either a continuum of states [191] or a set of discrete of states through various coupling schemes [192]. Because of the wide band gap within MgO, there can be no states below peak 1, thus the most likely coupling scheme in this system is coupling of peak 1 and 2 via an intermediate dark state (so called ladder coupling). The complex phase shift in the time domain then results in a modification of the XUV susceptibility in the frequency domain, which modifies observables such as absorption and reflection. In these systems the complex phase shift of the XUV dipole results in modification of the XUV lineshape before time zero, similar to the reflectivity changes observed in MgO, indicating that the observed reflectivity changes are due to

a similar mechanism. Interestingly, in these studies the lifetime of the XUV polarization can be estimated by the duration of lineshape modifications.

In order the estimate the lifetimes of the XUV polarization, the dynamics of the lineshape modifications are tracked by taking lineouts along the transient features. Lineouts taken at 64.15, 57.2 and 53.7 eV, corresponding to the maximum change along features 4,2 and 1 are shown as red points in Figure 38a, b and c respectively. The lineouts were fit with a convolution of a step function, a Gaussian with 3.5 fs duration and an exponential (black line), yielding estimated lifetimes of 5.4, 1.7 and 1.6 fs for excitons 4, 2 and 1 respectively. Based on the linewidths of the states, the lifetimes can be estimated as $\frac{\hbar}{\Delta E} = 2.7$ fs, 2.3 fs, and 3.2 fs, respectively, where ΔE is the linewidth of the state. The discrepancy between lifetimes obtained from linewidths and those measured directly in the time domain is a direct result of the strong coupling of the electronically excited state to the lattice [179,193], and highlights the need for a direct time domain observation of XUV polarization dynamics in MgO.
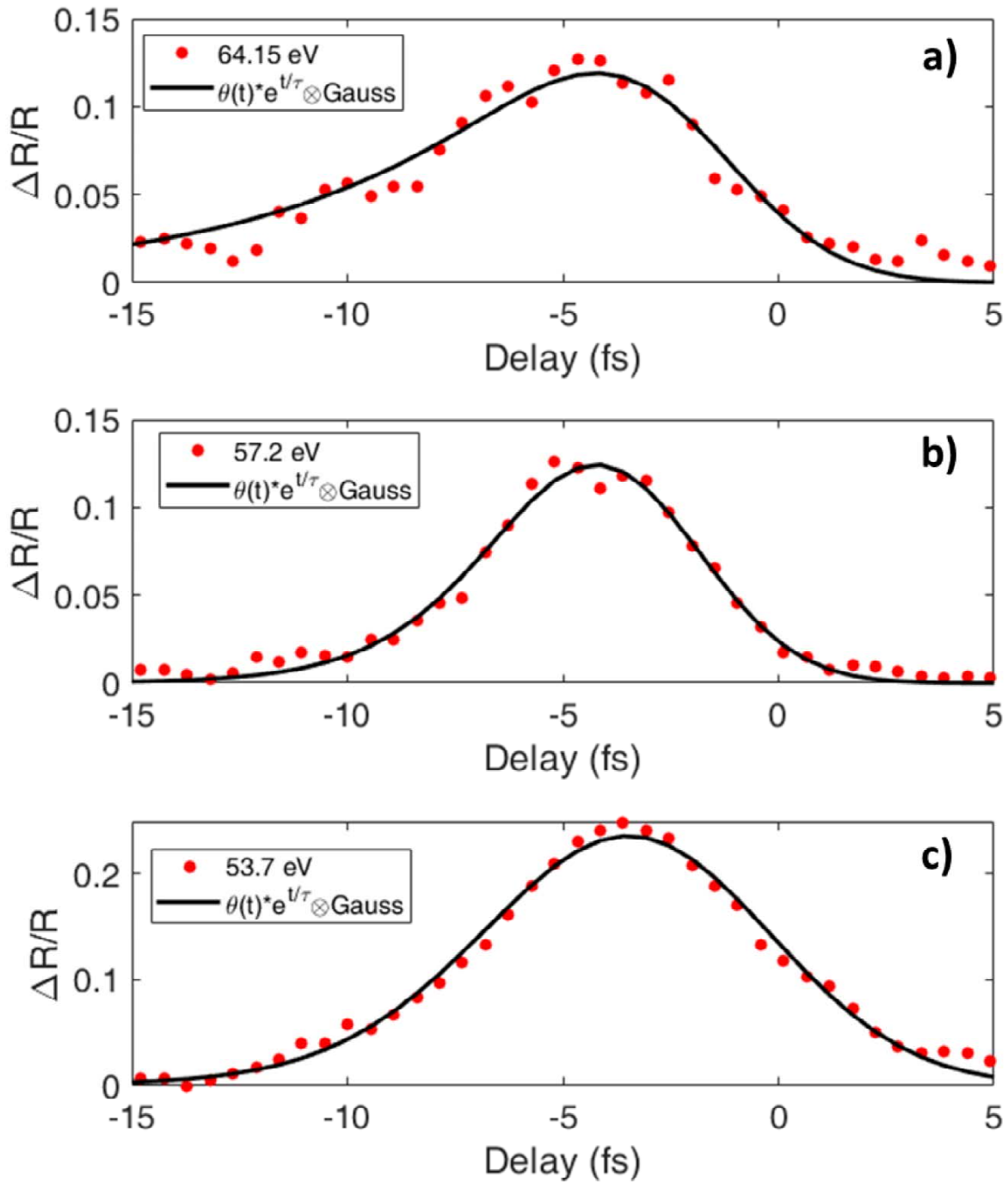
Figure 38: Lineouts along transient exciton features. A) Red, lineout along 53.7 eV, Black, convolution of step function, Gaussian with 3.5 fs duration and exponential with 1.6 fs duration. B) Red, lineout along 57.2 eV, Black, convolution of step function, Gaussian with 3.5 fs duration and exponential with 1.7 fs duration. C) Red, lineout along 64.15 eV, Black, convolution of step function, Gaussian with 3.5 fs duration and exponential with 5.4 fs duration.

5.3.4 Power Dependence

To more thoroughly investigate the transient features observed in reflectivity, we investigated the power dependence of the dynamics observed in reflectivity. As pump fluence is modified from 13.8 mJ/cm^2 to 24.8 mJ/cm^2 Figure 39, the underlying dynamics are basically unchanged, and still characterized by transient modification of the exciton lineshapes over the course of the pulse duration.
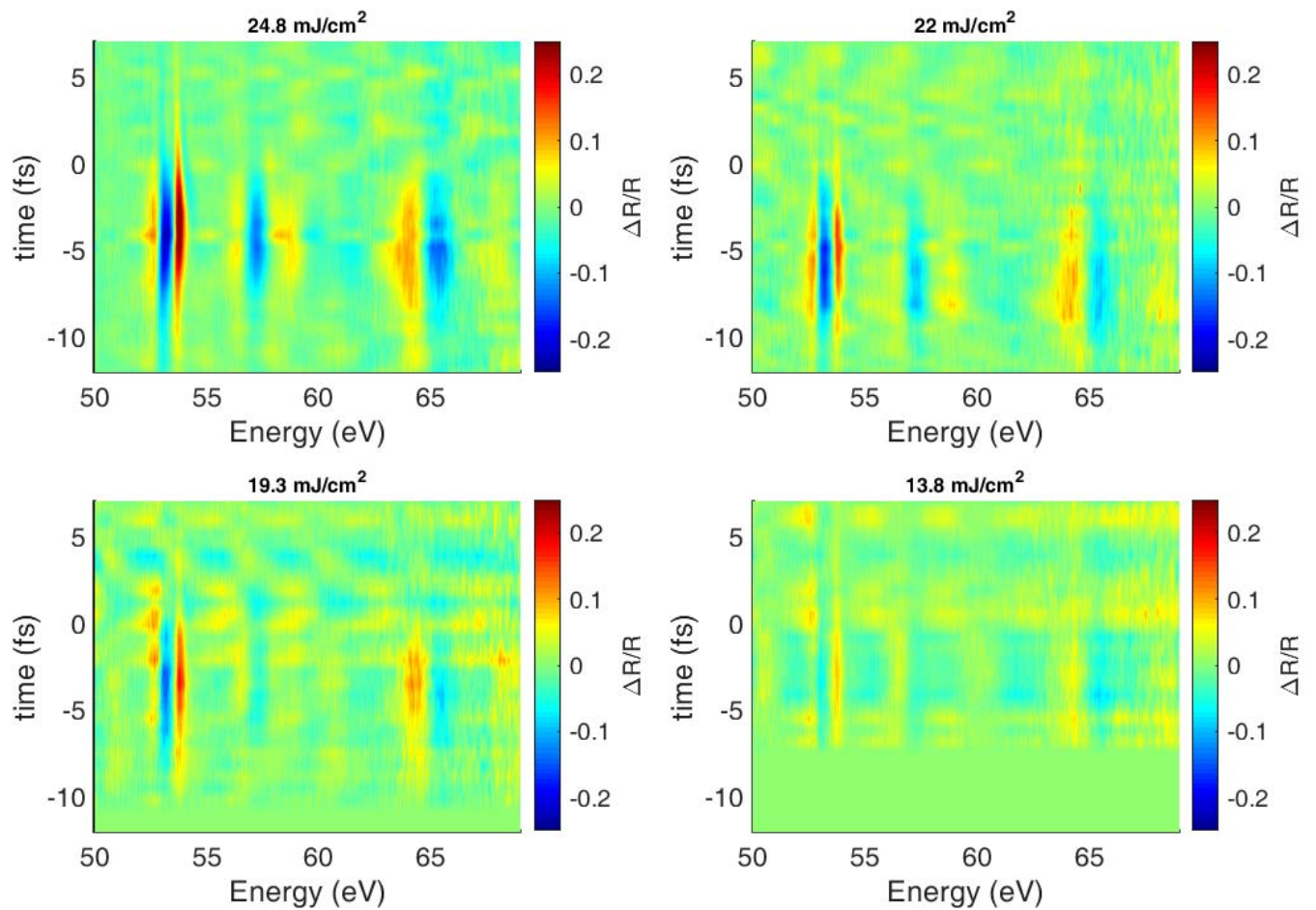
Figure 39: Power dependence of transient reflectivity in MgO. $\Delta R/R$ for 24.8 mJ/cm^2, 22 mJ/cm^2, 19.3 mJ/cm^2 and 13.8 mJ/cm^2.

The clear trends in lineshape modification are illustrated by taking lineouts of the transient reflectivity at -5 fs (Figure 40). This time was chosen as it corresponds to the time of maximal lineshape modification. The lineouts reveal that as pump fluence is varied from 13.8 mJ/cm^2
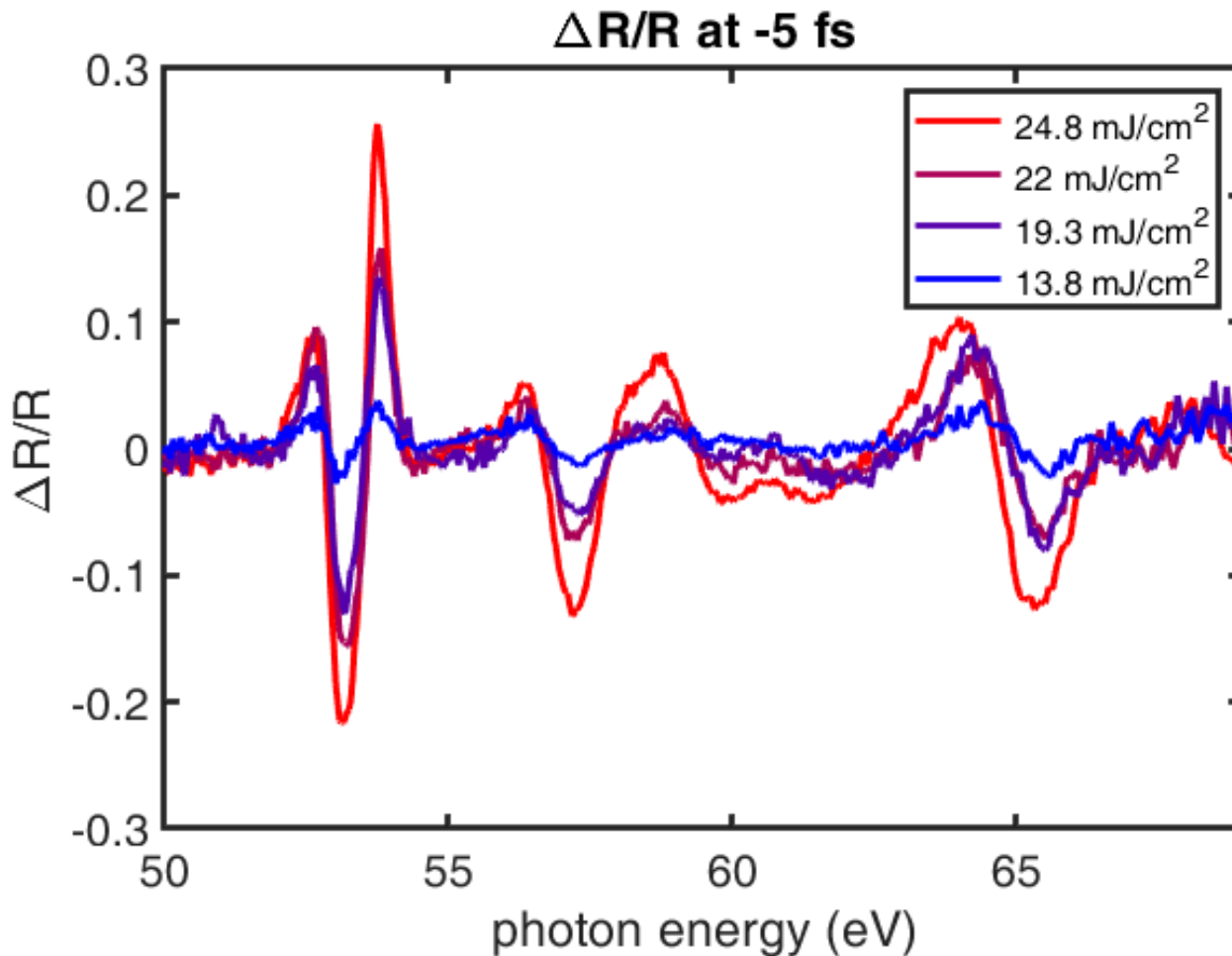
Figure 40: Fluence dependence of transient reflectivity at – 5 fs. Lineshape modifications can be continuously tuned as pump fluence is increased from 13.8 mJ/cm^2 (blue) to 24.8 mJ/cm^2 (red).

(blue) to 24.8 mJ/cm^2 (red), the lineshape modification can be continuously tuned. Interestingly, the feature at 53.5 eV is substantially more sensitive to pump fluence than the other features present, indicating that Exciton 1 may be more polarizable than excitons 2, 3 and 4.

5.4. Discussion

5.4.1 Multi level model simulation of dynamics

The polarization lifetimes obtained from the lineouts in Figure 38 are rough estimates and generally speaking, extraction of polarization lifetimes from lineshape modification requires simulation of the relevant dynamics [194–196]. To recreate the dynamics in Figure 37a, consider a multilevel model which assumes the presence of 4 states: a ground state $|1\rangle$ and 2 bright states ($|2\rangle$ and $|4\rangle$) which can be populated by the XUV field. The energies of $|2\rangle$ and $|4\rangle$ are fixed at 53.5 and 57.8 eV with respect to the ground state, mimicking the energies of excitons 1 and 2 observed in the static spectrum. The role of the NIR is to couple $|2\rangle$ and $|4\rangle$ via an intermediate state $|3\rangle$ which is optically dark with respect to the ground state.
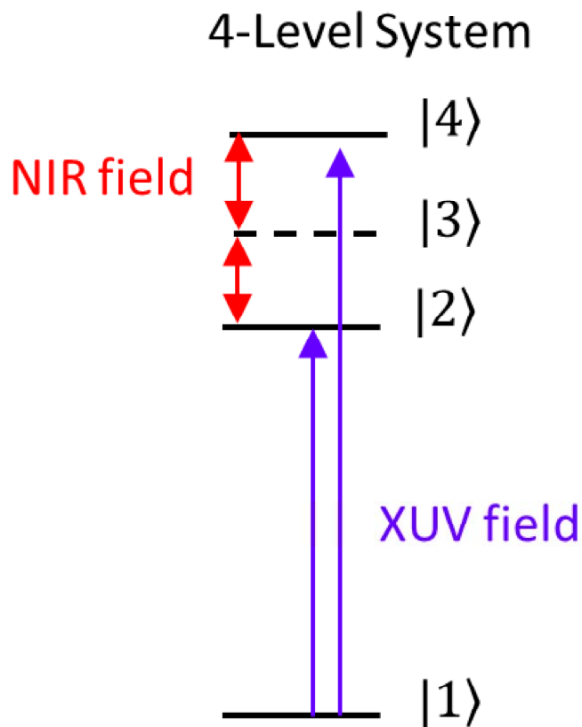
Figure 41: Schematic view of multi-level model used in simulating dynamics.

Using time dependent perturbation theory, the dipole moment of the system can be expressed as:

$$d(t) = \langle \Psi(t)|\hat{d}|\Psi(t)\rangle e^{-\frac{\Gamma t}{2\hbar} - \varphi(t)}$$

<div align="right">(5.7)</div>

Where $\hat{d}$ is the transition dipole operator, $\Psi(t)$ is the time dependent wave function of the system, Γ is the Auger lifetime of the excited state, and $\varphi(t)$ is the phonon induced phase described in equation 5.3. In principle equation 5.7 allows computation of the time dependent absorption spectrum, where the time dependence is induced by the action of the NIR field on $\Psi(t)$. In this model, the XUV field creates a coherent superposition of $|1\rangle$, $|2\rangle$ and $|4\rangle$, which then experiences phase shifts due to NIR induced latter coupling of $|2\rangle$ and $|4\rangle$ mediated through the dark state $|3\rangle$. Expanding (**5.7**) gives

$$d(t) \propto [c_1^* c_2 d_{12} e^{-i\omega_{12}t - \varphi_2(t)} + c_1^* c_4 d_{14} e^{-i\omega_{14}t - \varphi_4(t)}$$
$$+ c_2^* c_3 d_{23} e^{-i\omega_{23}t - \varphi_2(t)} c_3^* c_4 d_{34} e^{-i\omega_{23}t - \varphi_4(t)}] e^{-\frac{\Gamma}{2\hbar}t}$$

<div align="right">(5.8)</div>

where ω_{ij} is the energy difference and d_{ij} is the transition dipole matrix element between states i
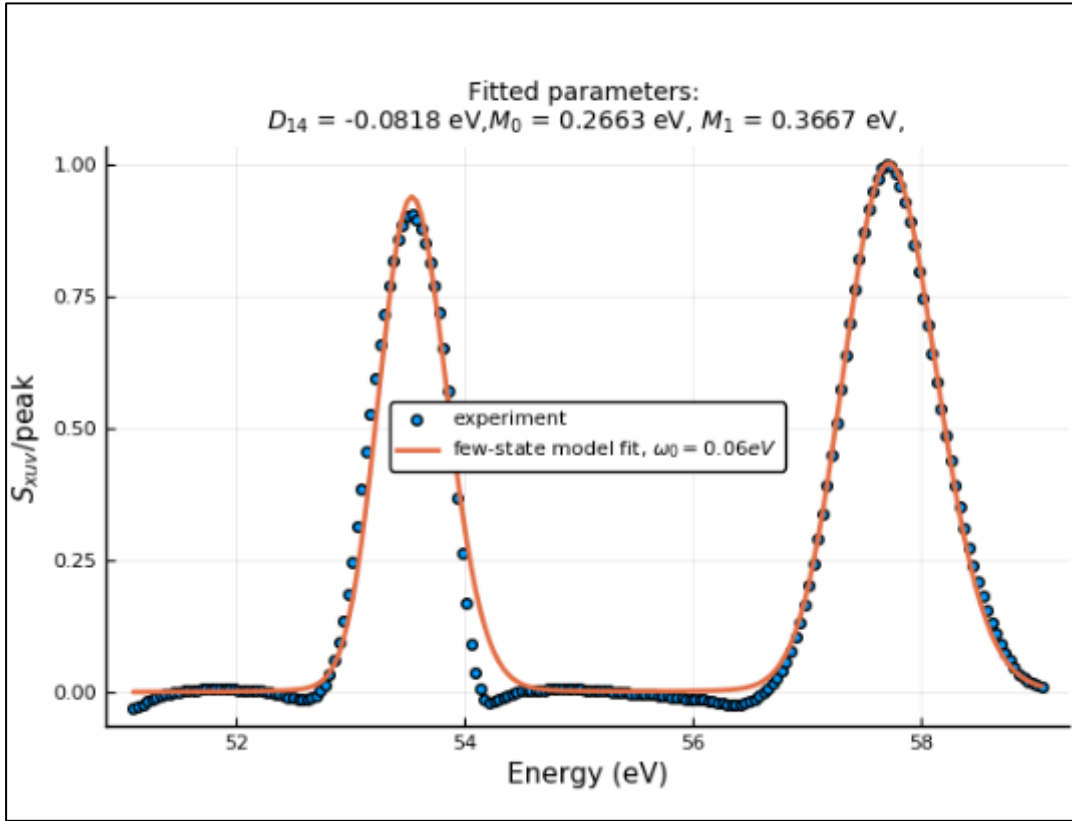
Figure 42: XUV only absorption spectrum (blue points) and fit to few-state model (orange curve). Parameters obtained from fit: $\boldsymbol{\omega_{12}}$ = 53.57 eV, $\boldsymbol{\omega_{14}}$ = 57.76 eV, $\boldsymbol{\omega_0}$ = 0.06 eV, M_1 = 0.266 eV, M_4 = 0.367 eV, d_{12} = 0.05, d_{14} = -0.0818.

and j respectively, c_i is a time dependent coefficient which accounts for the non-trivial time evolution of $\Psi(t)$ due to laser induced phase, and $\varphi_i(t)$ is the phase due to coupling of state i to the lattice, as given by equation 5.3.

 Application of the above model to the transient behavior observed requires first fitting the static XUV absorption spectrum, (red curve Figure 36) to equation 5.8. For the XUV -only case, all c_i are time independent, and only d_{12} and d_{14} terms contribute. The background subtracted static absorption and fit obtained are shown in Figure 42. From the fit, the energies of the excitons are obtained as $\omega_{12} = 53.57$ eV, $\omega_{14} = 57.76$ eV, in good agreement with the peak positions in Figure 36, and in good agreement with previous work. [179] Using the model for the ground state XUV dipole parameterized by these values, excited state absorption values can then be calculated using (5.8). The experimental absorption spectrum during pump-probe at -5 fs
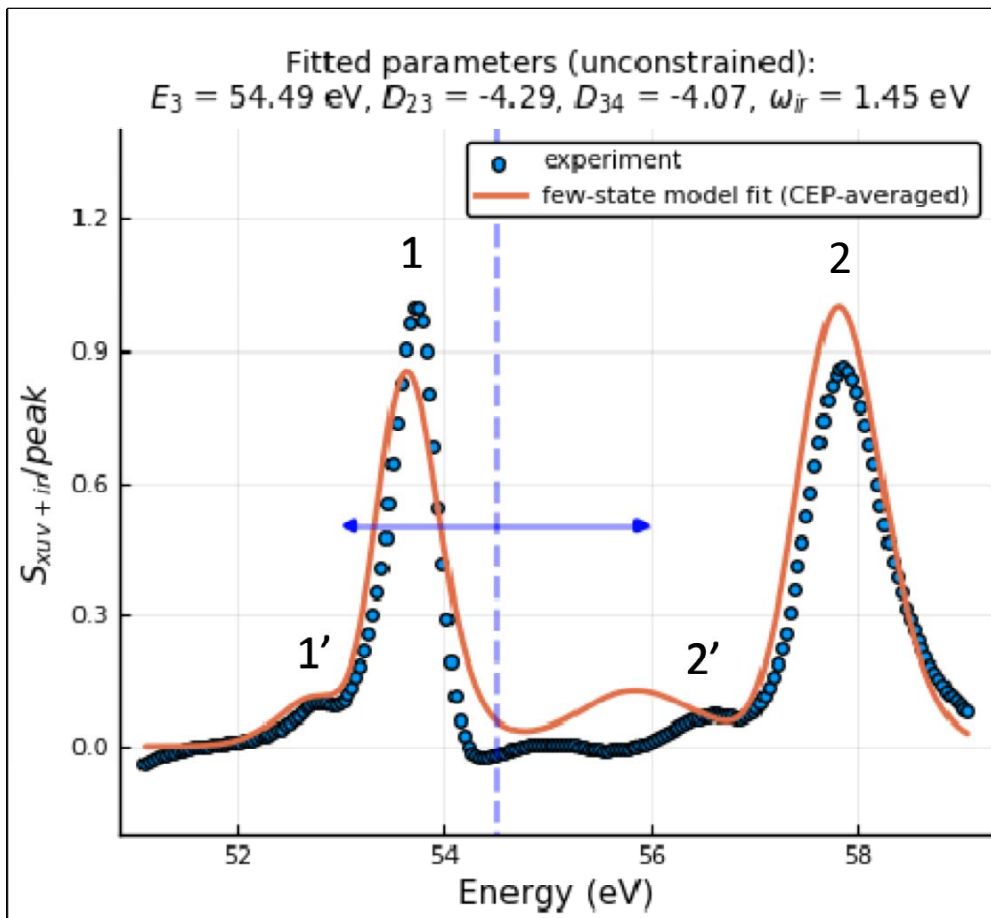

Figure 43: XUV + IR absorption (blue points), and fit to few-state model (orange curve). Blue dashed line indicates the position of the dark state. Data and simulation correspond to -5 fs delay.

time delay, and the resulting fit are shown in Figure 43. The resulting fit qualitatively captures the major dynamics induced by the NIR pulse. The blueshift of peaks 1 and 2 shown in Figure 37b as well as the emergence of peaks 1' and 2' are reasonably captured by the model, indicating that the 4-level model is a reasonable physical description of the system. Interestingly, 1' and 2' are spaced by $\hbar\omega_{NIR}$ from state $|3\rangle$, suggesting that they are actually light induced states(dressed states resulting from the photon dressing of the field free electronic structure), similar to those that have been observed in attosecond studies in helium [191,197]. Further analysis to determine this is ongoing.

The reasonable qualitative agreement between the model and experiment reveals that the experimentally measured transient reflectivity can be described as a NIR induced perturbation of the XUV induced dipole in MgO it and allows us to build the following physical picture: First, the XUV pulse coherently populates core excited excitonic states. Subsequently, these states are then coupled via the NIR field, leading to phase shifts of the associated dipoles, and the transient features observed, as well as the creation of light induced states 1' and 2'. Finally, coherence is lost as the core excited states couple to the lattice, leading to the rapid dephasing of the dipoles within <4 fs, and the extremely rapid dynamics observed in this work. Extraction of the underlying dynamics will require more quantitative fit of the simulations to experiment. This work is ongoing.

5.5 Conclusion

In this work, we use XUV transient reflectivity to provide a time domain observation of excitonic coherence in MgO. This work allows direct measurement of coherence lifetimes and describes the associated dynamics in terms of a simple, physically intuitive few level model. Although coherent coupling of XUV core excited states has been observed in the past [192,195], this work represents one of the first demonstrations of these dynamics in a solid. Accordingly, this work indicates that the few-level formalism that has been so successfully applied in the gas phase, also has relevance to solid state dynamics. This work paves the way for a deeper understanding of polarization dynamics in solids, and provides a convenient mechanism for ultrafast XUV pulse shaping, by tuning the reflectivity of an XUV mirror with a NIR field.

References

[1] S. R. Leone, C. W. McCurdy, J. Burgdörfer, L. S. Cederbaum, Z. Chang, N. Dudovich, J. Feist, C. H. Greene, M. Ivanov, R. Kienberger, U. Keller, M. F. Kling, Z.-H. Loh, T. Pfeifer, A. N. Pfeiffer, R. Santra, K. Schafer, A. Stolow, U. Thumm, and M. J. J. Vrakking, Nat. Photonics **8**, 162 (2014).

[2] W. Ashcroft, N and N. D. Mermin, *Solid State Physics* (2014).

[3] F. Krausz and M. Ivanov, Rev. Mod. Phys. **81**, 163 (2009).

[4] G. D. Dickenson, M. L. Niu, E. J. Salumbides, J. Komasa, K. S. E. Eikema, K. Pachucki, and W. Ubachs, Phys. Rev. Lett. **110**, (2013).

[5] A. H. Zewail, Nobel Prize 1 (1999).

[6] A. H. Zewail, Science **242**, 1645 (1988).

[7] T. S. Rose, M. J. Rosker, and A. H. Zewail, J. Chem. Phys. **88**, 6672 (1988).

[8] P. M. Paul, E. S. Toma, P. Breger, G. Mullot, F. Augé, P. Balcou, H. G. Muller, and P. Agostini, Science **292**, 1689 (2001).

[9] M. Hentschel, R. Kienberger, C. Spielmann, G. A. Reider, N. Milosevic, T. Brabec, P. Corkum, U. Heinzmann, M. Drescher, and F. Krausz, Nature **414**, 509 (2001).

[10] P. B. Corkum and Z. Chang, Opt. Photonics News **19**, 24 (2008).

[11] M. F. Jager, C. Ott, P. M. Kraus, C. J. Kaplan, W. Pouse, R. E. Marvel, R. F. Haglund, D. M. Neumark, and S. R. Leone, Proc. Natl. Acad. Sci. **114**, 9558 (2017).

[12] M. H. Elkins, H. L. Williams, A. T. Shreve, and D. M. Neumark, Science **342**, 1496 (2013).

[13] W. Cao, E. R. Warrick, A. Fidler, D. M. Neumark, and S. R. Leone, Phys. Rev. A **94**, (2016).

[14] Y. J. Yan and S. Mukamel, Phys. Rev. A **41**, 6485 (1990).

[15] M. Schultze, K. Ramasesha, C. D. Pemmaraju, S. A. Sato, D. Whitmore, A. Gandman, J. S. Prell, L. J. Borja, D. Prendergast, K. Yabana, D. M. Neumark, and S. R. Leone, Science **346**, 1348 (2014).

[16] M. Lucchini, S. A. Sato, A. Ludwig, J. Herrmann, M. Volkov, L. Kasmi, Y. Shinohara, K.

Yabana, L. Gallmann, and U. Keller, Science **353**, 916 (2016).

[17] M. Schultze, E. M. Bothschafter, A. Sommer, S. Holzner, W. Schweinberger, M. Fiess, M. Hofstetter, R. Kienberger, V. Apalkov, V. S. Yakovlev, M. I. Stockman, and F. Krausz, Nature **493**, 75 (2013).

[18] H. Mashiko, Y. Chisuga, I. Katayama, K. Oguri, H. Masuda, J. Takeda, and H. Gotoh, Nat. Commun. **9**, (2018).

[19] H. Mashiko, K. Oguri, T. Yamaguchi, A. Suda, and H. Gotoh, Nat. Phys. **12**, 741 (2016).

[20] R. Huber, F. Tauser, A. Brodschelm, M. Bichler, G. Abstreiter, and A. Leitenstorfer, Nature **414**, 286 (2001).

[21] M. Zürch, H.-T. Chang, L. J. Borja, P. M. Kraus, S. K. Cushing, A. Gandman, C. J. Kaplan, M. H. Oh, J. S. Prell, D. Prendergast, C. D. Pemmaraju, D. M. Neumark, and S. R. Leone, Nat. Commun. **8**, 15734 (2017).

[22] P. C. Becker, H. L. Fragnito, C. H. B. Cruz, R. L. Fork, J. E. Cunningham, J. E. Henry, and C. V. Shank, Phys. Rev. Lett. **61**, 1647 (1988).

[23] M. Bernardi, D. Vigil-Fowler, C. S. Ong, J. B. Neaton, and S. G. Louie, Proc. Natl. Acad. Sci. **112**, 5291 (2015).

[24] A. Othonos, J. Appl. Phys. **83**, 1789 (1998).

[25] J. F. Young and H. M. Van Driel, Phys. Rev. B **26**, 2147 (1982).

[26] A. Othonos, H. M. Van Driel, J. F. Young, and P. J. Kelly, Phys. Rev. B **43**, (1991).

[27] M. Y. Odoi, N. I. Hammer, K. T. Early, K. D. McCarthy, R. Tangirala, T. Emrick, and M. D. Barnes, Nano Lett. **7**, 2769 (2007).

[28] M. J. Kerr and A. Cuevas, J. Appl. Phys. **91**, 2473 (2002).

[29] P. B. Corkum, Phys. Rev. Lett. **71**, 1994 (1993).

[30] M. Lewenstein, P. Balcou, M. Y. Ivanov, A. L'Huillier, and P. B. Corkum, Phys. Rev. A **49**, 2117 (1994).

[31]   S. Ghimire, A. D. Dichiara, E. Sistrunk, P. Agostini, L. F. Dimauro, and D. A. Reis, Nat. Phys. **7**, 138 (2011).

[32]   A. R. Attar, A. Bhattacherjee, C. D. Pemmaraju, K. Schnorr, K. D. Closser, D. Prendergast, and S. R. Leone, Science **356**, 54 (2017).

[33]   F. Quéré, Y. Mairesse, and J. Itatani, in *J. Mod. Opt.* (2005), pp. 339–360.

[34]   G. Sansone, E. Benedetti, F. Calegari, C. Vozzi, L. Avaldi, R. Flammini, L. Poletto, P. Villoresi, C. Altucci, R. Velotta, S. Stagira, S. De Silvestri, and M. Nisoli, Science **314**, 443 (2006).

[35]   Z. Chang, Phys. Rev. A - At. Mol. Opt. Phys. **76**, (2007).

[36]   H. Timmers, M. Sabbar, J. Hellwagner, Y. Kobayashi, D. M. Neumark, and S. R. Leone, Optica **3**, 707 (2016).

[37]   G. Laan, J. Phys. Condens. Matter **3**, 7443 (1991).

[38]   R. Qiao, T. Chin, S. J. Harris, S. Yan, and W. Yang, Curr. Appl. Phys. **13**, 544 (2013).

[39]   C.-M. Jiang, L. Robert Baker, J. Matthew Lucas, J. Vura-Weis, A. Paul Alivisatos, and S. R. Leone, J. Phys. Chem. C **118**, 22774 (2014).

[40]   C. Kittel, *Solid State Physics, 8th Ed.* (2005).

[41]   D. C. Giancoli, *Physics Principles with Applications 6th Edition* (2005).

[42]   R. Bertani, *Solids and Surfaces* (1990).

[43]   A. de Groot, F, Kotani, *Core Level Spectroscopy of Solids (Advances in Condensed Matter Science)* (2008).

[44]   N. H. List, J. Kauczor, T. Saue, H. J. A. Jensen, and P. Norman, J. Chem. Phys. **142**, (2015).

[45]   D. J. Griffiths and C. Inglefield, *Introduction to Electrodynamics*, 4th ed. (Cambridge University Press, 2017).

[46]   M. Wen, I. V Kozhevnikov, and Z. Wang, Opt. Express **23**, 24220 (2015).

[47]   M. C. Troparevsky, A. S. Sabau, A. R. Lupini, and Z. Zhang, Opt. Express **18**, 24715 (2010).

[48]   A. J. Sabbah and D. M. Riffe, Phys. Rev. B - Condens. Matter Mater. Phys. **66**, 1 (2002).

[49]   A. Cirri, J. Husek, S. Biswas, and L. R. Baker, J. Phys. Chem. C **121**, 15861 (2017).

[50]   C. J. Kaplan, P. M. Kraus, A. D. Ross, M. Zürch, S. K. Cushing, M. F. Jager, H.-T. Chang, E. M. Gullikson, D. M. Neumark, and S. R. Leone, Phys. Rev. B **97**, 1 (2018).

[51]   J. Husek, A. Cirri, S. Biswas, and L. Robert Baker, Chem. Sci. **8**, 8170 (2017).

[52]   W. S. M. Werner, K. Glantschnig, and C. Ambrosch-Draxl, J. Phys. Chem. Ref. Data **38**, 1013 (2009).

[53]   M. S. Dresselhaus, Proc. Int. Sch. Phys. 198 (1966).

[54]   Y. R. Shen, Nature **337**, 519 (1989).

[55]   H. Zhang, C.-X. Liu, X.-L. Qi, X. Dai, Z. Fang, and S.-C. Zhang, Nat. Phys. **5**, 438 (2009).

[56]   V. K. Subashiev and A. A. Kukharskii, Phys. Status Solidi (1967).

[57]   I. F. Vakhnenko and V. L. Strizhevskii, Sov. Phys.-Semicond **3**, 1562 (1970).

[58]   H. Timmers, Y. Kobayashi, K. F. Chang, M. Reduzzi, D. M. Neumark, and S. R. Leone, Opt. Lett. (2017).

[59]   F. Silva, M. Miranda, B. Alonso, J. Rauschenberger, V. Pervak, and H. Crespo, Opt. Express (2014).

[60]   K. Codling, R. P. Madden, and D. L. Ederer, Phys. Rev. (1967).

[61]   R. P. Madden, D. L. Ederer, and K. Codling, Phys. Rev. (1969).

[62]   X. Wang, M. Chini, Y. Cheng, Y. Wu, and Z. Chang, Appl. Opt. **52**, 323 (2013).

[63]   O. V. E. Mber, **10**, 2080 (1974).

[64]   K. Schulz, M. Domke, R. Püttner, A. Gutiérrez, G. Kaindl, G. Miecznik, and C. H. Greene, Phys. Rev. A **54**, 3095 (1996).

[65]   M. F. Jager, C. Ott, C. J. Kaplan, P. M. Kraus, D. M. Neumark, and S. R. Leone, Rev. Sci. Instrum. **89**, (2018).

[66] E. Hecht, *Optics 4th Edition* (1998).

[67] A. J. Den Boef, Surf. Topogr. Metrol. Prop. (2016).

[68] C. Wagner and N. Harned, Nat. Photonics (2010).

[69] G. Van Der Laan, J. Phys. Condens. Matter (1991).

[70] C. M. Jiang, L. R. Baker, J. M. Lucas, J. Vura-Weis, A. P. Alivisatos, and S. R. Leone, J. Phys. Chem. C (2014).

[71] A. Cirri, J. Husek, S. Biswas, and L. R. Baker, J. Phys. Chem. C (2017).

[72] J. Vura-Weis, C. M. Jiang, C. Liu, H. Gao, J. M. Lucas, F. M. F. F. De Groot, P. Yang, A. P. Alivisatos, and S. R. Leone, J. Phys. Chem. Lett. **4**, (2013).

[73] C.-M. Jiang, L. Robert Baker, J. Matthew Lucas, J. Vura-Weis, A. Paul Alivisatos, and S. R. Leone, J. Phys. Chem. C (2014).

[74] L. R. Baker, C. M. Jiang, S. T. Kelly, J. M. Lucas, J. Vura-Weis, M. K. Gilles, A. P. Alivisatos, and S. R. Leone, Nano Lett. (2014).

[75] L. Tang, S. E. Kocabas, S. Latif, A. K. Okyay, D. S. Ly-Gagnon, K. C. Saraswat, and D. A. B. Miller, Nat. Photonics (2008).

[76] N. E. Posthuma, G. Flamand, W. Geens, and J. Poortmans, Sol. Energy Mater. Sol. Cells (2005).

[77] M. Zürch, H.-T. Chang, P. M. Kraus, S. K. Cushing, L. J. Borja, A. Gandman, C. J. Kaplan, M. H. Oh, J. S. Prell, D. Prendergast, C. D. Pemmaraju, D. M. Neumark, and S. R. Leone, Struct. Dyn. (Melville, N.Y.) **4**, 044029 (2017).

[78] D. T. F. Marple and H. Ehrenreich, Phys. Rev. Lett. (1962).

[79] D. E. Aspnes and A. A. Studna, Phys. Rev. B (1983).

[80] D. Brust, J. C. Phillips, and F. Bassani, Phys. Rev. Lett. (1962).

[81] H. R. Philipp and E. A. Taft, Phys. Rev. (1960).

[82] O. P. Rustgi, J. S. Nodvik, and G. L. Weissler, Phys. Rev. **122**, 1131 (1961).

[83]   H. R. Philipp and H. Ehrenreich, Phys. Rev. **129**, 1550 (1963).

[84]   B. Feuerbacher, M. Skibowski, R. P. Godwin, and T. Sasaki, J. Opt. Soc. Am. **58**, 1434 (1968).

[85]   B. L. Henke, E. M. Gullikson, and J. C. Davis, At. Data Nucl. Data Tables (1993).

[86]   M. Taniguchi, S. Suga, S. Shin, K. Inoue, M. Seki, and H. Kanzaki, Solid State Commun. **44**, 85 (1982).

[87]   S. K. Sahari, H. Murakami, T. Fujioka, T. Bando, A. Ohta, K. Makihara, S. Higashi, and S. Miyazaki, Jpn. J. Appl. Phys. **50**, 04DA12 (2011).

[88]   J. H. Underwood, E. M. Gullikson, M. Koike, P. J. Batson, P. E. Denham, K. D. Franck, R. E. Tackaberry, and W. F. Steele, in *Rev. Sci. Instrum.* (1996).

[89]   J. Als-Nielsen and D. McMorrow, Phys. Today (2002).

[90]   C. A. D. Roeser, A. M. T. Kim, J. P. Callan, L. Huang, E. N. Glezer, Y. Siegal, and E. Mazur, Rev. Sci. Instrum. **74**, 3413 (2003).

[91]   T. Shih, M. T. Winkler, T. Voss, and E. Mazur, Appl. Phys. A Mater. Sci. Process. (2009).

[92]   G. D. Mahan, in *Many-Particle Phys.*, 3rd ed. (2000).

[93]   E. Shiles, T. Sasaki, M. Inokuti, and D. Y. Smith, Phys. Rev. B (1980).

[94]   D. Attwood, *Soft X-Rays and Extreme Ultraviolet Radiation: Principles and Applications* (1999).

[95]   J. Shah, *Ultrafast Spectroscopy of Semiconductors and Semiconductor Nanostructures* (Springer Science & Business Media, 2013).

[96]   D. König, K. Casalenuovo, Y. Takeda, G. Conibeer, J. F. Guillemoles, R. Patterson, L. M. Huang, and M. A. Green, Phys. E Low-Dimensional Syst. Nanostructures **42**, 2862 (2010).

[97]   M. Zürch, H.-T. Chang, P. M. Kraus, S. K. Cushing, L. J. Borja, A. Gandman, C. J. Kaplan, M. H. Oh, J. S. Prell, D. Prendergast, C. D. Pemmaraju, D. M. Neumark, and S. R. Leone, Struct. Dyn. **4**, (2017).

[98]   C.-M. Jiang, L. R. Baker, J. M. Lucas, J. Vura-Weis, A. P. Alivisatos, and S. R. Leone, J. Phys. Chem. C **118**, 22774 (2014).

[99] S. Mathias, C. La-O-Vorakiat, P. Grychtol, P. Granitzka, E. Turgut, J. M. Shaw, R. Adam, H. T. Nembach, M. E. Siemens, S. Eich, C. M. Schneider, T. J. Silva, M. Aeschlimann, M. M. Murnane, and H. C. Kapteyn, Proc. Natl. Acad. Sci. **109**, 4792 (2012).

[100] D. Zusin, P. M. Tengdin, M. Gopalakrishnan, C. Gentry, A. Blonsky, M. Gerrity, D. Legut, J. M. Shaw, H. T. Nembach, T. J. Silva, P. M. Oppeneer, H. C. Kapteyn, and M. M. Murnane, Phys. Rev. B **97**, 24433 (2018).

[101] E. Turgut, D. Zusin, D. Legut, K. Carva, R. Knut, J. M. Shaw, C. Chen, Z. Tao, H. T. Nembach, T. J. Silva, S. Mathias, M. Aeschlimann, P. M. Oppeneer, H. C. Kapteyn, M. M. Murnane, and P. Grychtol, Phys. Rev. B **94**, 220408 (2016).

[102] S. Mathias, C. La-o-vorakiat, J. M. Shaw, E. Turgut, P. Grychtol, R. Adam, D. Rudolf, H. T. Nembach, T. J. Silva, M. Aeschlimann, C. M. Schneider, H. C. Kapteyn, and M. M. Murnane, J. Electron Spectros. Relat. Phenomena **189**, 164 (2013).

[103] E. Turgut, C. La-o-vorakiat, J. M. Shaw, P. Grychtol, H. T. Nembach, D. Rudolf, R. Adam, M. Aeschlimann, C. M. Schneider, T. J. Silva, M. M. Murnane, H. C. Kapteyn, and S. Mathias, Phys. Rev. Lett. **110**, 197201 (2013).

[104] R. Berlasso, C. Dallera, F. Borgatti, C. Vozzi, G. Sansone, S. Stagira, M. Nisoli, G. Ghiringhelli, P. Villoresi, L. Poletto, M. Pascolini, S. Nannarone, S. De Silvestri, and L. Braicovich, Phys. Rev. B **73**, 115101 (2006).

[105] F. Krausz and M. Ivanov, Rev. Mod. Phys. **81**, 163 (2009).

[106] B. L. Henke, E. M. Gullikson, and J. C. Davis, Nucl. Data Table **54**, 181 (1993).

[107] F. Silva, M. Miranda, B. Alonso, J. Rauschenberger, V. Pervak, and H. Crespo, Opt. Express **22**, 10181 (2014).

[108] S. K. Cushing, M. Zürch, P. M. Kraus, L. M. Carneiro, A. Lee, H.-T. Chang, C. J. Kaplan, and S. R. Leone, ArXiv:1705.04393 [Cond-Mat, Physics:Physics] 1 (2017).

[109] T. Shin, S. W. Teitelbaum, J. Wolfson, M. Kandyla, and K. A. Nelson, J. Chem. Phys. **143**, 194705 (2015).

[110] S. Zollner, K. D. Myers, K. G. Jensen, J. M. Dolan, D. W. Bailey, and C. J. Stanton, Solid State

Commun. **104**, 51 (1997).

[111]   E. Gaubas and J. Vanhellemont, J. Electrochem. Soc. **154**, H231 (2007).

[112]   C. A. and E. of the L. V. III/17A-22A-41A1b, in *Gr. IV Elem. IV-IV III-V Compd. Part b - Electron. Transp. Opt. Other Prop.* (Springer-Verlag, Berlin/Heidelberg, n.d.), pp. 1–7.

[113]   C. Kittel, *Introduction to Solid State Physics* (Wiley, 2005).

[114]   L. J. Borja, M. Zürch, C. D. Pemmaraju, M. Schultze, K. Ramasesha, A. Gandman, J. S. Prell, D. Prendergast, D. M. Neumark, and S. R. Leone, J. Opt. Soc. Am. B **33**, C57 (2016).

[115]   D. W. Bailey and C. J. Stanton, J. Appl. Phys. **77**, 2107 (1995).

[116]   D. Attwood, *Soft X-Rays and Extreme Ultraviolet Radiation: Principles and Applications*, 1st ed. (Cambridge University Press, New York, NY, USA, 2007).

[117]   W. L. OBrien, J. Jia, Q. Y. Dong, T. A. Callcott, J. E. Rubensson, D. L. Mueller, and D. L. Ederer, Phys. Rev. B **44**, 1013 (1991).

[118]   B. T. Thole and G. van der Laan, Phys. Rev. B **38**, 3158 (1988).

[119]   A. Scherz, Spin-Dependent X-Ray Absorption Spectroscopy of 3d Transition Metals : Systematics and Applications, Free University of Berlin, 2003.

[120]   T. Shih, M. T. Winkler, T. Voss, and · E Mazur, Appl Phys A **96**, 363 (2009).

[121]   B. Feurbacher, M. Skibowski, R. P. Godwin, and T. Sasaki, **58**, 1434 (1969).

[122]   P. Y. Yu and M. Cardona, *Fundamentals of Semiconductors* (Springer-Verlag Berlin Heidelberg, 2010).

[123]   A. E. Siegman, *Lasers* (University Science Books, 1986).

[124]   G. Mak and H. M. van Driel, Phys. Rev. B **49**, 16817 (1994).

[125]   X. Q. Zhou, H. M. van Driel, and G. Mak, Phys. Rev. B **50**, 5226 (1994).

[126]   L. Viña, S. Logothetidis, and M. Cardona, Phys. Rev. B **30**, 1979 (1984).

[127]   A. Debernardi, S. Baroni, and E. Molinari, Phys. Rev. Lett. **75**, 1819 (1995).

[128] P. B. Allen and M. Cardona, Phys. Rev. B **23**, 1495 (1981).

[129] P. Lautenschlager, P. B. Allen, and M. Cardona, Phys. Rev. B **31**, 2163 (1985).

[130] P. B. Allen and M. Cardona, Phys. Rev. B **27**, 4760 (1983).

[131] A. Cavalleri, C. W. Siders, F. L. H. Brown, D. M. Leitner, C. Tóth, J. A. Squier, C. P. J. Barty, K. R. Wilson, K. Sokolowski-Tinten, M. Horn von Hoegen, D. von der Linde, and M. Kammler, Phys. Rev. Lett. **85**, 586 (2000).

[132] E. Gaubas and J. Vanhellemont, J. Electrochem. Soc. **154**, H231 (2007).

[133] B. R. Bennett, R. A. Soref, and J. A. Del Alamo, IEEE J. Quantum Electron. **26**, 113 (1990).

[134] P. A. Wolff, Phys. Rev. **126**, 405 (1962).

[135] M. L. Ledgerwood and H. M. van Driel, Phys. Rev. B **54**, 4926 (1996).

[136] P. Ruello and V. E. Gusev, Ultrasonics **56**, 21 (2015).

[137] C. N. Cohen-Tannoudji, Rev. Mod. Phys. **70**, 707 (1998).

[138] F. H. M. Faisal and J. Z. Kami\ifmmode \acuten\else ń\fiski, Phys. Rev. A **56**, 748 (1997).

[139] N. H. Lindner, G. Refael, and V. Galitski, Nat. Phys. **7**, 490 (2011).

[140] G. Usaj, P. M. Perez-Piskunow, L. E. F. Foa Torres, and C. A. Balseiro, Phys. Rev. B **90**, 115423 (2014).

[141] H. Hübener, M. A. Sentef, U. De Giovannini, A. F. Kemper, and A. Rubio, Nat. Commun. **8**, 13940 (2017).

[142] M. C. Rechtsman, J. M. Zeuner, Y. Plotnik, Y. Lumer, D. Podolsky, F. Dreisow, S. Nolte, M. Segev, and A. Szameit, Nature **496**, 196 (2013).

[143] F. Schmitt, P. S. Kirchmann, U. Bovensiepen, R. G. Moore, L. Rettig, M. Krenz, J. H. Chu, N. Ru, L. Perfetti, D. H. Lu, M. Wolf, I. R. Fisher, and Z. X. Shen, Science (2008).

[144] T. Rohwer, S. Hellmann, M. Wiesenmayer, C. Sohrt, A. Stange, B. Slomski, A. Carr, Y. Liu, L. M. Avila, M. Kalläne, S. Mathias, L. Kipp, K. Rossnagel, and M. Bauer, Nature **471**, 490 (2011).

[145] L. Stojchevska, I. Vaskivskyi, T. Mertelj, P. Kusar, D. Svetin, S. Brazovskii, and D. Mihailovic, Science (2014).

[146] R. Matsunaga, N. Tsuji, H. Fujita, A. Sugioka, K. Makise, Y. Uzawa, H. Terai, Z. Wang, H. Aoki, and R. Shimano, Science (2014).

[147] Y. H. Wang, H. Steinberg, P. Jarillo-Herrero, and N. Gedik, Science (2013).

[148] F. Mahmood, C. K. Chan, Z. Alpichshev, D. Gardner, Y. Lee, P. A. Lee, and N. Gedik, Nat. Phys. (2016).

[149] K. Ramasesha, S. R. Leone, and D. M. Neumark, Annu. Rev. Phys. Chem. (2016).

[150] A. L. Cavalieri, N. Müller, T. Uphues, V. S. Yakovlev, A. Baltuška, B. Horvath, B. Schmidt, L. Blümel, R. Holzwarth, S. Hendel, M. Drescher, U. Kleineberg, P. M. Echenique, R. Kienberger, F. Krausz, and U. Heinzmann, Nature (2007).

[151] S. Neppl, R. Ernstorfer, A. L. Cavalieri, C. Lemell, G. Wachter, E. Magerl, E. M. Bothschafter, M. Jobst, M. Hofstetter, U. Kleineberg, J. V. Barth, D. Menzel, J. Burgdörfer, P. Feulner, F. Krausz, and R. Kienberger, Nature (2015).

[152] Z. Tao, C. Chen, T. Szilvási, M. Keller, M. Mavrikakis, H. Kapteyn, and M. Murnane, Science (2016).

[153] L. Seiffert, Q. Liu, S. Zherebtsov, A. Trabattoni, P. Rupp, M. C. Castrovilli, M. Galli, F. Submann, K. Wintersperger, J. Stierle, G. Sansone, L. Poletto, F. Frassetto, I. Halfpap, V. Mondes, C. Graf, E. Ruhl, F. Krausz, M. Nisoli, T. Fennel, F. Calegari, and M. F. Kling, Nat. Phys. (2017).

[154] M. F. Ciappina, J. A. Pérez-Hernández, A. S. Landsman, W. A. Okell, S. Zherebtsov, B. Förg, J. Schötz, L. Seiffert, T. Fennel, T. Shaaran, T. Zimmermann, A. Chacón, R. Guichard, A. Zaïr, J. W. G. Tisch, J. P. Marangos, T. Witting, A. Braun, S. A. Maier, L. Roso, M. Krüger, P. Hommelhoff, M. F. Kling, F. Krausz, and M. Lewenstein, Reports Prog. Phys. (2017).

[155] M. B. Gaarde, C. Buth, J. L. Tate, and K. J. Schafer, Phys. Rev. A - At. Mol. Opt. Phys. (2011).

[156] M. Chini, X. Wang, Y. Cheng, Y. Wu, D. Zhao, D. A. Telnov, S. I. Chu, and Z. Chang, Sci. Rep. (2013).

[157] M. Reduzzi, J. Hummert, A. Dubrouil, F. Calegari, M. Nisoli, F. Frassetto, L. Poletto, S. Chen, M.

Wu, M. B. Gaarde, K. Schafer, and G. Sansone, Phys. Rev. A - At. Mol. Opt. Phys. (2015).

[158] Y. Kobayashi, H. Timmers, M. Sabbar, S. R. Leone, and D. M. Neumark, Phys. Rev. A (2017).

[159] Y. S. You, Y. Yin, Y. Wu, A. Chew, X. Ren, F. Zhuang, S. Gholam-Mirzaei, M. Chini, Z. Chang, and S. Ghimire, Nat. Commun. (2017).

[160] G. Vampa, T. J. Hammond, N. Thiré, B. E. Schmidt, F. Légaré, C. R. McDonald, T. Brabec, and P. B. Corkum, Nature (2015).

[161] M. Taniguchi, S. Suga, S. Shin, K. Inoue, M. Seki, and H. Kanzaki, Solid State Commun. (1982).

[162] S. A. Sato, L. Gallmann, Y. Shinohara, U. Keller, J. Herrmann, L. Kasmi, A. Ludwig, M. Volkov, K. Yabana, and M. Lucchini, Science (2016).

[163] A. Schiffrin, T. Paasch-Colberg, N. Karpowicz, V. Apalkov, D. Gerster, S. Mühlbrandt, M. Korbman, J. Reichert, M. Schultze, S. Holzner, J. V. Barth, R. Kienberger, R. Ernstorfer, V. S. Yakovlev, M. I. Stockman, and F. Krausz, Nature (2013).

[164] G. S. Engel, T. R. Calhoun, E. L. Read, T. K. Ahn, T. Mančal, Y. C. Cheng, R. E. Blankenship, and G. R. Fleming, Nature (2007).

[165] C. Ott, A. Kaldun, P. Raith, K. Meyer, M. Laux, J. Evers, C. H. Keitel, C. H. Greene, and T. Pfeifer, Science **340**, 716 (2013).

[166] R. C. Whited and W. C. Walker, Phys. Rev. Lett. (1969).

[167] R. S. Knox, in *Collect. Excit. Solids* (2012).

[168] M. G. Brereton, Phys. Bull. (2015).

[169] T. Kazimierczuk, D. Fröhlich, S. Scheel, H. Stolz, and M. Bayer, Nature (2014).

[170] K. Ueda, S. Inoue, H. Hosono, N. Sarukura, and M. Hirano, Appl. Phys. Lett. (2001).

[171] J. Tilchin, D. N. Dirin, G. I. Maikov, A. Sashchiuk, M. V. Kovalenko, and E. Lifshitz, ACS Nano (2016).

[172] C. J. Bardeen, Annu. Rev. Phys. Chem. (2013).

[173] S. Takeno, in *Theory Frenkel Excit. Using a Two-Level-Atom Model* (Springer, Boston, MA, n.d.),

pp. 69–73.

[174] V. Mauchamp, M. Jaouen, and P. Schattschneider, (n.d.).

[175] S.-D. Mo and W. Y. Ching, Phys. Rev. B (Condensed Matter) **62**, 7901 (2000).

[176] G. D. Mahan, Phys. Rev. B **15**, 4587 (1977).

[177] N. Jiang, D. Su, and J. C. H. Spence, Ultramicroscopy **109**, 122 (2008).

[178] W. F. Hanson, E. T. Arakawa, and M. W. Williams, J. Appl. Phys. Vac. Ultrav. J. Appl. Phys. J. Vac. Sci. Technol. B Microelectron. Process. Phenom. J. Appl. Phys. J. Phys. D Can. J. Phys **431**, 1661 (1972).

[179] W. L. O'brien, J. Jia, Q. Y. Dong, T. A. Callcott, J. E. Rubensson, D. L. Mueller, and D. L. Ederer, Phys. Rev. B **44**, 1013 (1991).

[180] W. L. O'Brien, J. Jia, Q.-Y. Dong, T. A. Callcott, K. E. Miyano, D. L. Ederer, D. R. Mueller, C.-C. Kao, and K. Sxe, Phys. Rev. B **47**, 140 (1993).

[181] A. Quattropani, F. Bassani, G. Margaritondo, and G. Tinivella, Nuovo Cim. B Ser. 11 **51**, 335 (1979).

[182] J. S. Toll, Phys. Rev. (1956).

[183] J. Venables, J. Mod. Opt. (2007).

[184] A. B. Kuzmenko, Rev. Sci. Instrum. (2005).

[185] V. Shtrauss, Signal Processing (2006).

[186] T. S. Robinson, Proc. Phys. Soc. Sect. B (1952).

[187] E. Palik D, in *Handb. Opt. Constants Solids* (1998).

[188] D. M. Roessler, D. M. Roessler, H. J. Lempka, S. G. Tomlin, E. Khawaja, G. K. M. Thutupalli, O. S. Heavens, M. M. Hargreave, D. W. Lane, D. Beaglehole, R. F. Miller, W. Hasan, and L. S. Julien, (n.d.).

[189] V. E. Henrich, G. Dresselhaus, and H. J. Zeiger, Phys. Rev. Lett. **36**, 158 (1976).

[190] A. Moulet, J. B. Bertrand, T. Klostermann, A. Guggenmos, N. Karpowicz, and E. Goulielmakis, Science **357**, (2017).

[191] M. Wu, S. Chen, M. B. Gaarde, and K. J. Schafer, Phys. Rev. A - At. Mol. Opt. Phys. (2013).

[192] A. R. B. and B. B. and E. R. W. and M. W. and S. C. and M. B. G. and K. J. S. and D. M. N. and S. R, New J. Phys. **16**, 113016 (2014).

[193] K. Sxe, **47**, 1 (1993).

[194] A. Blättermann, C. Ott, A. Kaldun, T. Ding, V. Stooß, M. Laux, M. Rebholz, and T. Pfeifer, Opt. Lett. (2015).

[195] E. R. Warrick, W. Cao, D. M. Neumark, and S. R. Leone, J. Phys. Chem. A (2016).

[196] W. Cao, E. R. Warrick, D. M. Neumark, and S. R. Leone, New J. Phys. **18**, 13041 (2016).

[197] A. P. Fidler, S. J. Camp, E. R. Warrick, E. Bloch, H. J. B. Marroux, D. M. Neumark, K. J. Schafer, M. B. Gaarde, and S. R. Leone, Nat. Commun. **10**, 1384 (2019).